JAEA-Review 2008-061

Annual Report of Fusion Research and Development Directorate of JAEA from April 1, 2007 to March 31, 2008

Fusion Research and Development Directorate

Japan Atomic Energy Agency
Naka-shi, Ibaraki-ken

(Received October 20, 2008)

This annual report provides an overview of major results and progress on research and development (R&D) activities at Fusion Research and Development Directorate of Japan Atomic Energy Agency (JAEA) from April 1, 2007 to March 31, 2008, including those performed in collaboration with other directorates of JAEA, research institutes, and universities.

The JT-60U operation regime was extended toward the long sustainment of high normalized beta (β_N) with good confinement ($\beta_N = 2.6 \times 28$ s). Effectiveness of real-time control of current profile was demonstrated in high β plasmas. Toroidal momentum diffusivity and the convection velocity were systematically clarified for the first time, and intrinsic rotation due to pressure gradient was discovered. Effects of toroidal rotation and magnetic field ripple on type I ELM size and pedestal performance were clarified, and type I ELM control was demonstrated by toroidal rotation control. Variety of inter-machine experiments, such as JT-60U & JET, and domestic collaborations were performed.

In theoretical and analytical researches, for the NEXT (Numerical Experiment of Tokamak) project, numerical simulations of a tokamak plasma turbulence progressed and a zonal field generation was investigated. Also, nonlinear MHD simulations found the Alfven resonance effects on the evolution of magnetic islands driven by externally applied perturbations. Integrations of several kinds of element codes progressed in the integrated transport/MHD model, the integrated edge/pedestal model and the integrated SOL/divertor model.

In fusion reactor technologies, R&Ds for ITER and fusion DEMO plants have been carried out. For ITER, a steady state operation of the 170GHz gyrotron up to 800 s with 1 MW was demonstrated. Also extracted beam current of the neutral beam injector has been extended to 320 mA at 796 keV. In the ITER Test Blanket Module (TBM), designs and R&Ds on Water and Helium Cooled Solid Breeder TBMs were progressed. For the ITER TBM fabrication technology, a full-scale TBM first wall was fabricated with reduced-activation-ferritic-martensitic steel (F82H) by a hot isostatic press method. Tritium processing technology for breeding blankets and neutronics integral experiments with a blanket mockup were also progressed. For ITER and DEMO blankets, studies on neutron irradiation effects and ion irradiation effects on F82H steel characteristics were continued using HFIR, TIARA and so on.

ITER Agreements entered into force on 24th October 2007. On the same day ITER Organization (IO) was established and JAEA was designated as the Japanese Domestic Agency (JADA) by Japanese Government. The Procurement Arrangement for the Toroidal Field (TF) Conductors was concluded between the IO and JADA in Nov. 2007, and then the contract with Japanese companies to fabricate TF conductors was launched in March 2008. The Quality Assurance Program of JADA inevitable to implement the procurement was approved by the IO. The Project Management (e.g. Schedule Management, Procurement Management, and QA) of JADA was executed. The preparation of the procurement was continued for the TF coil, Blanket First Wall, Divertor, Remote maintenance System of Blanket, EC and NB Heating System, and Diagnostics.

The Agreement for the Broader Approach (BA) Activities entered into force and JAEA was assigned as the Implementing Agency for the BA Activities, on 1st June 2007. Contracts for the constructions of the buildings for the IFERC Project and the IFMIF/EVEDA Project as well as the preparation for the Rokkasho site were made in March 2008. For the IFERC Project, information exchange to obtain common view of DEMO design

---

Editors: Kubo, H., Hoshino, K., Isei, N., Nakamura, H., Sato, S., Shimada, K., Sugie, T.

was carried out. Procurement Arrangement for the urgent tasks to be implemented for DEMO R&D was concluded. Preparation toward selection of a super computer for the Computational Simulation Centre started. For the IFMIF/EVEDA Project, detailed planning for the initial engineering research of the accelerator components, the lithium target and the test cell were implemented. On JT-60SA project, Executive Summary of the Conceptual Design Report including the baseline project schedule was approved at the 1st BA Steering Committee Meeting. The Integrated Project Team, consisting of the Project Team, JAEA Home Team and EU Home Team, was organized and developed the Integrated Design. The Procurement Arrangements were launched between the Implementing Agencies, JAEA and F4E, for the supply of PF magnet conductor and winding building, vacuum vessel and materials of in-vessel components.

Finally, as to fusion reactor design study, physics design on current drive and beta limit analysis and neutronics design on the blanket for SlimCS progressed.

Keywords; Fusion Plasma, Fusion Technology, JT-60, JT-60SA, ITER, Broader Approach, IFMIF/EVEDA, International Fusion Energy Research Center, DEMO Reactor

Contents

I. JT-60 Program

1. Experimental Results and Analyses

The JT-60U tokamak project has focused on the physics and engineering issues for the establishment of burning plasma operation in ITER and steady-state high β operation toward JT-60SA and DEMO. Since the optimization of current profile and pressure profile is essential for the stable and steady plasma operation, enhancing the control capability of these parameters is quite important. In addition, plasma rotation has a critical influence on magneto-hydro-dynamic (MHD) stability in the high β plasmas, edge pedestal performance and edge localized mode (ELM) characteristics. Thus, to expand the flexibility of heating and rotation profile control, the power supply system for 3 neutral beams (NBs) has been upgraded so as to enable the maximum injection period of 30 s in 2007. By making full use of the state-of-the-art tools of feedback control, heating/current drive and diagnostics, significant progress has been made in the integrated research on steady-state operation, transport, MHD stability, and edge pedestal physics.

1.1 Extended Plasma Regimes

Operation regime was extended toward the long sustainment of high β_N with good confinement [1.1-1]. Real-time control of current profile was applied to high β plasmas, and the effectiveness of controlling the minimum in the q profile (q_{min}) in high β plasmas was clearly demonstrated [1.1-2]. Driven current profiles for the off-axis tangential NBIs were directly evaluated using motional Stark effect (MSE) diagnostics, and compared with ACCOME calculation [1.1-2].

1.1.1 Long Sustainment of High β_N Plasma

Toward the development of the ITER hybrid operation scenario where the large current (low q_{95}) operation for a long period is required both with high β_N and a moderate current drive (CD) fraction, JT-60U has extended the operation regime, making full use of the increased heating power for a long pulse in this campaign; see Fig. I.1.1-1. Power supply systems for 3 units of NBs (about 6 MW) are modified to enable 30 s operation (formerly 10 s). The sustained period with β_N=2.6 has been almost tripled from 10 s to 28 s in the high-β_p ELMy H-mode plasma at low q_{95}=3.2 (I_p=0.9 MA, B_t=1.5 T). The duration corresponds to about 16 times of the current diffusion time (τ_R). Good confinement (H_{H98y2}≥1) is kept for 25 s, where the period is limited by the degradation of confinement (after t=29 s in Fig. I.1.1-1(a)) due to increase in density caused by enhanced recycling. In this discharge, off-axis bootstrap current maintains the flat safety factor profile at q_{min}~1, and the values of bootstrap current fraction (f_{BS}) and non-inductively driven current (f_{CD}) are 0.43 and 0.48, respectively. Weak and infrequent sawtooth activities were observed, but they did not affect the confinement. The onset of the neoclassical tearing modes (NTMs) was successfully prevented by the optimization of pressure gradient at low-q rational surfaces (3/2 and 2) through adjustment of the heating profiles.

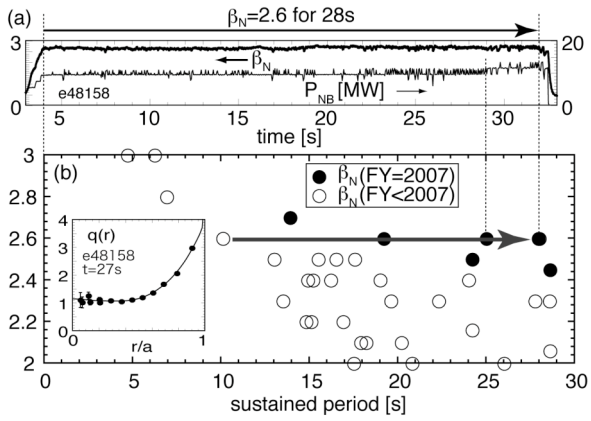

Fig. I.1.1-1 (a) Waveforms of a discharge in which β_N=2.6 was sustained for 28 s (and H_{H98y2}≥1 for 25 s). (b) Extended operation regime toward longer sustainment and higher $\beta_N H_{H98y2}$ (filled circles) from previous campaigns (open circles). The inset is the q profile at t=27 s. Sustained duration at β_N=2.6 has been almost tripled.

1.1.2 Real Time Current Profile Control

The minimum value of the safety factor profile (q_{min}) affects the MHD instability related to the low-q rational surface, such as m/n=3/2 and 2/1 NTMs, where m and n are the poloidal and toroidal mode numbers, respectively. In order to demonstrate the effectiveness of q_{min} control on elimination of MHD activities, the real-time control of q_{min} was applied to the high-β_p mode plasmas. Figure I.1.1-2 shows the waveforms of the discharge at I_p=0.8 MA, B_t=2.4 T (q_{95}=5.4). Neutral beams (NBs) of about 14 MW were injected to produce high β plasma. When the diamagnetic stored energy W_{dia} reached 1.55 MJ (β_N=1.7, β_p=1.5), the m/n=2/1

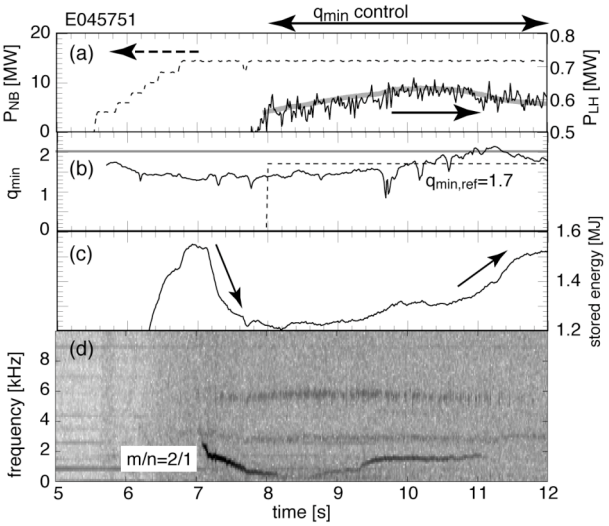

Fig. I.1.1-2 (a) NB injection power (dotted), LH injection power (thin solid), and its command value (thick solid). (b) q_{min} (solid) and its reference (dotted, $q_{min,ref}$=1.7). Gray line indicates q_{min}=2. (c) stored energy. (d) spectrogram of magnetic fluctuations. The control of q_{min} started from t=8 s.

NTM appeared, leading to decrease in W_{dia} by 22 %. In this discharge, we expected appearance of the m/n=3/2 NTM, so we set reference $q_{min,ref}$=1.7 intending to eliminate q=1.5 rational surface in the plasma. The lower hybrid (LH) waves were injected after t=7.5 s. The q_{min} control by LH power (P_{LH}) starts at t=8 s, with primary parallel-refractive-index $N_{//}$~1.65. When the q_{min} control started, P_{LH} increased to raise q_{min}. The q_{min} reached to 1.7 at t=10 s, and the LH power decreased by the control. The q_{min} overshot the reference $q_{min,ref}$, and reached to 2 at t~11 s. At this timing, the magnetic and density fluctuations at 1.6 kHz were suppressed, and W_{dia} started increasing back to the initial value. Due to the reduction of LH power from t~10 s, q_{min} decreased down to $q_{min,ref}$=1.7 at t~12 s, showing that LH current drive was actually effective in sustaining the q_{min} value.

1.1.3 Off-Axis NBCD

Off-axis current drive is essentially important in advanced operation in ITER and JT-60SA. Although off-axis current drive by neutral beams (NBCD) is a candidate for the off-axis current driver, the characteristics of the driven current profile had not been investigated yet due to the difficulty in measuring its broadly distributed current density profile. Using the MSE diagnostics, the NBCD profile was measured in plasmas with I_p=0.8 MA and 1.2 MA at B_t=3.8 T [1.1-2]. In both cases, no MHD activity was observed except ELMs, and the spatially localized NB driven current profile was measured for the first time. The total amount of the measured driven current agreed with calculations by the ACCOME code in both cases. In addition, the measured driven current profile was consistent with neutron-emission profile measurement representing beam ion profile. However, the measured driven current density profile was more off-axis than that in the calculations.

References

1.1-1 Ide, S., the JT-60 team, *Proc. 35th EPS Conf. on Plasma Physics,* ECA 32F (2008) I1.007.

1.1-2 Suzuki, T., *et al.*, *Nucl. Fusion* **48**, 045002 (2008).

1.2 Heat, Particle and Rotation Transport

1.2.1 Toroidal Momentum Transport and Rotation Profile in L-mode plasmas

Recent tokamak studies have been emphasizing that the plasma rotation profile plays essential roles in determining confinement and stability. In order to establish a method for controlling the rotation profile, construction of physics basis of momentum transport and its effect on rotation profiles is required. Concerning toroidal momentum transport, most of the previous works evaluated the diffusive term utilizing the steady state momentum balance equation. However, it is recognized that the measured toroidal rotation velocity (V_t) profiles cannot be explained by the momentum transport coefficient evaluated by the steady state equation.

Parameter dependences of the toroidal momentum diffusivity (χ_ϕ) and the convection velocity (V_{conv}), and the relation between χ_ϕ and heat diffusivity (χ_i) are systematically investigated in typical JT-60 L-mode plasmas using the transient analysis by using the momentum source modulation [1.2-1]. Experiments have been carried out to investigate the momentum transport. The absorbed power is varied from 2.4 to 10.7 MW under otherwise similar conditions (I_p=1.5 MA, B_t=3.8 T, q_{95}=4.2, δ=0.3, V_p=74 m^3). These plasmas stay in a low collisionality and small Larmor radius regime with ρ_{pol}*~0.03-0.06 and ν*~0.07-0.26. As shown in Fig. I.1.2-1, the momentum diffusivity increases with increasing the heating power, and the shape of χ_ϕ profile is nearly identical. The V_{conv} profile takes non-zero value and has a minimum value at r/a~0.6. The momentum diffusivity at r/a=0.6 roughly

scaled linearly with the heating power in this data set. We have also investigated I_p dependence of χ_ϕ and V_{conv}. During this I_p scan (I_p=0.87, 1.5, 1.77 MA), one CO tangential NB and one PERP-NB are injected with a similar absorbed power P_{abs}=3.3-4 MW and other plasma parameters were B_t=3.8-4.1 T, δ=0.3 and$\bar{n}_e$=1.3-1.9x10^{19} m^{-3}. The inverse χ_ϕ at r/a=0.6 increases linearly with I_p, and such improvement of the momentum confinement is confirmed by steady toroidal momentum profiles. It is also found that toroidal rotation velocity profiles in steady state can be almost reproduced by χ_ϕ and V_{conv} estimated from the transient momentum transport analysis at low β (β_N<0.4) as shown in Fig. 1.2-2.

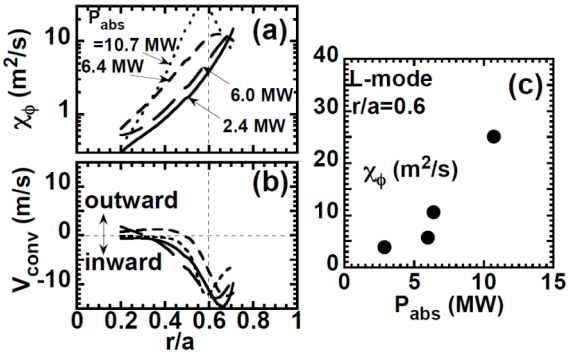

Fig. I.1.2-1 Profiles of (a) χ_ϕ and (b) V_{conv} during a heating power scan in L-mode plasmas. (c) Dependence of χ_ϕ at r/a=0.6 on absorbed power.

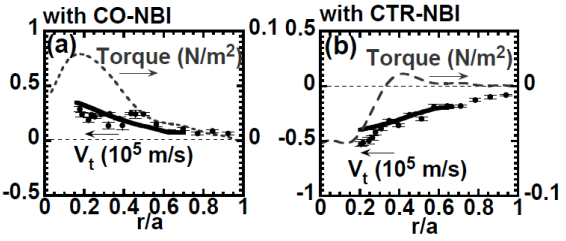

Fig. I.1.2-2 Experimental data (solid circles) and reproduced V_t profile (solid lines) in L-mode plasmas (a) with CO-NBI, and (b) with CTR-NBI, respectively. Torque profiles (dashed lines) are also shown.

1.2.2 Role of Pressure Gradient on Intrinsic Toroidal Rotation

The toroidal rotation velocity profile is determined by the momentum transport, external momentum source and intrinsic plasma rotation. It is important to separately evaluate contributions of the intrinsic rotation and the external induced rotation, and to understand the mechanism responsible for the generation of intrinsic rotation. Although the progress in understanding the physics of momentum transport and rotation has been made experimentally and theoretically in worldwide, the characteristics of the rotation profile including the spontaneous term is not yet sufficiently understood. This is due mainly to the experimental difficulty in separating the non-diffusive term and the spontaneous term.

We have identified the intrinsic rotation, which is not determined by the momentum transport coefficients and the external momentum input [1.2-2]. The momentum transport coefficients, such as χ_ϕ and V_{conv}, can be obtained separately from the transient momentum transport analysis, and the V_t profile is calculated using these coefficients, the external torque and the boundary condition of V_t [1.2-1]. From this approach, we have identified roles of externally induced rotation and the intrinsic rotation on the measured V_t profiles. The heating power scan is performed both in L-mode (I_p=1.5 MA, B_t=3.8 T, q_{95}=4.2, δ~0.3, κ~1.3-1.4) and in H-mode plasmas (I_p=1.2 MA, B_t=2.8 T, δ~0.33, κ~1.4) in order to investigate the effect of plasma pressure on the spontaneous rotation. The absorbed power is varied over the range 2.4 MW<P_{abs}<11 MW for the L-mode plasma discharges, and 4.8 MW<P_{abs}<10 MW for the H-mode discharges. Although the measured V_t profile agrees with the calculation in the region 0.45<r/a<0.65, the measured V_t deviates from the calculated one in the CTR-direction in the core region 0.2<r/a<0.45 as shown in Fig. I.1.2-3. The difference in V_t is observed in the region where such large pressure gradients are measured.

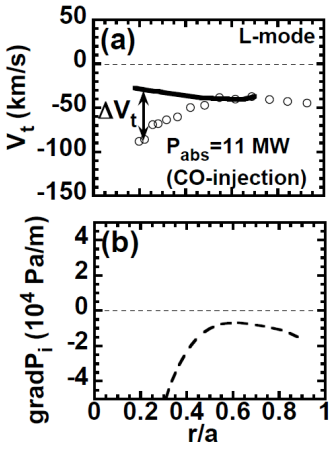

Fig. I.1.2-3 (a) Profiles of the measured V_t (open circles) and the calculated one (solid line), (b) and ∇P_i in the case of higher β_N=1.07 L-mode plasma with P_{abs}=11 MW.

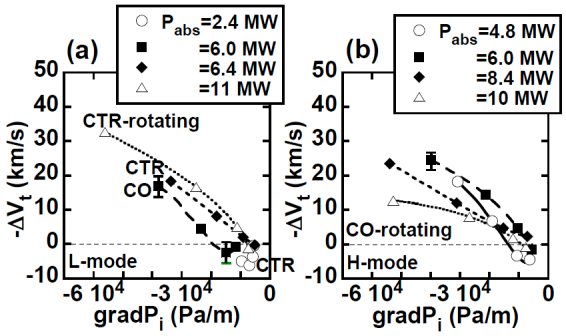

Fig. I.1.2-4 Difference between measured V_t and the calculated one (ΔV_t) is plotted against the ∇P_i during heating power scan in (a) L-mode and (b) H-mode plasmas.

A good correlation between the difference in V_t (i.e. $V_t(calculation) - V_t(measurement)$) and the pressure gradient is found during the heating power scan: ΔV_t increases with increasing pressure gradient in all cases including L-mode, H-mode, CO-, and CTR-rotating plasmas as shown in Fig. I.1.2-4. These results indicate that the local pressure gradient plays the role of the local value of spontaneous rotation velocity.

1.2.3. Dependence of Heat Transport on Toroidal Rotation in Conventional H-Modes in JT-60U

Temperature gradients are a key element in driving turbulent convection and causing anomalous heat transport in plasmas. The property of the turbulence driven by temperature gradient is believed to be provided by a strong increase of heat conduction which sustains a self-similar profile when the temperature profile exceeds a threshold in the temperature gradient (TG) scale length. The significant role of edge pedestal structure in H-modes, which is affected by the ELM activities, has been observed in many devices as a boundary condition for the heat transport in the plasma core. In JT-60U, the core temperatures vary in approximately proportion to the temperatures at the shoulder of the H-mode pedestal in a wide range of accessible densities in the type I ELMy H-mode regime, suggesting the existence of profile resilience. In H-mode plasmas where the ion channel is heated sufficiently by the positive ion-based neutral beams (NBs), the heat transport at the plasma core has been considered to be imposed strongly by the existence of a critical scale length of the ion temperature gradient L_{Ti}.

Understanding the effects of toroidal rotation velocity on the physical processes determining the heat transport and the pedestal structure in H-modes is one of the key issues in recent tokamak research. In JT-60U and DIII-D, it has been observed that the energy confinement is improved with the toroidal torque (and the resulting rotation) in co-direction to the plasma current I_p by the tangential NB. The confinement improvement with co-NBI accompanies the enhanced plasma pressure at the top of the H-mode pedestal together with the reduction of ELM frequency in case of JT-60U [1.2-3]. However, an underlying physics mechanism of this confinement improvement is not yet clear.

In this study, relation between heat transport in the plasma core and toroidal rotation as well as characteristics of the pedestal structure were examined in conventional ELMy H-mode plasmas in JT-60U. Conducting the experiments on power scan with a variety of toroidal momentum source generating the plasma rotation direction to co, balanced and counter with respect to the plasma current, dependence of the heat transport properties in the plasma core on toroidal rotation profiles was investigated. Energy confinement improvement was observed with increase in the toroidal rotation in co-direction. Heat transport in the plasma core varies, while self-similar temperature profile in the variations of toroidal rotation profiles are sustained. Pressure at the H-mode pedestal is increasing slightly with toroidal rotation in co-direction. Thus, energy confinement enhanced with co-toroidal rotation is determined by increased pedestal and reduced transport, brought on by profile resilience. In other words, heat transport in the plasma core is mainly determined by the saturation of temperature profile and is not strongly influenced locally by toroidal rotation. As shown in Fig. I.1.2-5, when the pedestal temperature was fixed between the cases of co and counter-NBI by adjusting the plasma density, the identical temperature profiles were obtained in spite of totally different toroidal rotation profiles. In H-mode plasmas where the ion channel is heated dominantly by the positive ion-based neutral beams, the saturation of ion temperature gradient governs the heat transport in the plasma core. As a result, large increase in heat conduction imposes the resilient profile of ion temperature, under which local effect of toroidal rotation profile on the scale length of ion temperature gradient is very weak [1.2-4].

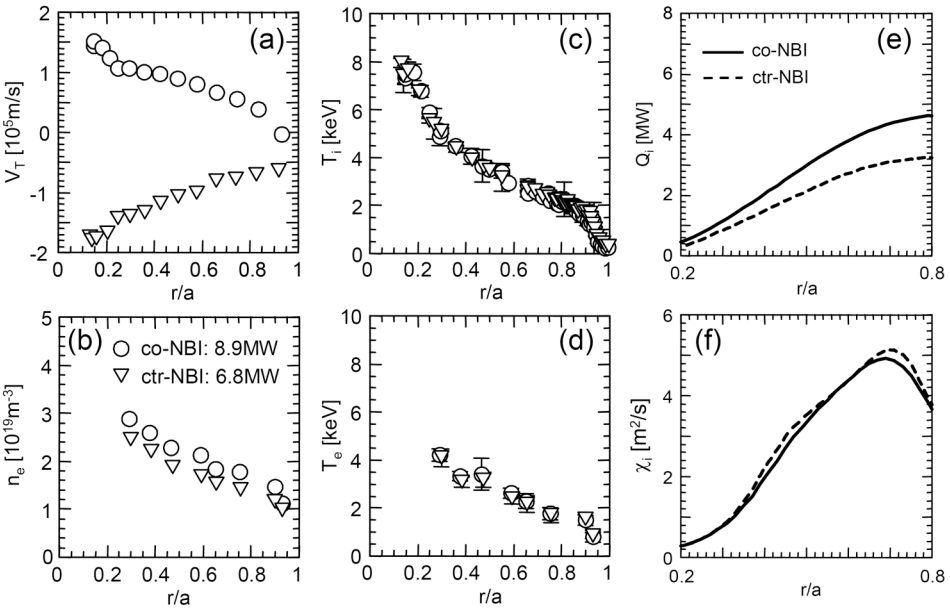

Fig. I.1.2-5 Profiles of (a) toroidal rotation, V_t, (b) electron density, n_e, (c) ion temperature, T_i, (d) electron temperature, T_e, (e) integrated ion conductive loss power, Q_i and (f) ion heat diffusivity, χ_i for the cases of co and counter-NBI. The pedestal temperature is decreased by increasing density for the case of co-NBI.

1.2.4 Comparisons of Density Profiles in JT-60U Tokamak and LHD Helical Plasmas with Low Collisionality

In order to understand particle transport systematically in toroidal plasmas, electron density profiles were compared in JT-60U tokamak and LHD helical plasmas with low collisionality. The neoclassical particle transport in a low collisionality regime is significantly different for tokamak and helical plasmas. In helical plasmas, the 1/ν regime exists, where the neoclassical transport is enhanced as being proportional to 1/ν (ν is collisionality) in non-axisymmetric helical plasmas due to the presence of helical ripples [1.2-5]. On the other hand, anomalous transport in both plasmas seems to be related with common physics in toroidal systems. Gyrokinetic analyses showed that the quasilinear particle flux driven by drift wave instabilities exhibits weak dependence on the magnetic configurations [1.2-6].

Figure I.1.2-6 shows dependence of density peaking factors on collisionality for JT-60U ELMy H-mode plasmas (I_p=1 MA and B_t=2 T) and LHD plasmas (B_t=2.8 T) with a magnetic axis (R_{ax}) of 3.5 m and 3.6 m [1.2-7]. Note that scaling studies indicated that both of these plasmas have the same weak gyro-Bohm like confinement feature [1.2-8]. Here, the density peaking factor was defined by a ratio of the central electron density at r/a=0.2 to the volume averaged density. In this figure, the abscissa indicates an electron-ion collision frequency normalized by a trapped electron bounce frequency (ν^*_b). The normalized collisionality of unity indicates a boundary between the collisionless region and the plateau region in both tokamak and single helicity (where only a single helical Fourier magnetic component exists) configurations. Thus, ν^*_b is a good index for showing the collisionality range for comparison. Here, the value of ν^*_b was calculated using plasma parameters at r/a=0.5. The density peaking factor increases with decreasing ν^*_b in JT-60U. The dependence in the collisionless region of LHD for R_{ax}=3.5 m tends to approach that in the collisionless region of JT-60U, although the dependence in the collisionless region of LHD for R_{ax}=3.6 m is reversed compared with that in the collisionless region of JT-60U.

The collisionality dependence of the density profile in JT-60U could be related to the anomalous inward pinch. The collisionality dependence of the density profile in LHD for R_{ax}=3.5 m could involve the anomalous inward pinch, because it has been shown that neoclassical transport in LHD in the plateau region becomes the less pronounced as the magnetic axis is moved the more inward [1.2-5]. Therefore, the

collisionality dependence of density profiles in LHD for R_{ax}=3.5 m might become similar to that in tokamak plasmas, because gyrokinetic analyses showed that the quasilinear particle flux driven by drift wave instabilities exhibits weak dependence on the magnetic configurations [1.2-6]. On the other hand, the collisionality dependence of density profiles in LHD for R_{ax}=3.6 m could be related to an increase in the neoclassical outward flux, because the convective flux for electrons is dominated by the temperature gradient driven flux, which increases in outward direction with decreasing collisionality in the 1/ν regime, in the datasets used here.

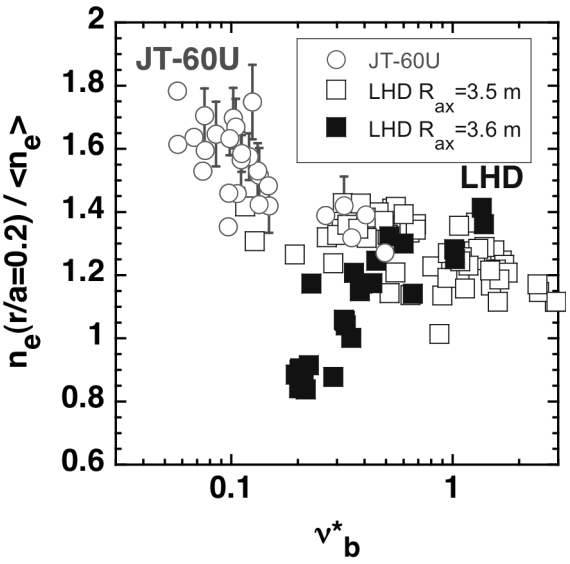

Fig. I.1.2-6 Dependence of the density peaking factor as a function of an electron-ion collisionality normalized by a trapped electron bounce frequency. Circles show data for JT-60U ELMy H-mode plasmas. Open and closed squares show data for LHD plasmas for R_{ax} = 3.5 m and 3.6 m, respectively.

References

1.2-1 Yoshida, M., *et al.*, *Nucl. Fusion* **47**, 856 (2007).

1.2-2 Yoshida, M., *et al., Physical Review Letters* **100**,105002(2008).

1.2-3 Urano, H., *et al., Nucl. Fusion* **47**, 706 (2007).

1.2-4 Urano, H., *et al., Nucl. Fusion* **48**, 085007 (2008).

1.2-5 Murakami S., *et al., Nucl. Fusion* **42**, L19 (2002).

1.2-6 Yamagishi O., *et al., Phys. Plasmas* **14**, 012505 (2007).

1.2-7 Takenaga H., *et al., Nucl. Fusion* **48**, 075004 (2008).

1.2-8 Yamada H. *et al., Nucl. Fusion* **45**, 1684 (2005).

1.3 MHD Instabilities and Control

1.3.1 MHD Stability Analysis of the High β Plasma for the Resistive Wall Mode Experiments

A very low rotation threshold was identified in JT-60U experiments in an investigation of the critical rotation for stabilizing resistive wall mode (RWM) by changing the toroidal plasma rotation using different combination of tangential neutral beams (NBs) [1.3-1]. Note that magnetic braking using external coils is not applied in JT-60U. The identified critical rotation is V_t ~20 km/s and corresponds to 0.3 % of the Alfvén velocity at the q=2 surface, which is much smaller than the previous prediction in DIII-D with magnetic braking. It is important for the RWM experiment to check the stability limit of external kink-ballooning mode without wall (no-wall limit) and with wall (ideal-wall limit) because RWM is destabilized between the ideal-wall limit and the no-wall limit. The MHD stability analysis code MARG-2D has been developed and has a useful interface for the analysis of experimental results with realistic plasma parameters, e.g. plasma pressure and current profile and equilibrium [1.3-2].

By using the MARG-2D code, the no-wall limit and ideal-wall limit in the RWM experiments was evaluated, and the value of the normalized beta (β_N) at the no-wall limit was β_N=2.3. Since the experimentally achieved β_N was about 2.8, it is sustained above the no-wall limit. Figure I.1.3-1 shows the plasma displacement of n=1 RWM for the plasma at the no-wall limit. Here, n is the toroidal mode number, and the displacement profiles with the poloidal mode number from 1 to 6 are shown in this figure. This mode has a global structure that contains internal and external components. Namely the peaks of m=2~4 components correspond to rational surfaces q=2~4. The components

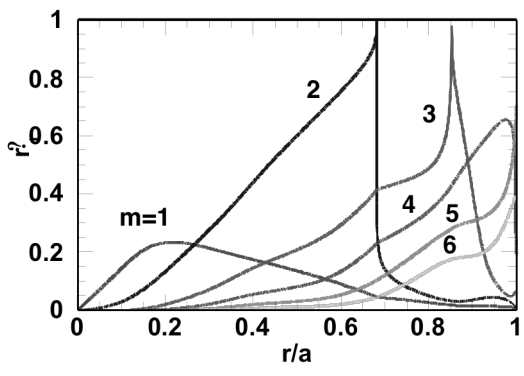

Fig. I.1.3-1 Plasma displacement of n=1 RWM for the plasma at β_N=2.3 without wall.

of m=1 and m>4 are non-resonant and externally resonant ones. Moreover, the amplitude of this mode at the low-field side is larger than that at the high-field side. This is consistent with the experimental measurements. By this numerical analysis, we can estimate the no-wall and ideal-wall limit using experimentally obtained profiles. By comparing with the numerical and experimental results, it is found that the experimentally obtained critical rotation is still low as β_N increases toward the ideal wall limit. These results indicate that for large plasmas such as in future fusion reactors with low rotation, the requirement of the additional feedback control system for stabilizing RWM is much reduced.

1.3.2 Simulation of Neoclassical Tearing Mode Stabilization

In JT-60U experiments, active stabilization of neoclassical tearing mode with m/n=3/2 or 2/1 using electron cyclotron current drive (ECCD) has been extensively performed. In addition, simulation of the stabilization of NTMs was performed using the TOPICS code combined with the modified Rutherford equation. In the simulation, the coefficients in the modified Rutherford equation were determined by comparing with experimental data. The TOPICS simulations were found to well reproduce the behavior of NTMs in JT-60U experiments. By using these coefficients, prediction analysis on NTM stabilization was performed.

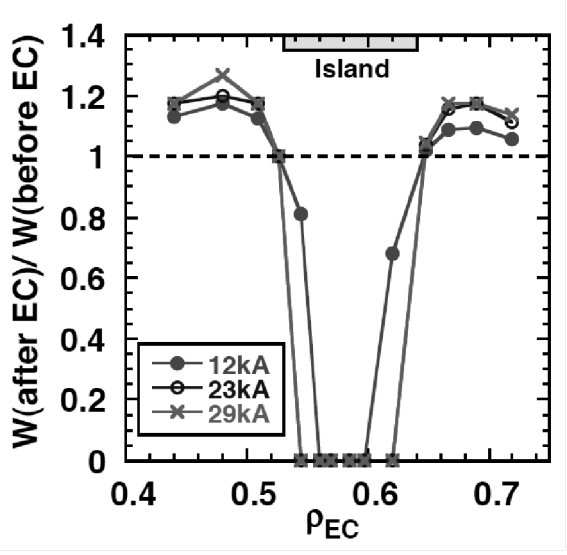

Fig. I.1.3-2 Magnetic island width after ECCD for various ECCD location and EC-driven current. The value of vertical axis is normalized by island width before ECCD.

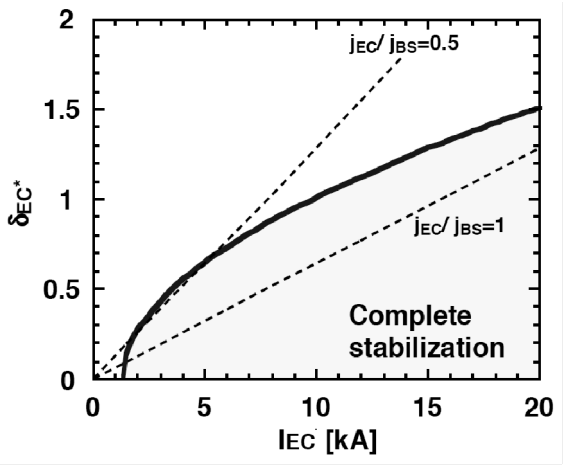

Fig. I.1.3-3 The region for complete stabilization in the space of EC driven current and ECCD deposition width. The solid curve is the boundary for the complete stabilization.

In particular, effects of ECCD location and ECCD deposition width on stabilization were investigated in detail [1.3-3,4]. Figure I.1.3-2 shows magnetic island width of m/n=2/1 NTM for various ECCD location (ρ_{EC}) and EC-driven current (I_{EC}). The value of the vertical axis is normalized by the island width before ECCD. For the reference case, I_{EC}=12 kA, the values of ECCD deposition width, full width of saturated island and mode location are 0.08, 0.11 and 0.59 in the normalized minor radius, respectively. The ratio of EC-driven current density to bootstrap current density at the mode rational surface, j_{EC}/j_{BS}, is about 1. This condition is similar to that in JT-60U experiments. In this case, NTM can be completely stabilized when misalignment is within about half of the full island width. When the misalignment is comparable to the island width, NTM is destabilized, and the width becomes wider by about 20 %. Such destabilization is actually observed in JT-60U experiments. When EC wave power is doubled (~23 kA), the V-shape profile becomes wider, that is, larger misalignment becomes acceptable for complete stabilization. However, at the same time, the destabilization effect also increases. When EC wave power is further increased to 29 kA, while allowed misalignment does not increase, the destabilization effect further increases. This suggests that precise adjustment is required to avoid NTM destabilization and subsequent mode locking even when abundant EC wave power is available. In addition to ECCD location, ECCD deposition width is another factor affecting NTM stabilization. In general, narrower

ECCD deposition width has stronger stabilization effect. Figure I.1.3-3 shows a region of complete stabilization in the space of I_{EC} and δ_{EC}*. Here, δ_{EC}* is full width at half maximum of ECCD deposition profile normalized by saturated island width. As shown in this figure, the boundary for complete stabilization increases roughly with $I_{EC}^{0.5}$. Thus, stabilization effect is roughly proportional to I_{EC}/δ_{EC}^2, showing that ECCD width is an important factor for NTM stabilization. The dependence is similar to the previously obtained result on m/n=3/2 NTM stabilization.

1.3.3 Instability in Ion Cyclotron Frequency Range [1.3-5]

The fluctuations in ion cyclotron range of frequency (ICRF) are driven by the presence of non-thermal ion distribution in magnetically confined plasmas. ICRF antennas are used as pickup loops for detecting electrostatic and/or electromagnetic fluctuations. Two sets of ICRF antennas, which are installed with the distance of 1.67 m in the toroidal direction, are used in this experiment and the toroidal wave number can be evaluated due to the small pitch angle of the toroidal magnetic field line. Two types of magnetic fluctuations are detected: one is due to high energy D-ions from neutral beam (NB) injections and the other is due to fusion products (FPs) of ^{3}He and T-ions. These fluctuations have been reported as ion cyclotron emissions (ICEs) in the burning plasma experiments on large tokamaks [1.3-6]. In this experiment, the first measurement of the toroidal wave numbers of those spontaneously excited waves is described. The modes due to D-ions have zero or small toroidal wave number k_z. On the other hand, the measurement of finite k_z in the modes due to FP-ions supports the excitation of the Alfvén waves is the possible origin of FP-ICEs. Figure I.1.-3-4 shows a typical intensity plot of the fluctuation amplitude as a function of time and frequency. The time sequence of NBs is indicated in the figure. Two sharp peaks, of which frequencies are corresponding to the fundamental and 2nd harmonic cyclotron frequencies of ^{3}He near the outer midplane edge of the plasma, appear when the tangential positive-ion-based NBs (P-NBs) are injected. After perpendicular P-NBs are injected, relatively broad peaks due to D-ions are detected. A peak with the lowest frequency below 10 MHz appears after negative-ion based NB is injected. This is considered to be due to T-ions. It is also observed that the excited modes due to FP-ions (^{3}He and T-ions) have different characteristics: driven by different neutral beams and having different parameter dependence. ICE due to T-ions has no harmonics and the value of ω/Ω_{ci} is smaller than that due to ^{3}He-ions. Both beam-driven ICEs and FP-ICEs are clearly observed, and those spatial structures are also obtained on JT-60U.

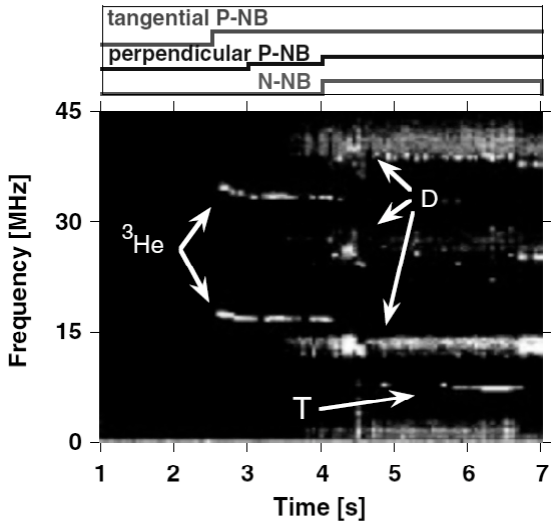

Fig. I.1.3-4 Typical intensity plot of the fluctuations in the case of tangential and perpendicular NBs. Two types of fluctuations (due to injected D-ions and fusion product ions of ^{3}He and T) are shown. The toroidal magnetic field strength is 2.3 T in this discharge.

1.3.4 Development of Active MHD Diagonostic System [1.3-7]

In order to actively diagonose the MHD stability such as RWM, edge localized mode (ELM) and Alfvén eigenmode (AE), we have been developing an active MHD diagnostic system in JT-60U. This system has two one-turn coils located 180º apart toroidally in the JT-60U vacuum vessel. These coils are connected to bipolar power supplies that can apply ±60 V and ±60 A as the maximum voltage and current, respectively. According to the calculation by Biot-Savart method in vacuum, the maximum magnitude of radial magnetic perturbations is predicted to be $\delta B_r \sim 0.1$ G at the plasma surface. Figure I.1.3-5 shows the Fourier components spectrum of magnetic perturbations produced by this system. In the case where the coil currents are out of phase and in phase with each other, the dominant mode number is odd and even, respectively. These toroidal mode spectra are fairly broadened up to the intermediate

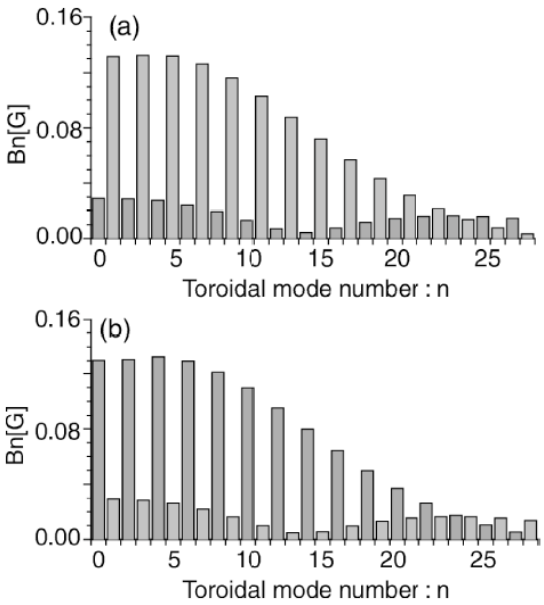

Fig. I.1.3-5 Fourier spectra of magnetic perturbations produced by the active MHD diagnostic system. (a) Odd and (b) Even connections.

n~20. This enables us to perform the active MHD diagnostic for low-n (RWM and low-n AE) to intermediate-n (ELM and AE) MHD instabilities. We expect that these could lead to deeper understanding of MHD stability.

References

1.3-1 Takechi, M., *et al.*, *Phys. Rev. Lett.* **98,** 055002 (2007).
1.3-2 Aiba, N., *et al.*, *Comput. Phys. Commun*. **175**, 269 (2006).
1.3-3 Isayama, A., *et al., Nucl. Fusion* **47**, 773 (2007).
1.3-4 Ozeki, T., *et al., Phys. Plasmas* **14**, 056114 (2007).
1.3-5 Ichimura, M., *et al.*, *Nucl. Fusion* **48**, 035012 (2008).
1.3-6 Dendy R.O., *et al., Nuclear Fusion* **35**, 1733-42 (1995).
1.3-7 Matsunaga, G., *et al., Proc. 10th IAEA Technical Meeting on Energetic Particles in Magnetic Confinement Systems 2007 (Kloster Seeon, 2007)* CD-ROM file P-10.

1.4 H-Mode and Pedestal Research

1.4.1 Effect of Toroidal Field Ripple and Toroidal Rotation on H-Mode Performance and ELM Characteristics in JET/JT-60U Similarity Experiments

In order to understand the effect of toroidal field (TF) ripple and toroidal rotation (V_t) on H-mode performance and ELM characteristics, dedicated ripple experiments were performed in JET and JT-60U using a matched plasma shape [1.4-1]. After the installation of ferritic steel tiles in JT-60U, toroidal field ripple, δ_r, near the outer midplane was reduced to ~0.5 % at B_t =2.2 T. In JET, on the other hand, δ_r can be varied by selecting the appropriate differential current between odd and even set of coils out of 32 TF coils, providing in this case four levels of ripple amplitude of δ_r=0.1, 0.5, 0.75 and 1 %. Although the same level of ripple amplitude was successfully obtained in both devices, the V_t in JET was still higher than that in JT-60U due to a different level of fast ion losses. Since a correlation between δ_r and V_T was found in JET plasmas, it is difficult to separate the two parameters, δ_r and V_t, in JET experiments.

A series of power and density scans indicated that plasmas with lower δ_r and/or larger co-V_t are favorable

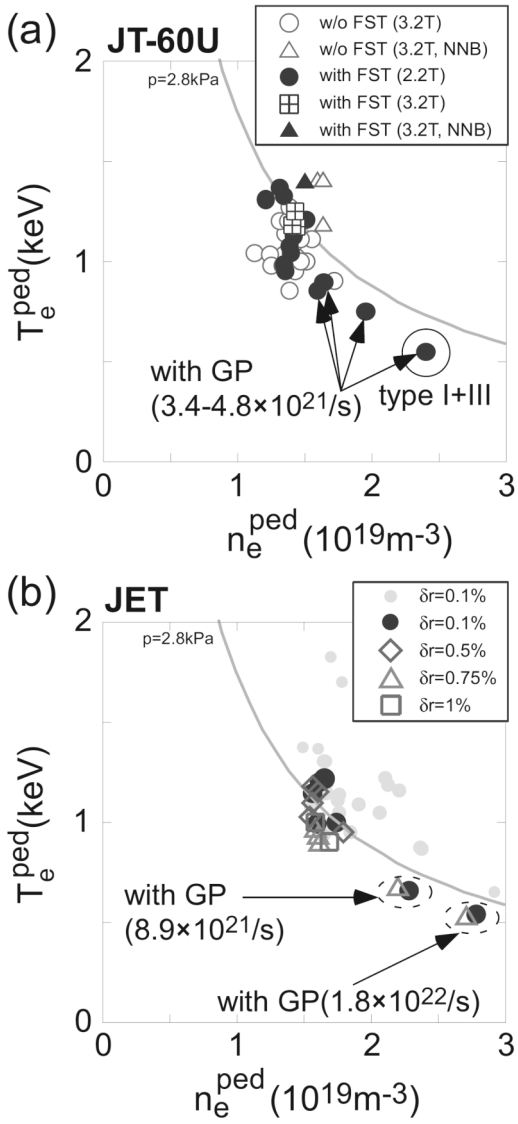

Fig. I.1.4-1 Comparison of electron density and temperature at the top of pedestal in ripple scan experiments in JT-60U (a) and in JET (b). ELM characteristics changed at n_e^{ped}~2.4×10^{19} m^{-3} from type I ELMs to type I+III ELMs in JT-60U.

to achieve higher p^{ped} and H_{H98y2} factor in both devices. As for ELM characteristics, larger co-V_t seems to increase the ELM energy loss together with the reduction of the ELM frequency. Sustaining a high n_e^{ped} with type I ELMs was still difficult in JT-60U plasmas even with FSTs ($\delta_r \sim 0.5$ %), while n_e^{ped} in JET plasmas at $\delta_r = 0.75$ % could be increased to similar value as at $\delta_r = 0.1$ % using the same amount of gas puffing, as shown in Fig. I.1.4-1. Therefore, there are still some differences between the two devices. In order to obtain a better prediction for ITER plasmas, further investigations into the effects of the TF ripple and the toroidal rotation are necessary, and the acceptable level of ripple amplitude in ITER is still uncertain from these experimental results in both devices.

1.4.2 Dimensionless Parameter Dependence of H-mode Pedestal Width Using Hydrogen and Deuterium Plasmas in JT-60U

In H-mode plasmas, the edge pedestal structure determines the boundary condition of the heat transport of the plasma core. Therefore, it is of primary importance to understand the physical processes determining the edge pedestal structure. The structure of the H-mode pedestal is composed of a height of the plasma pressure and a spatial width in which a steep pressure gradient is formed. In this region, the periodic expulsion of energy and particles is commonly observed due to the existence of the edge localized modes (ELMs) triggered by a steep pressure gradient and/or a large bootstrap current. However, the dependence of the spatial width of the H-mode edge transport barrier on local and global plasma parameters is not well understood. In particular, knowledge of the pedestal width Δ_{ped} based on dimensionless parameters is of great help for the extrapolation towards a next step device. However a well-validated means of predicting the spatial width of the H-mode transport barrier in ITER is still lacking and remains a major topic of research. Attempts to project a pedestal width for ITER through physics based or empirical scaling from multi-tokamak databases are underway to extend turbulent models through the pedestal region in recent tokamak research.

A variety of empirical scalings of Δ_{ped} during the well-developed type I ELMy H-mode phase have been proposed empirically, based on theoretical or semi-empirical models. However, these scalings vary from machine to machine and with the operational regime. In particular, a main argument on the pedestal width Δ_{ped} is whether Δ_{ped} scales as the normalized poloidal Larmor radius ρ_{pol}* or β_{pol}. This disagreement of the scalings intermingling ρ_{pol}* and β_{pol} can be caused by the existing edge stability boundary for ELMs. In this region, ρ_{pol}* and β_{pol} are linked strongly and thus are hard to separate out in the standard dimensionless parameter scan using a single gas species. To distinguish these variables, a pair of experiments in hydrogen and deuterium plasmas was conducted in this study. Explicit difference between ρ_{pol}* and β_{pol} is the mass dependence of ρ_{pol}* ($\propto m^{0.5}$) in contrast with no mass dependence in β_{pol}.

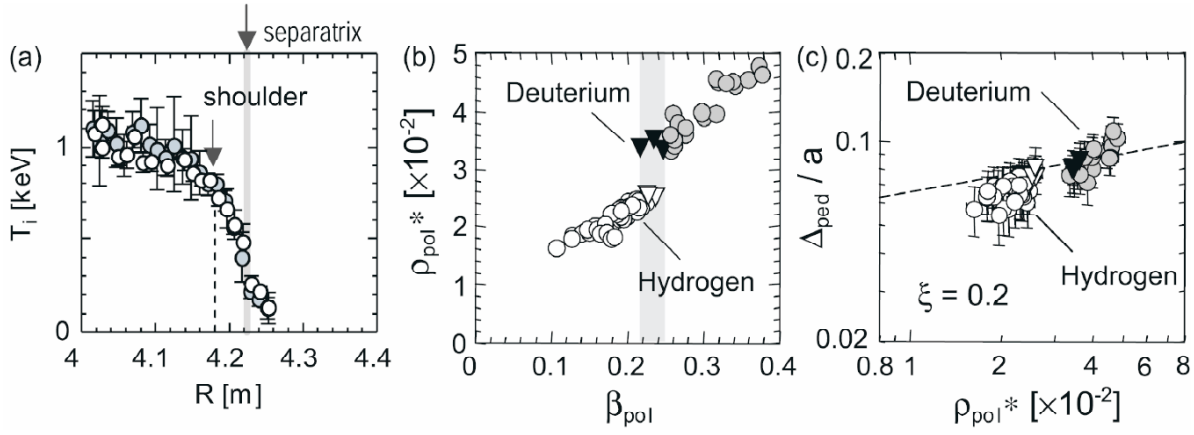

Fig. I.1.4-2 (a) Pedestal T_i profiles for the deuterium (shaded circles) and hydrogen plasmas (open circles) at the same β_{pol} and ν*. (b) Data area in $\beta_{pol} - \rho^*_{pol}$ space of the experiments. (c) Relation between ρ^*_{pol} and Δ_{ped}/a. The exponent of ρ^*_{pol} in the log-linear regression at fixed β_{pol} is $\xi = 0.2$. Closed and open inverse triangles indicate the deuterium and hydrogen plasmas at a given β_{pol} (~0.23), respectively.

Both the database analysis and the dedicated experiments on the mass scan indicated that the pedestal width depends very weakly on the plasma particle species or ρ_{pol}*. Identical profiles of the edge T_i obtained in the experiments suggested that the pedestal width more strongly depended on β_{pol} than ρ_{pol}* as shown in Fig. I.1.4-2. The experiment on β_{pol} scan was also performed. Higher β_{pol} plasma had higher pedestal T_i value accompanied by wider pedestal width in spite of almost identical ρ_{pol}* at the pedestal. Based on the experiments on the dimensionless parameter scan, the scaling of the pedestal width was evaluated as $\Delta_{ped} \propto a_p \rho_{pol}^{*0.2} \beta_{pol}^{0.5}$ [1.4-2].

References

1.4-1 Oyama, N., *et al.*, "Effect of toroidal field ripple and toroidal rotation on H-mode performance and ELM characteristics in JET/JT-60U similarity experiments," to be published to *Journal of Physics: Conference Series.*

1.4-2 Urano, H., *et al., Nucl. Fusion* **48**, 045008 (2008).

1.5 Divertor/SOL Plasmas and Plasma-Wall Interaction

1.5.1 Particle Control in Long-Pulse Discharges

The particle retention in the plasma surface wall has been investigated in a series of long-pulse discharges by a particle balance analysis [1.5-1]. As shown in Fig.I.1.5-1, the first 13 discharges with a line-averaged electron density lower than 3.5×10^{19} m^{-3}, which corresponds to ~75 % of the Greenwald density, the particle retention in the first wall gradually decreased. This is due predominantly to outgassing from the divertor plates with an increase of the surface temperature. In contrast, in the high-density discharges with a line-averaged electron density of 75 – 83 % of the Greenwald density, the particle retention changed to increase since the wall-pumping rate becomes positive. Several reasons are candidates for the positive wall-pumping rate and investigated. First, with increasing electron density, the increase of the divertor plate temperature was suppressed, resulting in lower outgassing rate compared to that of the low-density discharges. Second, in the high-density discharges, the co-deposition of deuterium with carbon became significant to enhance the fuel retention rate. Third, in addition, wall-pumping process was enhanced dynamically with increasing particle flux.

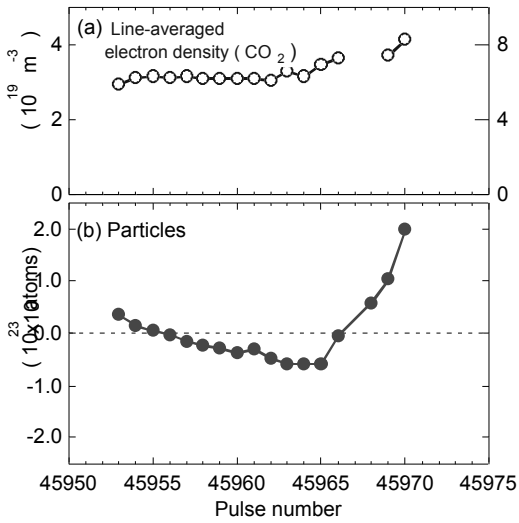

Fig.I.1.5-1 (a) line averaged electron density and (b) particle retention as a function of shot number.

1.5.2 Radiative Plasma Control

Reduction of heat loading appropriate for the plasma facing components is crucial for a fusion reactor. Power handling by large radiation power loss using impurity (Argon) gas seeding was studied to sustain the high confinement ELMy H-mode plasma with the large radiation power under the wall saturated condition, where particle recycling flux changes during the long discharge. Controllability of the large radiation in the good energy confinement plasma (H_{H98y2}=0.78-0.87) was investigated by the radiation feedback control of the Ar gas puff rate, using the bolometer signals viewing the main plasma edge. Total radiation fraction of P_{rad}/P_{abs} = 0.75-0.9 was maintained continuously during Ar gas puffing (up to 13 s so far) under the outgassing condition from the plasma facing components.

1.5.3 SOL Fluctuations and ELM

Characteristics of the ELM filaments and intermittent plasma events have been investigated from the fast sampling database of three reciprocating Mach probes measured in 2006. In particular, in-out asymmetry in the plasma propagation of these transient events was investigated [1.5-2, 3].

ELM plasma measurements showed two transient convective fluxes during the ELM event: one was the large, short convective flow caused by the filaments, and the other was the flow reversal over a wide SOL region. The latter fact was observed only at the

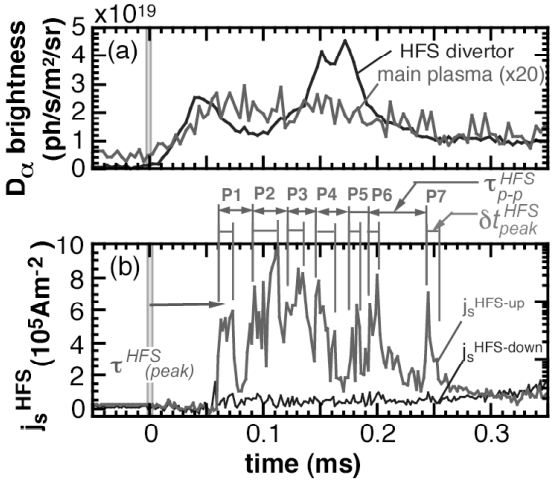

Fig.I.1.5-2 Enlarged time evolutions of ELM event: (a) D_α brightness in the main plasma and the HFS divertor, (b) j_s^{HFS} at upstream and downstream sides of the HFS Mach probe. Delay of the first j_s^{HFS} peak, separation and duration of these peaks are shown by $\tau^{HFS}(peak)$, $\tau_{p\text{-}p}{}^{HFS}$ and $\delta t_{pk}{}^{HFS}$.

High-Field-Side (HFS) SOL. During the early period of type I ELM event as shown in Fig. I.1.5-2, seven large peaks in the ion saturation current (j_s) appeared only at the upstream side of the HFS SOL ($j_s^{HFS\text{-}up}$), and the radial propagation was not seen. On the other hand, at the Low-Field-Side (LFS) midplane, multi-peaks in j_s were seen both at the upstream and downstream sides of the Mach probe, and radial propagation with $v_\perp$=0.4-3 km/s was evaluated. In Fig. I.1.5-2, delays of the first few peaks were smaller than the parallel convective transport from the LFS midplane (~190 μs). This fact suggested that ELM filaments extend to the HFS edge and are ejected into the SOL. In the characteristics of the filaments at the HFS SOL, the separation of the maxima ($\tau_{p\text{-}p}{}^{mid}$) was 25-55 μs, which was larger than those at the LFS midplane. The toroidal mode number was estimated to be relatively large (n=18–44) from the toroidal rotation velocity measurement. After the appearance of the multi-peaks, the flow reversal of the SOL plasma occurred over a wide SOL region.

Intermittent convective plasma transport, i.e. "plasma blobs" has been observed in the LFS SOL, which is thought to play a key role for cross-field transport of the SOL plasma. Conditional averaging method was employed to reveal the typical burst's profile, and Figure I.1.5-3 shows the typical time evolution of j_s at the LFS SOL and the positive spikes have the common property of a rapid increase and slow

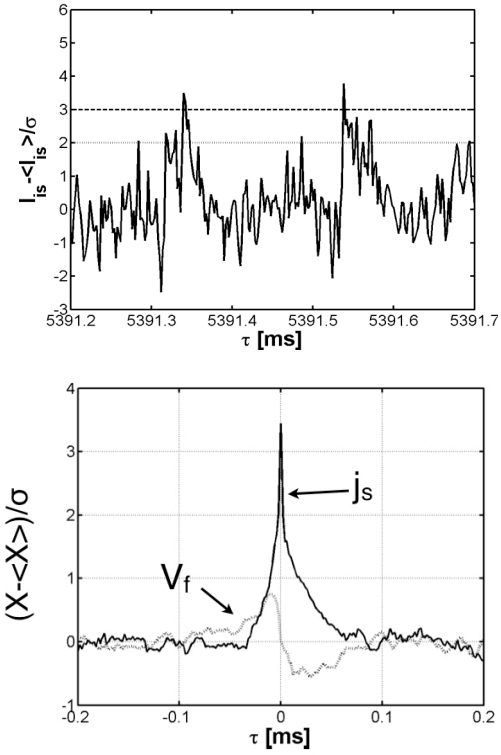

Fig.I.1.5-3 (a) Time evolution of j_s (b) conditional averaging results of j_s and floating potential V_f at LFS SOL.

decay. This feature was similar to that of theoretical prediction for plasma blobs. The conditional average of floating potential (V_f) measured simultaneously showed that V_f changes from positive to negative with respect to $\langle V_f \rangle$ as a large burst of j_s passes by. This result gives the internal potential structure of plasma blobs. The radial velocity of the plasma blob was estimated by using delayed time between the peaks of j_s and V_f to be about 0.43 km/s.

1.5.4 Spectroscopic Study in Divertor

The spectral lines of C^{2+} and C^{3+} emitted around the X-point in a detached plasma with MARFE were measured with a VUV spectrometer and a two-dimensional visible spectrometer in order to understand the controllability of the dominant radiation from C^{3+} [1.5-4]. As shown in Fig. I.1.5-4, it has been found that C^{3+} was produced by the volume recombination of C^{4+} and the ionization of C^{2+} comparably. In contrast, the volume recombination of C^{3+} was not detected, and the ionization flux of C^{3+} was less than 1 % of the C^{3+} generation flux. Thus, the C^{3+} generation flux was higher by two orders of magnitude

than the loss flux. This result suggests that loss mechanism of large number of C^{3+} ions from the radiation dominant region such as parallel or cross-field transport is significant. Because the ionization flux of C^{3+} was much smaller than the recombination flux of C^{4+} around the X-point, the predominant source of C^{4+}, which recombined into C^{3+}, was presumably the main plasma. Since the flux of C^{4+} is determined by the transport in the main plasma, it is difficult to control the C^{4+} flux.

Similarly, significant ionization of C^{2+} into C^{3+} and no recombination of C^{3+} into C^{2+} indicated that the source of C^{2+} exists in the divertor region, which can be increased for instance by seeding CD_4. Because the source rate of C^{3+} from the main plasma (the recombination of C^{4+}) and the divertor (the ionization of C^{2+}) was found to be similar as described above, the radiation loss control by impurity seeding from the divertor will work partly.

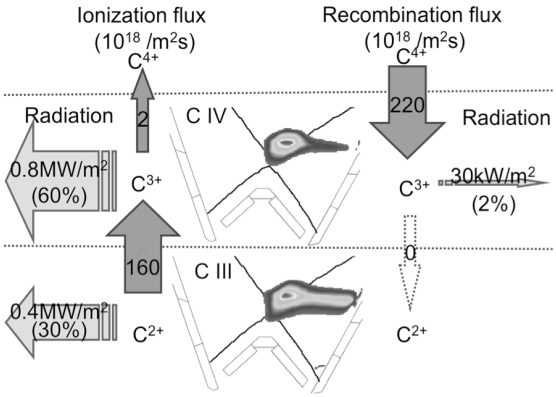

Fig.I.1.5-4 From the left, the radiation from ionizing component, the ionization flux, the spatial distribution of the emissivity, the recombination flux, and the radiation from recombining component of C^{3+} (upper) and C^{2+} (lower).

1.5.5 Study of Dust Dynamics

Movement and velocity of the dusts were measured with a fast visible TV camera (2-6 kHz) from tangential port to determine the trajectory and velocity of the dusts. In the main SOL, many dusts with various directions were observed, particularly, in the first shot after hard disruptions and overnight (3-7 hours) He-GDC. Many dusts were ejected from the inner divertor, in particular, for the high strike-point case: large ELM heat and particle loading on thick deposition layers may enhance producing dusts due to large thermal stress. Velocity of the toroidal movement (0.2-0.5 km/s) was faster than that of the radial movement (<0.05 km/s). Toroidal movement was mostly towards the ion drift direction (I_p), which is consistent with the SOL flow measurement at HFS and LFS SOLs.

1.5.6 Progresses of SOL and Divertor Code Development and Simulation Study

In order to understand the divertor pumping for particle control, the roles of atomic and molecular processes of ionization (Ie), charge exchange (CX), elastic collision (EL), and dissociation (DS) were investigated by the SOLDOR/NEUT2D code, which coupled the 2D plasma fluid modeling code SOLDOR and the Monte Carlo neutral kinetic modeling code NEUT2D. Characteristics of the incident neutrals into the exhaust slot were investigated from the dependence of the neutral pumping efficiency on the strike point distance from the slot. A case of small distance (2 cm) showed high pumping efficiency, where the most of neutrals produced on the target go toward the exhaust slot directly, except for the disappeared neutrals by Ie and DS processes. Whereas, for the long distance case of 10 cm, those neutrals were scattered at random by CX and EL and a few of them go toward the slot, leading a low pumping efficiency. Atomic and molecular processes was also identified when the divertor plasma changed from low n_e /high T_e ($n_{e\text{-}sp}^{ave}$=0.7×10^{19} m^{-3} and $T_{e\text{-}sp}^{ave}$=60 eV) to high n_e /low T_e ($n_{e\text{-}sp}^{ave}$=21×10^{19} m^{-3} and $T_{e\text{-}sp}^{ave}$≤1 eV). The incident neutrals to the slot for the low n_e /high T_e case were dominated by atoms produced through DS, then CX and EL. Molecules due to EL were are dominant for the high n_e /low T_e case [1.5-5].

A kinetic neutral model and a fluid neutral model in the divertor code have been compared under the detachment condition through collaboration with KEIO University. The SOL radial profiles of basic plasma and neutral parameters with the fluid neutral model were fitted to those with the kinetic model as the first step of the comparison, where the drift effects were also introduced. In the SOL, no significant effect of the drifts on the radial profiles of the plasma temperature and density was seen. However, in the divertor region, large differences were seen in the two models without the effects of drift, and drift effects tended to enlarge the difference. As a result, improvement of the fluid neutral

model is required in the divertor region. [1.5-6].

1.5.7 Tungsten Erosion and Deposition

Tungsten tiles have been installed at the upper row of the outer divertor in the No.8 port section since 2003. Poloidal and toroidal distributions of tungsten deposition on the divertor CFC/graphite tiles were investigated. A neutron activation method was used for the absolute measurement of W density by the $^{186}W(n,\gamma)^{187}W$ reaction by slow neutrons in JAEA/FNS (Fusion Neutronics Source). Conventional surface analysis methods such as EDX (Energy Dispersive X-ray spectrometry) and XPS (X-ray photoelectron spectroscopy) were also used.

For the divertor tiles exposed in 2003-2004, tungsten deposition on the dome tiles was found only near the top surface (within depth of a few μm), while tungsten on the inner divertor tiles was co-deposited with carbon to the depth up to about 60 μm. The neutron activation method could measure tungsten in these thick co-deposition layers. Ion beam analysis such as PIXE (Particle Induced X-ray Emission) was not appropriate for this case since only near-surface tungsten (~10 μm) was precisely measured by this method. It was found that tungsten deposition profile was not uniform toroidally. Tungsten surface densities near the inner strike point and on the outer wing were much higher at the toroidal position of 0 degree (near the W-tile position) than those toroidally separated at 60 degree (~3 m). Here the toroidal angle was defined as the angle viewed from the top of the torus (counter-clockwise).

Detailed measurement of the W toroidal distribution on the outer wing showed significant localization near the W-tile section. Since ionization length of W atom in the divertor plasma was more than an order of magnitude shorter than the distance of ~3 m, this long-distance deposition on the outer wing was not attributed to the local deposition of sputtered tungsten atoms. This result indicated that transport of tungsten ions in the outer divertor plasma was significantly affected by the cross-field transport in the private flux region. Toroidally localized W deposition was also observed on the inner divertor tile, thus significant amount of the tungsten could be also transported to the inner divertor through the private plasma by the cross-field transport such as drifts. At the same time, effect of the plasma flow along magnetic fields on the tungsten transport was also investigated.

1.5.8. Hydrogen-Isotope Retention

At the outer board first wall graphite tiles, it has been found that the deuterium retention was higher than the hydrogen retention even after hydrogen discharges for tritium degassing in 2004 [1.5-7]: at the surface of the tiles (< 0.1 μm), the hydrogen retention was higher than the deuterium retention. In contrast, the deuterium retention was higher in the deeper range between 0.1 μm and 1 μm (corresponding to the implantation depth of the fast ion), which contributed largely to the total amount of hydrogen-isotope retention, although it decreased with the depth. In a further depth range between 1 μm and 10 μm, the deuterium retention decreased gradually and finally reached a very low ratio of D to C ($D/C\sim10^{-4}$) [1.5-8].

The hydrogen-isotope retention in the side surfaces of the inner and the outer board first wall tiles was measured, and D/C was found to be comparable to that of the outer divertor tiles [1.5-9]. Compared to the tile surface of the inner divertor tiles, where the hydrogen-isotope retention was due predominantly to the co-deposition with carbon, D/C in the side surfaces of the first wall tiles was smaller. Since the total area of the tile side surface of the first wall tiles is much larger than that of the inner divertor tiles, the contribution of the tile side is under investigation. The deuterium depth profile was similar to that of boron, indicating that the deuterium was incorporated with boron.

The deuterium depth profile of the divertor tiles without the degassing discharges at the end of 2005-6 operations was measured for the first time [1.5-10]. Comparison of the deuterium depth profile at the inner divertor tile surface with and without the degassing discharges showed that about 90 % of the trapped deuterium was removed by the hydrogen degassing discharges. However, in the range deeper than ~1 μm, the deuterium retentions with and without degassing discharge were comparable within a factor of 2 (except for the dome top tile). Furthermore, it has been found that the deuterium concentration in the deep area (up to 16.4 μm) was not decreased. A similar depth profile was also found in the divertor tiles of ASDEX-U, and it was concluded that this is due to permeation of hydrogen isotopes along the orientation of carbon fibers [1.5-11].

This is also a candidate mechanism to explain the wall-pumping in the series of the high-density and long-pulse discharges [1.5-1].

References

1.5-1 Nakano, T., *et al.*, *Nucl. Fusion* **48**, 085002 (2008).

1.5-2 Asakura, N., *et al.,* "ELM propagation in the low- and high-field-side Scrape-off Layer of the JT-60U tokamak," to be published in *J. Phys.: Conf. Ser.* (2008).

1.5-3 Asakura, N., *et al.,* "Application of Statistical Analysis to the SOL Plasma Fluctuation in JT-60U," submitted to *J. Nucl. Mater.*

1.5-4 Nakano, T., *et al.,* "Radiation process of carbon ions in JT-60U detached divertor plasmas," submitted to *J. Nucl. Mater*.

1.5-5 Kawashima, H., *et al.*, *Contrib. Plasma Phys.* **48**, 158 (2008).

1.5-6 Hoshino, K., *et al.*, *Contrib. Plasma Phys.* **48**, 136 (2008).

1.5-7 Yoshida, M. *et al.*, "Hydrogen isotope retention in the first wall tiles of JT-60U," submitted to *J. Nucl. Mater.*.

1.5-8 Hayashi, T. *et al.*, *J Nucl. Mater.* **363-365**, 904 (2007).

1.5-9 Nobuta, Y. *et al*., "Retention and depth profile of hydrogen isotopes in gaps of the first wall in JT-60U," submitted to *J. Nucl. Mater*.

1.5-10 Hayashi, T. *et al.*, "Deuterium depth profiling in graphite tiles not exposed to hydrogen discharges before air ventilation of JT-60U," submitted to *J. Nucl. Mater.*

1.5-11 Roth, J. *et al.*, *J Nucl. Mater.* **363-365**, 822 (2007).

2. Operational and Machine Improvements

2.1 Tokamak Machine

2.1.1 Development of Supersonic Molecular Beam Injection

In order to control plasma pressure at the pedestal region and to evaluate the effect of fuel on the self-organization structure of plasma, a supersonic molecular beam injection (SMBI) system has been installed in JT-60U device. The SMBI system has been collaborated with CEA/Cadarache in France. The schematic diagram of the SMBI is shown in Fig. I.2.1-1. The nozzle heads were put on the wall of vacuum vessel (VV).

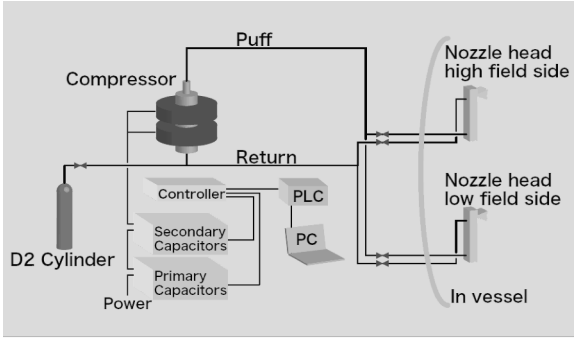

Fig. I.2.1-1 Schematic diagram of the SMBI system.

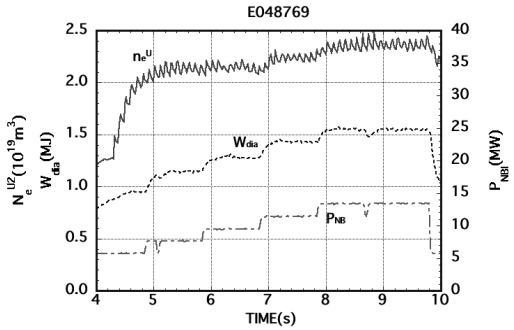

Fig. I.2.1-2 Time evolution of plasma parameters during the gas-jet injection using SMBI.

However, in the first SMBI system, the seal of the nozzle head was evaporated during baking of the vacuum vessel at a temperature of 300 degree C, causing a large seal leak. To improve this, heat-resistant materials were tested at JAEA and CEA/Cadarache, and FLUORITZ-HR was confirmed as a most promising seal material that showed no evaporation at temperature lower than 280 degree C. Thus, FLUORITZ-HR was adopted as a new seal material, and the baking temperature was decreased from 300 degree C to 280

degree C and gas pressure of the nozzle was increased from 0 MPa to 0.5 MPa to reduce the possibility of leak due to deformation of the seal. After these countermeasures, the SMBI successfully worked without vacuum leak.

Time evolutions of the plasma parameters in the case of high field side injection of SMBI are shown in Fig. I.2.1-2. The frequency of the SMBI is 10 Hz, and the pressure of SMBI is 0.3 MPa. The fast response of the plasma density synchronizing with the movement of the nozzle head of SMBI is confirmed.

2.1.2 Break-away of the Carbon Tiles

A carbon tile in the outer dome of the divertor was broken away and the tile dropped into the vertical port in June, 2006. The cause of the break was considered to be due to the heat flow from a plasma to the carbon tiles. The trace of heat concentration was observed at the bolt and nut between the tile and the basement of tile. The nut was melted by the heat flow and the tile was broken away from the basement.

Countermeasures for this break-away were taken during the maintenance period from May to September in 2007. In the inspection just after the break-away, bolt holes with unprocessed edges, which made a slight gap between the tile and the basement to reduce heat conduction between them, were found commonly for some of the dome tiles. Therefore, all bolt holes of the dome basements were processed. In addition, carbon sheets were set between the dome tiles and basements to ensure heat conduction though the dome had originally been designed as components that were not expected to directly receive high heat flux. However, the break-away of the carbon tile in the outer dome was found in March, 2008 again. The position of the tile is the same as that of the broken-away tile in June, 2006. The circumstance of the broken-away tile is shown in Fig. I.2.1-3. All tiles in outer dome (125 tiles) were checked again. No loosened bolt and melting were found except the broken-away tile. It is considered that the countermeasures for the first break-away was effective except the broken-away tile, although the cause has not been understood perfectly. The same countermeasures were taken again for the broken-away, and the position of the outer separatrix leg has been controlled at more than 0.5 cm away from the dome since this event.

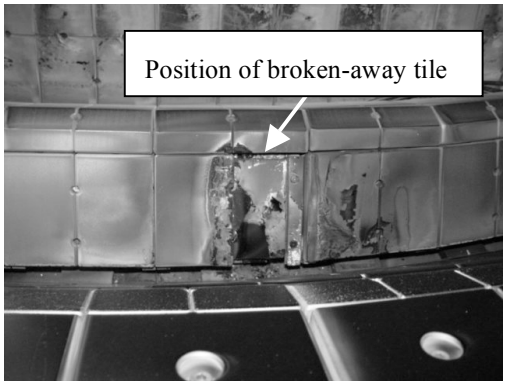

Fig. I.2.1-3 Photograph of circumstance of the broken-away tile.

2.2 Control System

2.2.1 New Real-Time Control Functions for Advanced Plasma Operation

For efficient exploration toward high performance plasmas in JT-60 operation, more advanced real-time control functions are required to be applied to the experiment. The major developments conducted in 2007 are presented as follows: (a) New real-time control of ion temperature (T_i) profile and toroidal rotation velocity (V_t) measured by the fast charge exchange recombination spectroscopy (CXRS) system during neutral beam heating [2.2-1]. (b) The integral control method newly employed for the real-time control of radiation power profile in a divertor plasma. (c) A digital filter newly applied to the separatrix strike position on the divertor dome plates for stable strike point control. (d) Multiple integral controls applied to a single real-time profile control. (e) Prompt plasma shape evolution viewer newly developed for efficient evaluation before the creation of JT-60 database using the real-time plasma shape visualization system [2.2-2, 3]. (f) Voltage control newly developed for safe operation even in case of deteriorated electrical insulation of the PF coil power supply. These new advanced plasma real-time control functions have contributed to achievement of annual mission parameters specified in JT-60 experimental plan.

2.2.2 Development of an FPGA-based Timing Signal Generator

The timing system in the supervisory control system of JT-60 [2.2-4] is composed of specially ordered CAMAC modules for limited usage [2.2-5]. This system generates trigger signals and a clock signal necessary for measurements and controls in the JT-60 experiment.

Recently, we have been facing difficulties in cost-effective maintenance due to CAMAC standardized hardware, and in increasing troubles due to the aged deterioration.

The following design guidelines for a new system configuration were employed: (a) A master clock cycle should be changed from 1 kHz to 40 MHz to improve accuracy. (b) FPGA (Field Programmable Gate Array) was chosen to minimize delay time for the logical calculation, and enhance the flexibility for changing logic flows. (c) The addition and change of the timing signal should be easily conducted in the new system. (d) The timing signal should be transmitted to the subsystem in less than 1 μs by using the optical cable. (e) The number of cables should be minimized, which requires multiplex transmission. (f) The interfaces between the supervisory timing system and subsystem one should remain unchanged.

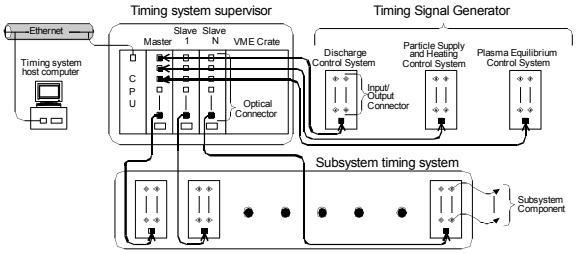

Fig. I.2.2-1 New timing system hardware configuration.

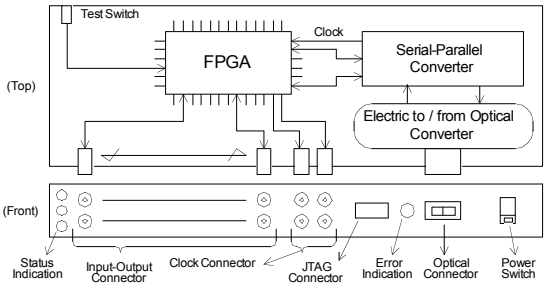

Fig. I.2.2-2 Circuit configuration of the timing signal generator.

Figure I.2.2-1 shows a new timing system hardware configuration. The timing system supervisor is composed of the VME-bus system with the host computer through Ethernet network. Figure I.2.2-2 shows the circuit configuration of the timing signal generator. Response time measurement of timing signal transmission has been carried out by using two timing signal generators connected with optical fiber cable as shown in Fig. I.2.2-3. Test result is shown in Fig. I.2.2-4 [2.2-6]. The elapsed transmission time was 276.5-326.5 ns, and reading time from input register was 50-100 ns, and writing time to output register was 62.5 ns. The optical transmission time takes 333 ns between supervisory timing system and subsystem. Total sum of test result and optical transmission time take 600-650 ns in signal transmission while 30-40 μs is needed in the original CAMAC system. This value is less than allowable delay time 1 μs.

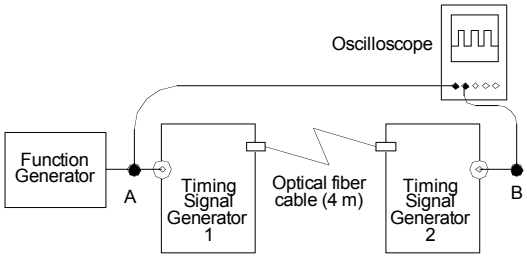

Fig. I.2.2-3 Configuration of timing signal transmission test.

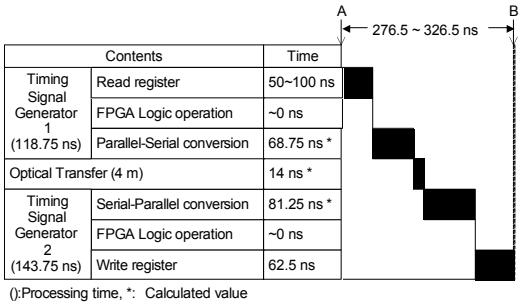

Contents		Time
Timing Signal Generator 1 (118.75 ns)	Read register	50~100 ns
	FPGA Logic operation	~0 ns
	Parallel-Serial conversion	68.75 ns *
Optical Transfer (4 m)		14 ns *
Timing Signal Generator 2 (143.75 ns)	Serial-Parallel conversion	81.25 ns *
	FPGA Logic operation	~0 ns
	Write register	62.5 ns

():Processing time, *: Calculated value

Fig. I.2.2-4 Elapsed time chart in the timing signal transmission test of test results

References

2.2-1 Yoshida, M., *et al.,* "Real-time measurement and feedback control of ion temperature profile and toroidal rotation in JT-60U," submitted to *Fusion Eng. Des.*

2.2-2 Sueoka, M., *et al., Fusion Eng. Des.* **83**, 283 (2008).

2.2-3 Sueoka, M., *et al., Fusion Eng. Des.* **82**, 1008 (2007).

2.2-4 Kurihara, K., *et al., Fusion Eng. Des.* **81**, 1729 (2006).

2.2-5 Akasaka, H., *et al., Fusion Eng. Des.* **71**, 29 (2004).

2.2-6 Kawamata, Y., *et al., Fusion Eng. Des.* **83**, 198 (2008).

2.3 Power Supply System

2.3.1 Operational Experience

Annual inspections and regular maintenances for the power supply system have been conducted to maintain high performance operation as shown in Table I.2.3-1.

In addition, the renewal and special maintenances have been also conducted to avoid troubles for the aged-deteriorated system as shown in Table I.2.3-2. These activities contributed to achieving safe operation of the systems.

Table I.2.3-1 Annual inspections and regular maintenances of the power supply system.

Item	Term
The Toroidal Field Coil Power Supply (TFPS)	April - October 2007
The Poloidal Field Coil Power Supply (PFPS)	April - October 2007
The Power Supply for Additional Heating Devices (H-MG)	September 2007
The Grounding Systems	January - February 2008
The Lightning Arrester System	January 2008
The Power Distribution Systems	July 2007

Table I.2.3-2 Renewals and special maintenances as measures for the aged-deteriorated power supply system.

Item	Term
Inspection of metal enclosed switchgears (M/C) for the Power Distribution System (every year)	July 2007
Renewal of MG shaft vibrograph for the H-MG	January 2008
Maintenance of outside metal enclosed switchgears for the TFPS	August - September 2008
Mass-spectroscopy of resolved gas in insulation oil for step-down transformers	February 2008

2.3.2 Investigation of MG Shaft Vibration in the Motor-Generator for Additional Heating Devices

The motor-generator with 300-ton flywheel for additional heating devices (H-MG) has double layers of stator windings connected together to a single output through the AC circuit breakers.

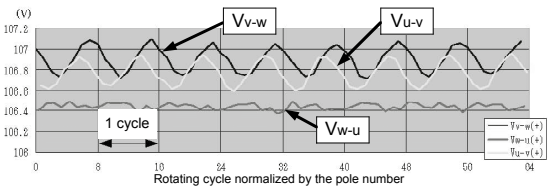

(a) Single Layer A

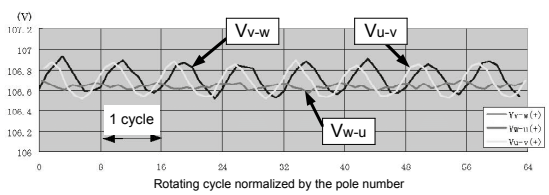

(b) Single Layer B

Fig. I.2.3-1 Output voltage ripple in the stator winding (Rotational speed: 580 min^{-1}, Exciter current: DC93 A).

A problem of the excessive shaft vibration was observed in the test operation with two-single-layer connection. Voltages between three phases for two single layers of stator windings are shown in Fig. I.2.3-1 (a) and (b). The voltages from the phase V commonly oscillated, while the voltage of U-W phases showed no oscillation.

When two single layers were connected together, no excessive shaft vibration occurred at all as shown in Fig. I.2.3-2. It could be understood that the V-phase stator winding might be somehow differently reconstructed from the original one in 2004.

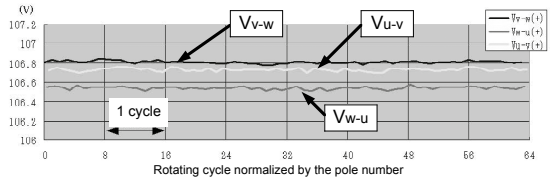

Fig. I.2.3-2 Output voltage ripple in case the two stator windings are connected together in parallel (Rotational speed: 580 min^{-1}, Exciter current: DC93 A).

2.4 Neutral Beam Injection System

In the campaign of 2007, the injection time of the negative-ion-based NBI (N-NBI) unit was successfully extended from previous 20 s to 27 s at 1.0 MW by modifying the negative ion sources. Four perpendicular positive-ion-based NBI units were also upgraded to extend the injection pulse length up to 30 s at 2 MW of injection power. These long pulse injections from the N-NBI and P-NBI units significantly contributed to the study on quasi-steady state plasmas in JT-60U.

2.4.1 Long Pulse Operation of NBI System

On JT-60U, there are 11 positive-ion-based NBI (P-NBI) units, each of which injects 2 MW D^0 beams. Out of P-NBI units, 4 tangential P-NBI units have been already upgraded to inject the D^0 beams for 30 s in 2006. In 2007, 4 perpendicular P-NBI units were additionally upgraded to extend the injection pulse length up to 30 s by mainly increasing the capacity of the power supplies. The injection pulse length of the upgraded P-NBI units is extended while the beam-limiter temperature increased by heat load of the high-energy re-ionized particles from the D^0 beams was confirmed to be reduced to an allowable level. The pulse lengths of the upgraded P-NBI units are extended from the previous

10 s to ~ 20 s. By using the tangential units modified in 2006 and the perpendicular units, high-power and long-pulse D^0 beams were reliably injected to meet the requirements of plasma physics. This significantly contributed to the study on quasi-steady state plasmas in JT-60U.

The injection pulse length in the N-NBI on JT-60U was also extended from the previous ~20 s to 27 s by optimizing the beam steering angle to reduce the grid power loading, as explained in 2.4.2. The time response of the neutron flux from the plasma indicates constant D^0 power without degradation during ~30 s. Since the voltage holding capability of the ion sources was as poor as 290 keV due to insufficient conditioning time, the D^0 beam was injected from one ion source, and hence the D^0 power was no more than 1 MW. Using two negative ion sources, the long-pulse beam at the higher power is to be injected [2.4-1].

2.4.2 R&D Programs of the Negative-Ion-based NBI System for the Performance Improvement

There remain three major issues to improve the performance of the negative-ion-based NBI system. One is to reduce the grid power loading below an acceptable level. Second is to understand the electron heat load in the beamline. Third is to improve the voltage holding capability of the ion source, where the usable acceleration voltage has been limited to < 400 kV.

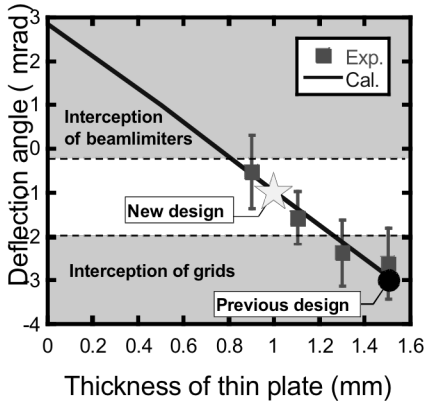

Fig. I.2.4-1 Beam steering by attaching a thin plate on extraction grid.

The JT-60U negative ion source was originally designed to produce high current beams of 22 A at 500 keV for 10 s through 1080 apertures that are distributed on five segmented grids. The beamlets must be steered to focus the overall beam envelope. It was found that some of the beamlets were mis-deflected and struck on the acceleration grids, resulting in the high grid power loading. To reduce the grid power loading, a thin plate for tuning the steering angle of the beamlets, called as "field shaping plate (FSP)" was newly designed and tested. Figure I.2.4-1 shows the vertical deflection angle of the outmost beamlets as a function of thickness of the FSP. To suppress the interceptions of the ion beam by the grids and the beam-limiters, a 1 mm thick FSP was chosen and installed on the JT-60U negative ion source. The use of the FSP reduces the grid power loading normalized by the drain power from the previous value of 7.5% to 6%, which is acceptable for the full specifications of the D^- ion beam [2.4-2].

In the JT-60U negative ion source, the electrons are mainly deflected downwards by the stray magnetic field. Some of the electrons are ejected from the ion source and dissipated on the inertial-cooled parts. Therefore, the ejected electron power should be quantified for long pulse operation. To measure the electron power, a thin stainless steel plate was set below the beam path, and the surface temperature of the plate was measured by infra-red camera (Fig. I.2.4-2(a)). Figure I.2.4-2(b) shows the typical temperature profile and the heat flux on the plate when 300 keV and 3.4 A beam was produced from only the central segment in the upper ion source. It is found that the highest heat flux from one segment is < 8 W/cm^2. Its total power load is ~2.6% of the drain power. For full beam with five segments, the highest heat flux is estimated to be ~37 W/cm^2 by assuming the heat flux distributions for the other segments to be the same as that measured from the central segment. This power loading can be removed readily by inertia cooling even for 30 s long pulse operation [2.4-3].

The D^0 beam power is restricted due to poor voltage holding capability of the ion sources. Even after sufficient conditioning, the achieved acceleration voltage is < 400 kV. Therefore, the voltage holding capability should be increased to the rated value of 500 keV. As the first step for the improvement of the voltage holding capability, the breakdown location of the JT-60 negative ion source has been examined. It is found that the breakdown location varied with the conditioning stage. In the early stage, breakdown occurs mainly in vacuum at gaps between the grids and their support frames with the total surface area of 2.5 m^2.

Careful observation shows that the conditioning gradually progresses with the breakdowns occurring at many different locations over the large surface area and with the reduction of the outgassing from the grids and the frames. This result suggests that the baking of the grids and frames would be effective to shorten the conditioning time. Over ~400 kV after conditioning of several months, the breakdown location is changed to the surface of the FRP insulator with an inner diameter of 1.8 m. It is recently found in Saitama University that the flashover voltage of a low outgassing epoxy resin (~10^{-4} Pa·m/s) is twice higher than that of the conventional one. The use of the low outgassing epoxy resin is expected to improve the voltage holding capability [2.4-4, 5].

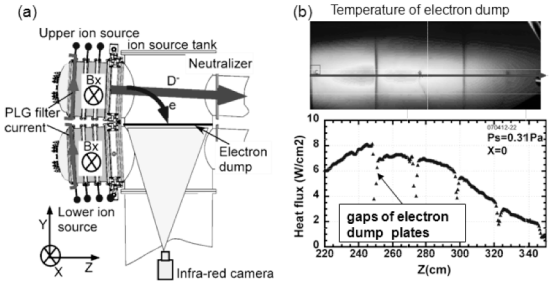

Fig. I.2.4-2(a) Set up of electron deposition measurement, (b) temperature and heat flux profiles at the electron dump.

References

2.4-1 Hanada, M., *et al., Rev. Sci. Instrum.* **79**, 02A519 (2008).

2.4-2 Ikeda, Y., *et al.,* "Recent R&D activities of negative ion based ion source for JT-60 SA," to be published in *IEEE Transactions on Plasma Science*, 2008.

2.4-3 Kamada, M., *et al., Rev. Sci. Instrum.* **79**, 02C114 (2008).

2.4-4 Hanada, M., *et al.,* "Power loading of electrons ejected from the JT-60 negative ion source," to be published in *IEEE Transactions on Plasma Science*, 2008.

2.4-5 Kobayashi, K., *et al.*, "Conditioning characteristic of DC 500 kV large electro-static accelerator in negative-ion-based NBI on JT-60U," *Proceedings of 23rd international symposium on Discharges and Electrical Insulation in Vacuum,* Bucharest, 2008.

2.5 Radio-Frequency Heating System

The FY2007 was quite fruitful year for the JT-60U radio-frequency (RF) heating system. Pulse length injected to the plasma by the electron cyclotron heating (ECH) system reached 30 s of the middle term (-2009) objective over the 25 s of the annual objective. Moreover in the ECH system, the world highest power output of 1.5 MW for 1 s was achieved by a gyrotron to the dummy load. Performance of the RF heating system has been constantly improved to extend the parameter region of experiments.

2.5.1 Long-Pulse Operation of the ECH System

The extension of the pulse duration of the ECH system has been tried to enhance the plasma performance in the recent experiment campaign in JT-60U focusing on long sustainment of high performance plasmas. Improvements of the vacuum pumping system of the transmission lines has been carried out in order to avoid pressure rise in the transmission lines due to temperature rise of the components. Vacuum pumping unit was installed at the Matching Optics Unit (MOU) individually for each transmission line. By means of the techniques of controlling heater current and anode voltage during the pulse to keep the oscillation condition, pulse duration of 30 s at 0.4 MW (at gyrotron) has been achieved as shown in Fig. I.2.5-1. Temperature increase of the transmission line components shows availability of the present system for 100 s operation in JT-60SA only for one shot. While upgrade of the cooling system of waveguides will be required to repeat 100 s operations.

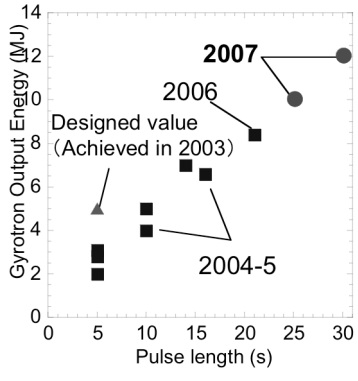

Fig. I.2.5-1 Extension of pulse duration of ECH system.

2.5.2 High Power Test of the Gyrotron

Improvements of the ECH system (1 MW for 5 s per unit) had been performed until FY2006 toward the higher power and the longer pulse. A Si_3N_4 ceramic DC-break was introduced into a gyrotron instead of an alumina ceramic DC-break due to the higher thermal strength. In order to avoid heating of a bellows which enables to move the last mirror in the gyrotron, a cover

was installed around the bellows to reflect stray-RF. Cooling water of a cavity wall was increased by about 20 %. Moreover, a high-power dummy load system (1.5 MW, CW) was developed to measure the oscillation power from the gyrotron. Those improvements enabled the ECH system to try high power oscillation up to 1.5 MW. In July of 2007, 1.5 MW for 1 s oscillation was achieved for the first time by means of fine optimization of the oscillation parameters as shown in Fig. I.2.5-2 [2.5-1]. The pulse length was not limited by any interlock signals. Therefore, it will be possible to obtain a longer pulse by making more fine adjustments.

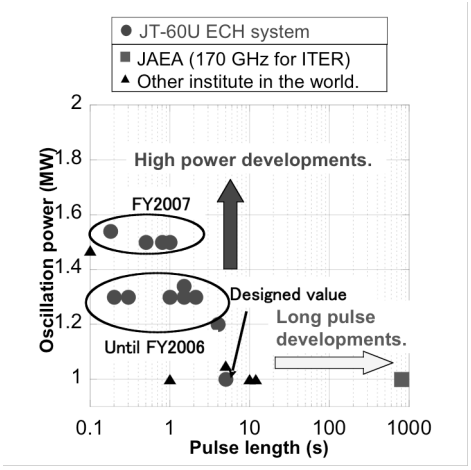

Fig. I.2.5-2 Oscillation power versus pulse length achieved in the world (power of over 1 MW and pulse length of over 0.1 s).

2.5.3 Improvement and Performance of the LHRF System

The LHRF (Lower Hybrid Range of Frequency) experiments such as real-time control of plasma current profile were performed. In FY 2006, 6-modules out of 8-modules of the launcher had been used because of damage at the launcher mouth due the malfunction of the arc detector in 2005. In the August of 2007, one of the heavily damaged mouths was repaired carefully from inside of the vacuum vessel of JT-60U, and the protection function against the arcing was upgraded with a new infrared camera watching at the launcher mouth from a tangential port. The conditioning operation for the launcher having 7-modules started in September and the injected power was reached ~ 2 MW in March 2009. The improvement of the power from the achievement of 1.6 MW in 2006 was 1.25 which was more than estimation (1.17~7/6) by a recovered module as shown in Fig. I.2.5-3.

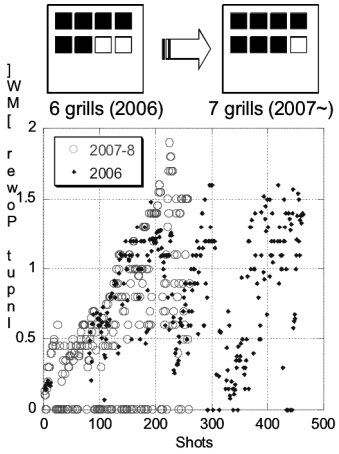

Fig. I.2.5-3 Power increase in LHRF system after repairing one of the damaged modules in the launcher.

Reference

2.5-1 Kobayashi, T., *et al., Plasma Fusion Res.*, **3**, 014 (2008).

2.6 Diagnostics Systems

2.6.1 Real-Time Measurement and Feedback Control of Ion Temperature Profile and Toroidal Rotation

Toward the steady-state operation with high beta and high thermal confinement, the real-time measurement and feedback control systems have been developed.

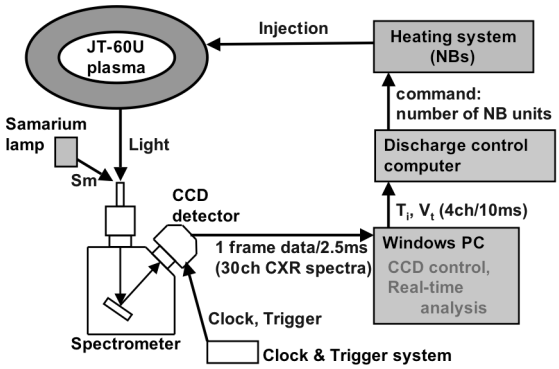

Fig. I.2.6-1 Schematic diagram of CXRS system for real-time feedback control.

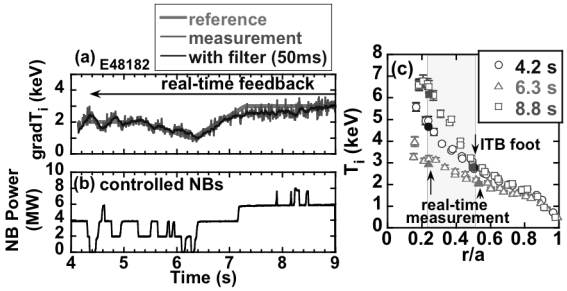

Fig. I.2.6-2 (a) Reference *grad-T_i* and measured *grad-T_i*. (b) Injected units of controlled NB heating. (c) Radial profiles of T_i with measurement point (solid symbols).

A fast charge exchange recombination spectroscopy (CXRS) system has been developed for the real-time measurement and feedback control of ion temperature (T_i) profile and toroidal rotation velocity (V_t) [2.6-1]. In order to control T_i and V_t in real-time, the charge exchange recombination spectroscopy with high time resolution, the real-time processor system, and the real-time control system have been developed (Fig. I. 2.6-1). Utilizing this system, real-time control of the T_i gradient has been demonstrated with NBs at high beta plasmas (β_N~1.6-2.8). The strength of the internal transport barrier is controlled (Fig. I. 2.6-2). Moreover, the real-time control of V_t has been demonstrated from counter to direction. Then the behavior of ELM changed by controlling the V_t.

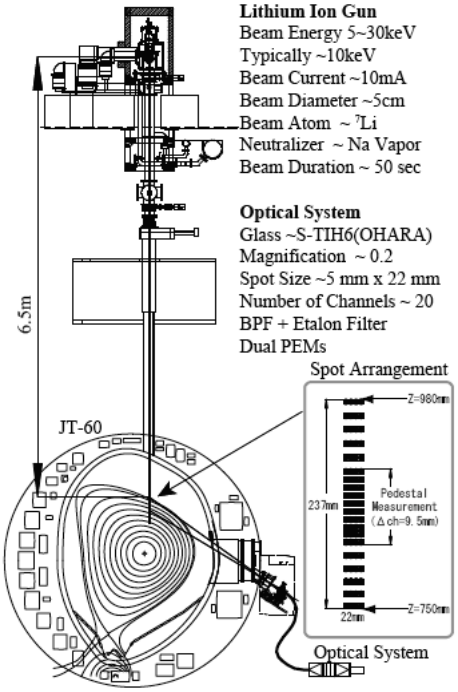

Fig. I.2.6-3 Lithium beam probe system on JT-60U. Neutral lithium beam is injected to JT-60U via 6.5 m beam line. A beam monitor is installed in the middle of the beam line.

2.6.2 Zeeman Polarimetry using Lithium Beam Probe for Edge Current Measurement

A lithium ion beam probe has been developed for edge current measurement (Fig. I.2.6-3). A lithium ion gun has been designed by the numerical simulation taking the space charge effects into account because a Zeeman polarimetry requires low beam divergence angle. A porous tungsten disk heated by an electron beam is utilized for an ion emitter. The concave surface of the disk and a peaked heating profile of the electron beam are selected to make a beam focusing better [2.6-2]. Performances of the ion gun have been investigated on a test stand [2.6-3]. A beam current of 10 mA and a divergence angle of 0.2 degrees and equivalent current of 3 mA at the observation area are attained by the ion gun. Figure I.2.6-4 shows the obtained current is increased with the extracted current. Moreover, a long pulse operation of 50 seconds with beam current of 10 mA has been demonstrated. Then the ion gun has been installed and operated on JT-60U successfully. After beam conditioning, a first signal of the lithium beam emission (2 ^{2}S - 2 ^{2}P resonance line) has been obtained in JT-60U plasma. Adjusting etalon filters, the lithium beam probe system is operated for the edge current measurement.

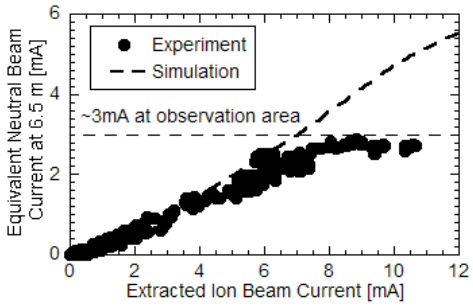

Fig. I.2.6-4 Experimental and simulation results of obtained current at 6.5 m. The saturation is caused by a shift of the neutralization position of an ion beam.

2.6.3 Polarization Interferometer for Thomson Scattering

Recently, the use of a polarization interferometer based on Fourier transform spectroscopy has been proposed for Thomson scattering diagnostics [2.6-4]. It is possible that this method alleviates some of the disadvantages of conventional grating spectrometers. Furthermore, this method delivers a simple and compact system. We are developing the polarization interferometer for Thomson scattering diagnostics with YAG laser to demonstrate the proof-of-principle. For thermal electrons, the optical coherence of the Thomson scattered light at an appropriately chosen optical path delay, is a unique function of T_e and n_e. The detection system utilizes a single bandpass filter combined with imaging optics and dual detectors to simultaneously observe both dark and bright scattered light interference fringes. The normalized intensity difference between the bright and dark interference fringes gives a direct measure of T_e. A

schematic of the polarization interferometer for Thomson scattering diagnostics is shown in Fig. I.2.6-5. Scattered light is collected and introduced to the polarization interferometer through a fiber-optic bundle. This polarization interferometer consists of an objective lens as the fiber coupling optics, a band pass filter, a polarizer, a birefringent plate which gives optical path delay, a Wollaston prism, an imaging optics to detector, and dual APD (silicon avalanche photodiode) detectors. Since proof-of-principle tests will be carried out in TPE-RX using the existing YAG laser Thomson scattering system before experiments in JT-60U, parameters for design of a prototype polarization interferometer are fixed as follows: $T_e \leq 1$ keV, $n_e \geq 5\times10^{19}$ m^{-3}, scattering angle 90°. In an initial test using a blackbody radiation source, the magnitude of the change in fringe visibility agrees with the numerical calculation. This result confirms that, following suitable calibration, we will be able to sense visibility changes due to changes in the electron temperature.

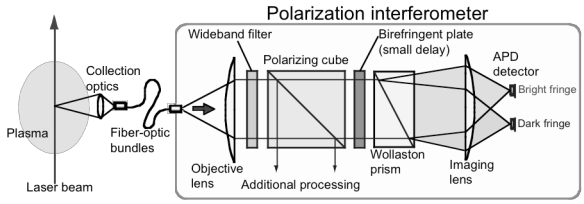

Fig. I.2.6-5 Schematic of a polarization interferometer for Thomson scattering diagnostics.

References

2.6-1 Yoshida, M., *et al*., "Real-time measurement and feedback control of ion temperature profile and toroidal rotation using fast CXRS system in JT-60U," submitted to *Fusion Eng. Des*.

2.6-2 Kojima, A., *et al.*, *Plasma Fusion Res.,* **2**, S1104 (2007).

2.6-3 Kojima, A., *et al*., "Development of a High-Brightness and Low-Divergence Lithium Neutral Beam for a Zeeman Polarimetry on JT-60U," to be published in *Rev. Sci. Instrum*.

2.6-4 Hatae, T., *et al*., *Plasma Fusion Res*., **2**, S1026 (2007).

2.7 Safety Assessment

2.7.1 Application Works for Operational Modifications on JT-60

Based on the law concerning prevention from radiation hazards due to radioisotopes, etc., licensing procedures have been done regarding two items below.

(1) Surface Analyses of Ferritic Steel First Wall Tiles

In FY2005, 1122 ferritic steel (8Cr-2W-0.2V) tiles were installed at the out board first wall inside the vacuum vessel in order to reduce toroidal magnetic field (TF) ripples. For the surface analysis of these tiles removed from the vessel, an application for use of radioisotopes induced on the tiles has been filed to the radiation regulation division of Ministry of Education, Culture, Sports, Science and Technology (MEXT) in March 2007 and was subsequently permitted in April.

(2) Extension of Neutral Beam Injection Time

Pulse lengths of neutral beam injectors (NBI) were extended from 30 s to 60 s in order to meet experiments with long pulse plasma discharges up to 60 s. An application for the NBI pulse extension was permitted in June 2007 and the experiments started in September elongating the beam pulses.

2.7.2 Radiation Safety Assessment for JT-60 Decommissioning

(1) Radiational Exposure during Decommissioning

Potential radiational exposure to workers in the torus hall during disassembly of the JT-60 was preliminarily assessed for internal and external radiation doses together with procedures of the disassembly. It was found that uses of the method of bubble lubricant during diamond wire sawing and of some Green Room facilities for cutting the main structures including the vacuum vessel sectors shall limit spread of contamination and eliminate pollutant in the torus hall, greatly contributing to minimize their internal exposure. In external radiation exposure, a contact dose level was assessed less than 20 μSv/h inside the vacuum vessel at one year cooling time after a shutdown of JT-60, indicating an acceptable radiation environment for the workers. The amount of internal and external exposure doses for the workers was expected to be 100 times less than that of the regal limit, 1mSv/week inside the controlled area.

(2) Storage and Management for Radio-Activated Materials Removed from Controlled Areas

From both points of view of resources saving and reusable nature of the materials, the radio-activated devices or structures replaced with new equipment are expected to be stored appropriately until the potential

clearance rule is put into operation. It was found that some additional controlled on-site facilities or areas other than the existing JT-60 storage building are required for their storage and management.

(3) Estimation of Low Level Waste by a Regulatory Clearance.

Low level waste of the JT-60U has been estimated by a regulatory clearance [2.7-1]. The JT-60U consists of main devices including a vacuum vessel, magnetic coils, heating devices such as neutral beam injectors and radio frequency systems. Those structural materials include copper, stainless steel, carbon steel, high manganese steel, inconel 625, ferritic steel, lead and others. The gross weight of the devices is about 6,400 tons.

Neutron and gamma-ray fluxes during an operation were calculated with the ANISN code. Induced activity of the materials was calculated by the ACT-4 code in the THIDA-2 code system at various times after an operational shutdown. The total neutron yields was assumed to be 1.14×10^{20} n for fourteen operation years of the JT-60U.

Figure I.2.7-1 shows time evolutions of the volume of activated materials after the shutdown. The report of IAEA RS-G-1.7 [2.7-2] was referred to compare clearance levels to the results of the activated nuclides induced on the structural materials. The amount of the low level waste of which activation levels exceed the clearance levels is about 5000 tons just after the shutdown. On the other hand, the amount below the clearance levels is 1400 tons.

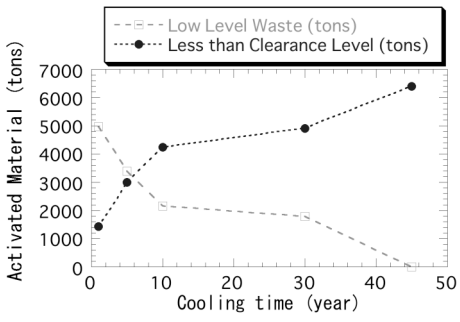

Fig.I.2.7-1 Time evolutions of the volume of activated materials at the various cooling time after the shutdown.

The former decreases with time and vanishes at 45 years after the shutdown. Asymmetrically, the latter increases year by year as shown in the figure. In JT-60U, stainless steel SS316 of about 50 tons, of which Cobalt content is 0.2 wt%, are used for the base plates of the first wall inside the vacuum vessel. The major source of the activated level of the waste, therefore, takes about 45 years until less than the clearance level due to the long half-time nuclide ^{60}Co.

2.7.3 Nuclear Shielding Assessment using ATTILA Code

Neutron fluxes of a tokamak fusion device with a cryostat were calculated with the three dimensional (3D) nuclear shielding code, ATTILA. ATTILA is a numerical modeling and simulation code designed to solve the 3D multi-group Sn transport equations for neutrons, charged particles, and infrared radiation on an unstructured tetrahedral mesh. It uses a traditional Sn source iteration technique for solving the first order form for the transport equation.

Figure I.2.7-2 depicts a demonstration result of the total neutron flux distribution for a typical superconducting tokamak with a cryostat. From the results, ATTILA has proved to be useful to analyze the nuclear shielding properties especially for the port or duct streaming of an experimental building.

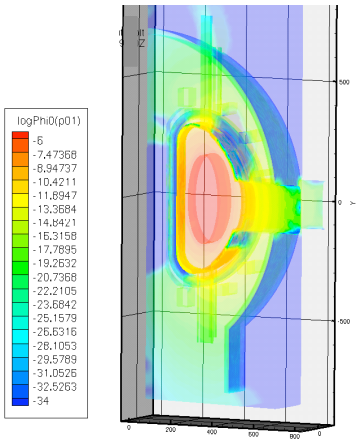

Fig. I.2.7-2 Total neutron flux distribution of a typical superconducting tokamak device (by ATTILA code).

2.7.4 Development of High Heat Resistant Neutron Shielding Resin

In fusion tokamak devices, temperature near a vacuum vessel is expected to rise up to ~300 ^{o}C, because the wall conditioning by vessel baking is of crucial importance for plasma discharge operations.

Shielding materials such as polyethylene and concrete are widely used. Polyethylene is the most

popular resin for neutron shielding, but the heatproof temperature is fairly low. Concrete is not suitable for the additional shielding material in the restricted space around the center of the devices, while it endure a high temperature environment. The heatproof neutron shielding resins such as KRAFTON-HB4 [2.7-3] and EPONITE [2.7-4] had been developed by 2004. KRAFTON-HB4 was the epoxy-based resin that contains boron to reduce the production of secondary gamma rays. It was developed for future FBR shielding materials. KRAFTON-HB [2.7-5] was improved one with the aim of suppressing the nuclear heating of superconducting coils of the DD nuclear fusion devices. The maximum heatproof temperature of it was 150 ^{o}C. EPONITE was the Colemanite and epoxy-based resin that contains boric acid. It was developed for a medical equipment PET cyclotron with a heatproof temperature of 200 ^{o}C.

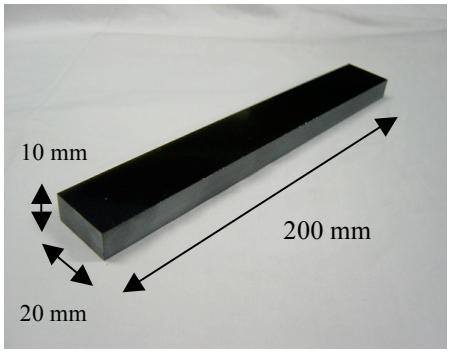

Fig. I.2.7-3 A test piece of the new epoxy-based neutron shielding resin before gel formation (Present study includes the result of "Research and Development for High Heat Resistant of Gel-type Neutron Shielding Resin" entrusted to Japan Atomic Energy Agency by MEXT).

Based on the previously demonstrated results above, we started the development of new resins against much higher temperature range up to 300 ^{o}C, and successfully produced the new boron-loaded and heat-resisting resin in 2005 [2.7-6]. The heatproof temperature has been improved by an appropriate mixing of stiffening materials with the epoxy-based resin. In 2007, the research and development of the Gel-type heat-resisting resin were initiated in response to the need for more flexible and light shielding materials expected to be useful in situations where an additional shielding is required in narrow or hard-to-reach areas such as locations of diagnostic collimators [2.7-7]. The results obtained to date have been limited to that of a solid-state sample. The glass transition temperature, an indicator of the heatproof temperature, in the specimen was obtained up to 320 ^{o}C. A test sample piece of the new resin before gel formation is shown in Fig. I.2.7-3.

References

2.7-1 Sukegawa, A. M., *et al.*, "Estimation of Low Level Waste by a Regulatory Clearance in JT-60U Fusion Device," *15th International Conference on Nuclear Engineering (ICONE-15)* , April 22-26, 2007, Nagoya, JAPAN.

2.7-2 IAEA, SAFETY GUIDE, No. RS-G-1.7.

2.7-3 Ueki, K., *et al*., *Nucl. Sci. and Eng*., **124**, 455 (1996).

2.7-4 Okuno, K., *Radiation Protection Dosimetry*, **115**, 1-4, 258-261 (2005).

2.7-5 Morioka, A., *et al., J. Nucl. Sci. Technol.,* Supplement **4**, 109-112 (2004).

2.7-6 Morioka, A., *et al., J. Nucl. Mater.*, **367-370**, 1085 (2007).

2.7-7 Sukegawa, A. M., *et al.*, "High Heat Resistant Neutron Shielding Resin, " *11th International Conference on Radiation Shielding (ICRS-11)* , April 13-18, 2008 , Callaway Gardens, Pine Mountain, Georgia, US.

3. Domestic and International Collaborations

3.1 Domestic Collaboration

JT-60U was assigned as a core national device for joint research by the Nuclear Fusion Working Group of the Special Committee on Basic Issues of the Subdivision on Science in the Science Council of MEXT in January 2003. Using the JT-60 tokamak and other facilities, JAEA has performed research collaboration with the universities and National Institute for Fusion Science (NIFS). Accordingly, the joint experiments on JT-60 between JAEA and the universities by assigning university professionals as leaders of research task forces has been successful. The number of collaborators had increased significantly since FY 2003, and it is kept around 150 for recent five yeas as shown in Fig. I.3.1-1.

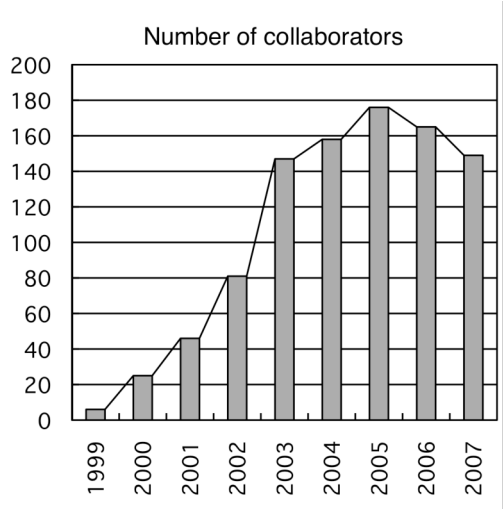

Fig.I.3.1-1 Evolution of number of collaborators in the JT-60 joint research.

Table I.3.1-1 Number of research subjects of the JT-60 joint research according to category in FY 2007.

Category	No. of research subjects
Performance improvement	3
Transport	3
Pedestal	2
MHD/High energy particles	7
Divertor/SOL	4
Plasma-material interaction	3
Diagnostics	3
Heating system	2
Total	27

In FY2007, 149 persons participated, who came from 19 research organs in Japan. Two leaders, one from university or NIFS and the other from JAEA, occupy each subtheme. The number of research subjects of the joint research was 27 in total in FY 2007, categories of which are shown in Table I.3.1-1. Twenty-two journal papers and 1 paper in conference proceedings were published as a result of the joint research in FY 2007.

3.2 International Collaboration

Status of collaborative research based on the IEA Implementing Agreement on cooperation on the Large Tokamak Facilities is described first. The result of personnel exchanges among Japan, US and Europe are as follows. The number of personnel exchanges, to which JAEA relates, is 11 in total. There are two personnel exchanges from JAEA to EU, 3 from EU to JAEA, 0 from JAEA to US, and 10 from US to JAEA. JT-60U contributes to ITPA/IEA inter-machine experiments. There are 3 to 7 experiments for each Topical Groups. In 2007, 4 related papers were published in journals and 10 related presentations are accepted for IAEA Fusion Energy Conference in 2008.

As for remote collaboration, JAEA provides JT-60 data within the scope of the proposal document sheet (PDS). There are 8 active PDS (3 with EU, 2 with US, 2 with AUG, 1 with EAST).

Remote experimental system (RES) with high network security has been developed in JT-60U. The remote experimental system is produced by personal authentication with a digital certificate and encryption of communication data to protect the JT-60U supervisory control system against illegal access. Remote experiment in JT-60U was demonstrated from Kyoto University (Japan) in 2006 and internationally from IPP Garching (Germany) in 2007 on the occasion of an neo-classical tearing mode stabilisation similarity experiment between JT-60U and ASDEX Upgrade. RES was successfully verified on its authentication, encryption and turn around time. The gateway server blocked all access except the IT-Based Laboratory InfraStructure (ITBL-IS) and Atomic Energy Grid Infrastructure (AEGIS) client certificate, and we confirmed that its authentication mechanism was working properly. The use of packet capture software proved that packets were encrypted. The amount of

communication data to display a discharge condition reference page was measured with packet capture software. Throughput was calculated from the window size and the measured Round Trip Time (RTT), and the turn around time was measured from the amount of communication data and throughput. When RTT was 290 milliseconds, the turn around time was 4.13 seconds for the remote experiment from IPP Garching. This gave the applicable response to the remote participants, and it provided mostly the same environment as the onsite researcher. Results are great advances towards the remote experiment in ITER.

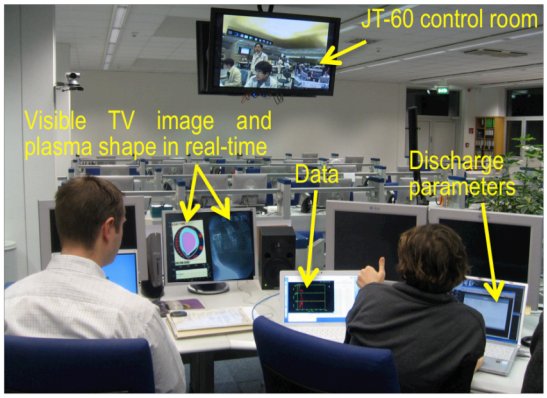

Fig.I.3.2-1 Remote experiment of JT-60 from IPP Garching.

II. Theory, Simulation and Modeling

For the NEXT (Numerical Experiment of Tokamak) project in 2007, a new conservative gyrokinetic full-*f* Vlasov code has been developed in order to realize a long time simulation. Zonal field generation was investigated in finite beta ion temperature gradient driven turbulence by global Landau-fluid simulations. Also, nonlinear MHD simulations found the Alfven resonance effects on the evolution of magnetic islands driven by an externally applied perturbation. The distribution of eigenvalues of the resistive MHD equations in the complex plane has been re-investigated for smaller resistivity than the previous works, and a numerical matching scheme for linear MHD stability analysis was proposed in a form offering tractable numerical implementation. A conjugate variable method was formulated in order to apply the Hamilton-Lie perturbation theory to a system of ordinary differential equations that does not have the Hamilton dynamic structure.

The development of the integrated modeling is promoting in order to study complex behaviors of JT-60U plasmas and to predict the performance of future burning plasmas. Several kinds of element codes have been developed for the integrated modeling; MHD stability code, integrated SOL/divertor code, fundamental SOL/divertor code of the particle model, heating and current drive analysis code, and integrated transport code TOPICS-IB. Achievements in 2007 with the use of these codes are described below in section 2.

1. Numerical Experiment of Tokamak (NEXT)

1.1 Magnetohydrodynamic (MHD) Theory and Simulation

1.1.1 Alfven Resonance Effects on an Externally Driven Magnetic Island in Rotating Plasma

The Alfven resonance effects on the magnetic island evolution driven by an externally applied perturbation were investigated. In a low viscosity regime, perturbed current sheets form at the Alfven resonance surfaces (Fig.II.1.1-1), which differ from the radial position of the magnetic neutral surface. Therefore, the sheets exist outside the inner non-ideal layer, defined for the non-rotating plasma. According to this perturbed current sheet profile, the total torque, which affects the plasma, extends wider than the radial position of the Alfven resonance. It is found that the radial position of an

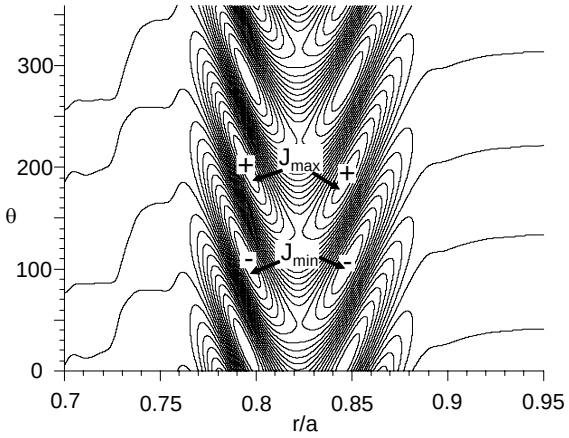

Fig. II.1.1-1 Two-dimensional profile of the perturbed current obtained for the rotation frequency $\Omega=0.02\pi$.

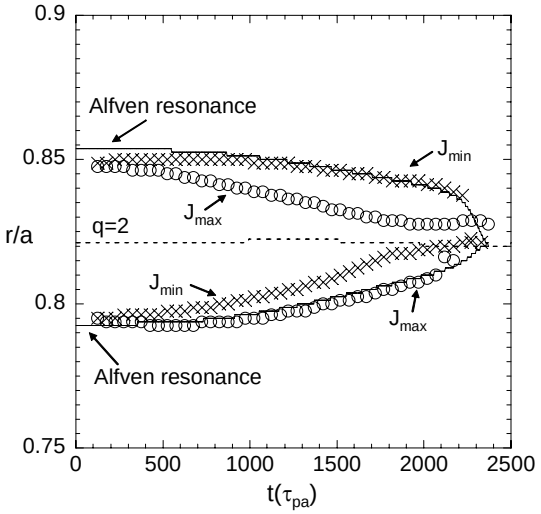

Fig. II.1.1-2 Time evolution of the radial position of the Alfven resonance and the maximum and minimum of the perturbed current.

Alfven resonance moves to the magnetic neutral surface and causes the rapid growth of a driven magnetic island (Fig.II.1.1-2). This is because the background flow is damped by the appearance of the magnetic island, which operates torque on the plasma. These features are inconsistent with former theoretical assumptions, which enable using the asymptotic matching method to estimate the force balance and the critical value of the external perturbation, beyond which the driven magnetic island grows rapidly [1.1-1].

1.1.2 MHD Spectrum of Resistive Modes

The resistive MHD spectrum is investigated in detail by solving the eigenvalue problem of the reduced MHD equations in cylindrical tokamak plasmas, in particular for asymptotically smaller resistivity than the previous works. In the presence of the resistivity, the eigenvalues

of linear resistive MHD modes are not necessarily purely real, but have an imaginary part. The eigenvalues are classified as the continuum spectrum of dumping modes on the negative real axis, the discrete spectrum of oscillatory and dumping modes on the complex plane, and the discrete spectrum of unstable modes on the positive real axis. For a wide range of the resistivity parameter ($\eta=10^{-4} \sim 1.5\times10^{-6}$), the shape and location of eigenvalue distribution for m/n=1/1 modes which have the same resonant surface at q=1 is almost independent of the resistivity, although the density of the eigenvalues increases. However, it is found that for a further small resistivity regime, the eigenvalue distribution changes sensitively depending on the resistivity [1.1-2].

1.1.3 Numerical Matching Scheme for Linear MHD Stability Analysis

A new matching scheme for linear MHD stability analysis is proposed in a form offering tractable numerical implementation. This scheme divides the plasma region into outer regions and inner layers, as in the conventional matching method. However, the outer regions do not contain any rational surface at their terminal points; an inner layer contains a rational surface as an interior point. The Newcomb equation is therefore regular in the outer regions. The MHD equation employed in the layers is solved as an evolution equation in time, and the full implicit scheme is used to yield an inhomogeneous differential equation for space coordinates. The matching conditions are derived from the condition that the radial component of the solution in the layer is smoothly connected to those in the outer regions at the terminal points. The proposed scheme was applied to the linear ideal MHD equation in a cylindrical configuration, and was proved to be effective from the viewpoint of a numerical scheme [1.1-3].

1.1.4 Conjugate Variable Method in the Hamilton-Lie Perturbation Theory -Applications to Plasma Physics-

The conjugate variable method, which is an essential ingredient in the path-integral formalism of classical statistical dynamics, was used in order to apply the Hamilton-Lie perturbation theory to a system of ordinary differential equations that does not have the Hamilton dynamic structure. The method endows the system with the Hamilton dynamic structure by doubling the unknown variables; hence the canonical Hamilton-Lie perturbation theory becomes applicable to the system. The method was applied to two classical problems known in plasma physics to demonstrate the effectiveness and to study the property of the method: one is a non-linear oscillator that can explode; the other is the guiding center motion of a charged particle in a magnetic field [1.1-4].

References

1.1-1 Ishii, Y., *et al*., "Formation and long term evolution of the externally driven magnetic island in rotating plasmas," to be published in *Plasma and Fusion Research*.

1.1-2 Matsumoto, T., *et al*., *Proc. 6th General Scientific Assembly of the Asia Plasma and Fusion Association* (India, 2007).

1.1-3 Kagei, Y., *et al*., "Numerical matching scheme for linear magnetohydrodynamic stability analysis," to be published in *Plasma and Fusion Research*.

1.1-4 Tokuda, S., *et al.*, "Conjugate variable method in the Hamilton-Lie perturbation theory -applications to plasma physics-," submitted to *Plasma and Fusion Research*.

1.2 Plasma Turbulence Simulation

1.2.2 Development of Non-Dissipative Conservative Finite Difference Scheme for Gyrokinetic Vlasov Simulation

A new conservative gyrokinetic full-*f* Vlasov code is developed using a finite difference operator which conserves both the L1 and L2 norms. The growth of numerical oscillations is suppressed by conserving the L2 norm, and the code is numerically stable and robust in a long time simulation. In the slab ITG turbulence

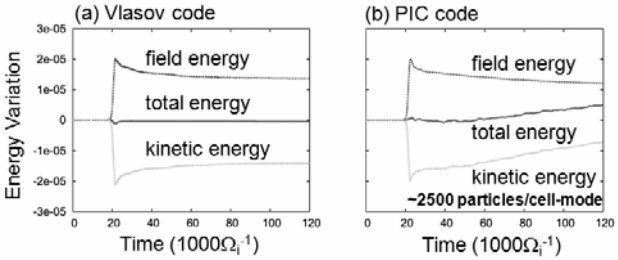

Fig. II.1.2-1 Comparisons of the time histories of the total, field, and kinetic energy in long time ITG turbulence simulations using (a) Vlasov and (b) PIC simulations with almost the same computational costs. In (a), the total particle number is exactly conserved and the total energy conservation is dramatically improved using a new conservative scheme.

simulation, the energy conservation and the entropy balance relation are confirmed, and solutions are benchmarked against a conventional δf particle-in-cell (PIC) code. The results show that the exact particle number conservation and the good energy conservation in the conservative Vlasov simulation are advantageous for a long time micro-turbulence simulation (Fig. II.1.2-1). In the comparison, physical and numerical effects of the $v_{//}$ nonlinearity are clarified for the Vlasov and PIC simulations [1.2-1, 2].

1.2.1 Zonal Field Generation and Its Effects on Zonal Flow and Turbulent Transport

Global Landau-fluid simulations of ion temperature gradient (ITG) driven turbulence have been performed for finite beta tokamak plasmas, where the beta value is a ratio of plasma pressure to magnetic pressure. The ITG turbulence can drive zonal magnetic fields as well as zonal flows in finite beta cases. The Reynolds stress drives zonal flows and the geodesic transfer effect acts as a sink for zonal flows usually. It is found that the Reynolds stress and the geodesic transfer effect change their roles at low order rational surfaces where zonal magnetic fields are generated the most strongly. This is not observed in electrostatic (zero beta) simulations. Effects of the zonal magnetic fields on the zonal flows and the turbulent transport are limited in a small region around a low order rational surface at least in a low beta regime where the ITG mode is dominant. The zonal magnetic fields, however, may affect the zonal flows and the turbulent transport in a high beta regime because amplitude of the zonal magnetic fields increases with the beta value [1.2-3].

References

1.2-1 Idomura, Y., *et al*., *J. Comput. Phys.* **226**, 244 (2007).

1.2-2 Idomura, Y., *et al*., *Commun. Nonlinear Sci. Numer. Simul.* **13**, 227 (2007).

1.2-3 Miyato, N., *et al*., *Proc. 34th EPS Plasma Phys. Conf.* (Poland, 2007), p4.043.

2. Integrated Modeling

2.1 MHD Stability – Effect of Equilibrium Properties on the Structure of the Edge MHD Modes in Tokamaks –

The ideal MHD stability code MARG2D has been extended to estimate a growth rate of the MHD mode under the incompressible assumption by introducing the plasma inertia [2.1-1]. With this extension, MARG2D realizes not only to identify the stability boundary of ideal MHD modes, but also to investigate physical properties of unstable MHD modes in detail.

By using this extended MARG2D, effects of the pressure profile and the current density profile inside the top of pedestal and that of the plasma shape on the expansion of the structure of the unstable edge MHD mode are investigated numerically [2.1-2]. The radial structure of the edge MHD mode is expanded by spreading the envelope of the edge ballooning mode due to increasing the pressure gradient inside the top of pedestal. Moreover, the increase of the current density induces the decrease in the toroidal mode number of the most unstable mode, and this decrease also expands the structure of the unstable mode.

The mode structure is subject to expanding in strongly shaped plasmas. This is because the pressure gradient inside the top of pedestal can approach to the ballooning mode stability boundary and the current density increases enough to reduce the toroidal mode number of the most unstable mode. These increases of

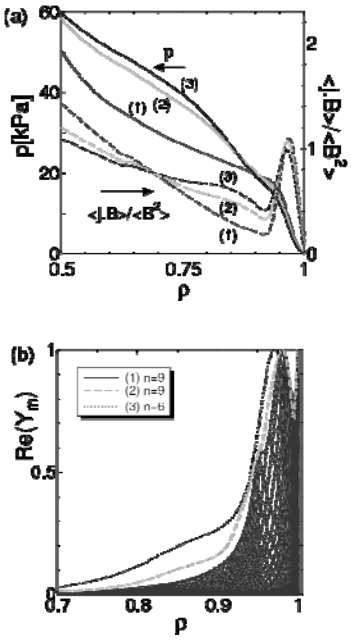

Fig. II.2.1-1 (a) Profiles of plasma pressure (solid line) and parallel current density (broken line) for three kinds of equilibria. The current density inside the top of pedestal increases due to the steep pressure gradient. (b) Radial structures of the most unstable MHD mode. Larger pressure gradient and current density inside the top of pedestal expand the structure of the unstable mode.

the pressure gradient and the current density destabilize the edge MHD mode and expand the mode structure.

References

2.1-1 Aiba, N., *et al.*, *J. Plasma Fusion Res.* **2**, 010 (2007).

2.1-2 Aiba, N., *et al.*, to be published in *J. Phys. Conf. Series* (2008).

2.2 SOL-Divertor

Divertor of tokamak reactors has four major functions, heat removal, helium ash exhaust, impurity retention, and density control. Such divertor performance strongly depends on the various physics, i.e. plasma transport, kinetic effects, atomic processes, and plasma-wall interactions. In order to understand complicated divertor physics and to predict divertor performance, JAEA has developed a series of divertor codes, onion-skin modeling, SOLDOR, NEUT2D, IMPMC, PARASOL, 5-point divertor code coupled with a core transport code (TOPICS-IB), and Core-SOL-Divertor model (CSD).

The benchmark test of SOLDOR/NEUT2D code with B2/EIRENE code was attempted. The simulation study of JT-60SA divertor was carried out with B2/EIRENE and the difference between single-null and double-null configurations was confirmed [2.2-1].

The CSD model was developed to take into account impurity radiation and momentum loss in the divertor region and the divertor detachment was investigated [2.2-2].

2.2.1 Development of Integrated SOL/Divertor Code and Simulation Study

To predict the heat and particle controllability in the divertor of tokamak reactors and to optimize the divertor design, comprehensive simulations by integrated modeling allowing for various physical processes are indispensable. SOL/divertor codes have been developed in Japan Atomic Energy Agency for the interpretation and the prediction on behavior of SOL/divertor plasmas, neutrals and impurities [2.2-3]. The code system consists of the 2D fluid code SOLDOR, the neutral Monte-Carlo (MC) code NEUT2D, and the impurity MC code IMPMC. Their integration code "SONIC" is almost completed and examined to simulate self-consistently the SOL/divertor plasmas in JT-60U. In order to establish the physics modeling used in fluid simulations, the particle simulation code PARASOL has also been developed.

Simulation studies using those codes are progressed with the analysis of JT-60U experiments and the divertor designing of JT-60SA. The X-point MARFE in the JT-60U experiment is simulated. It is found that the deep penetration of chemically sputtered carbon at the dome for the detached phase causes the large radiation peaking near the X-point as shown in Fig. II.2.2-1. The pumping capability of JT-60SA is evaluated through the simulation. A guideline to enhance the pumping efficiency is obtained in terms of the exhaust slot width and the strike point distance. Transient behavior of SOL/divertor plasmas after an ELM crash is characterized by the PARASOL simulation; the fast-time-scale heat transport is affected by collisions while the slow-time-scale behavior is affected by the recycling.

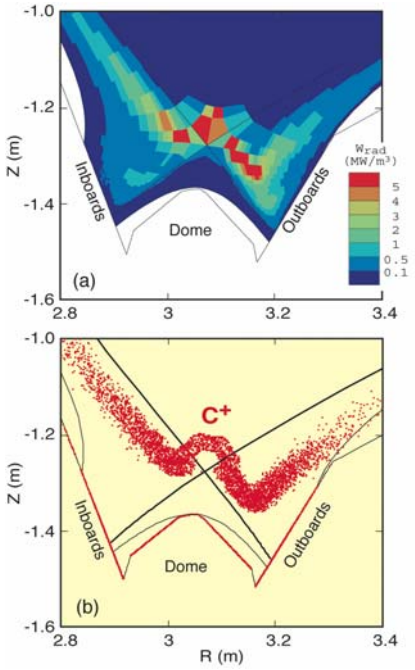

Fig. II.2.2-1 Simulation results of (a) carbon radiation profile and (b) C^+ ionization point distribution for X-point MARFE in JT-60U.

2.2.2 Extension of IMPMC Code toward Time Evolution Simulation

As a self-consistent modelling of divertor plasma and impurity transport, the SONIC code package has been developed. The key feature of this integrated code is to incorporate the impurity MC code, IMPMC. The MC approach is suitable for modelling of interactions between impurities and walls, including kinetic effects,

and the complicated dissociation process of hydro-carbons. The MC modelling, however, has the disadvantage for long computational time, large MC noise, and assumption of steady state. The first and second difficulties were solved by developing a new diffusion model and optimizing with a Message Passing Interface (MPI) on the massive parallel computer. The third subject is solved by extension of IMPMC code toward time evolution simulation. In time-dependent simulation with the MC code, a serious problem to increase number of test particles. The particle reduction method consisting of sorting the weights, pairing and Russian roulette has been proposed [2.2-4]. Sorting of the weights is indispensable to suppress the MC noise.

The divertor configuration in JT-60SA has been optimized from a viewpoint of the neutral recycling with SOLDOR/NEUT2D. In the near future, it will be further optimized from a viewpoint of the impurity control with the SONIC code package coupled with the above extended IMPMC.

References

2.2-1 Suzuki, Y., *et al., Contrib. Plasma Phys.* **48,** 169 (2008).

2.2-2 Hiwatari, R., *et al., Contrib. Plasma Phys.* **48,** 174 (2008).

2.2-3 Kawashima, H., *et al.*, *Plasma Phys. Control. Fusion* **49,** S77 (2007).

2.2-4 Shimizu, K., *et al., Contrib. Plasma Phys.* **48,** 270 (2008).

2.3 ELM Transport – Effect of Radial Transport Loss on the Asymmetry of ELM Heat Flux –

Large heat load on the divertor plate intermittently produced by ELMs is one of crucial issues for the tokamak fusion reactor research and development. The imbalance in the ELM heat loads on in-out divertor plates is also the problem. It has been reported that the ELM heat deposition to the outer plate is larger than that to the inner plate in JT-60U, while in JET and ASDEX Upgrade the inner-plate heat deposition becomes larger than the outer-plate heat deposition. To understand the physics background of such complex behaviors of the ELM heat flux, the dynamics of SOL-divertor plasmas after an ELM crash is studied with a one-dimensional particle simulation code, PARASOL [2.3-1].

The ELM crash occurs off-centrally in the SOL region, and the ELM heat flux to the near divertor plate and that to the far divertor plate become asymmetric. The peak heat flux to the near plate is larger as compared to the far plate. The asymmetry in the peak heat flux increases with the connection-length ratio. The imbalance in the heat deposition, however, is small. The radial transport loss of ELM flux creates the asymmetry in the heat deposition, but the imbalance is still not large even for the large radial transport loss rate. The electron heat flux to the far plate brought by the SOL current is one of the causes of a small imbalance in the heat deposition. Another cause is the asymmetric SOL flow and its convective heat flux, whose stagnation point stays for a long period near the ELM crash location.

Reference

2.3-1 Takizuka T., *et al., Contrib. Plasma Phys.* **48,** 207 (2008).

2.4 Heating and Current Drive – Electron Cyclotron Current Drive in Magnetic Islands of Neo-classical Tearing Mode –

Electron cyclotron current drive (ECCD) is the effective method for stabilization of neo-classical tearing modes (NTM). The driven current is evaluated conventionally by the bounce averaged Fokker-Planck equation (BAFP), where the magnetic field is assumed to be axi-symmetric. When the magnetic islands are formed by NTMs, however, this assumption is incomplete and the validity of ECCD analysis based on the BAFP equation becomes questionable.

The ECCD in the magnetic island is studied numerically by a particle simulation [2.4-1]. Drift motion of electrons with Coulomb collisions and

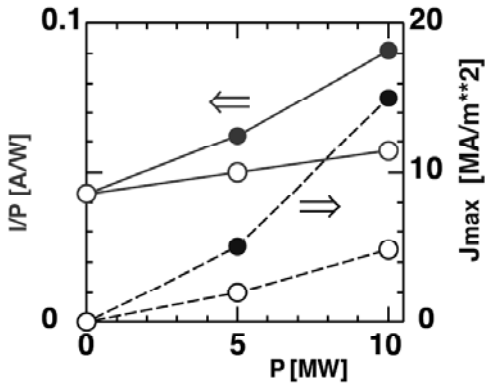

Fig. II.2.4-1 EC power dependence of EC current drive efficiency with the magnetic island (solid circle) and without island (open circle). The maximum of driven current density, J_{max}, is also shown by dashed line.

velocity diffusion due to the EC waves is tracked by using a Monte-Carlo technique. An EC resonance region is located around the O-point and localized along the toroidal direction. It is found that the driven current is well confined in the helical flux tube including the EC resonance region and the current channel looks like a helical "Snake". Figure II.2.4-1 shows the dependence of EC current drive efficiency I/P on the EC power P. Plasma parameters are the followings; the magnetic island of m/n = 2/1 is located around 0.5m in the minor-radius direction, where $n_e = 3\times10^{19}\mathrm{m}^{-3}$, T_e = 10keV and $Z_{eff} = 1$. The major radius is 3.5m and the EC wave frequency is 125GHz (2nd harmonic resonance). The current drive efficiency with the magnetic island is larger than that without magnetic island and is enhanced by the increase of the EC power. The driven current profile in the magnetic island becomes steep around the O-point with the increase of P. These results are caused by the good confinement of EC resonant electrons inside the island like "Snake" and the nonlinear kinetic effect due to the high EC power density.

Reference

2.4-1 Hamamatsu K., *et al., Plasma Phys. Control. Fusion* **49,** 1955 (2007).

2.5 Integrated Simulation

Integrated simulation models have been developed on the basis of the research in JT-60U experiments and first-principle simulations in order to clarify complex features of reactor-relevant plasmas. The integrated model of edge-pedestal, SOL and divertor clarified that the steep pressure gradient inside the H-mode pedestal top enhances the ELM energy loss [2.5-1]. A new one-dimensional core transport code, which can describe the radial electric field and plasma rotations, has been developed [2.5-2]. Success in these analysis and development leads to the further effective study of complex plasmas and methods to control the integrated performance.

2.5.1 Integrated ELM Simulation with Edge MHD Stability and Transport of SOL-Divertor Plasmas

The energy loss due to ELMs has been investigated by using an integrated simulation code TOPICS-IB based on a 1.5 dimensional core transport code with a stability code for the peeling-ballooning modes and a transport model for SOL and divertor plasmas. In the previous study, the TOPICS-IB successfully simulated transient behaviors of an H-mode plasma and clarified the mechanism of the collisionality dependence of the ELM energy loss. The ELM energy loss, however, was less than 10% of the pedestal energy.

The effect of the pressure gradient inside the pedestal top, P'_{inped}, on the ELM energy loss is examined [2.5-1]. Figure II.2.5-1(a) shows profiles of the total pressure, P, at the ELM onset. The transport is reduced to the ion neoclassical level in the pedestal region for case A, and the transport is additionally reduced inside the pedestal top for other cases B-D. The pedestal top is located at ρ = 0.925 for all cases and P'_{inped} becomes steeper in order of A, B, C, D. Even for the case A, P'_{inped} is as the same as that observed in JT-60U. Profiles of the ELM enhanced diffusivity, χ_{ELM}, in the cases A-D are shown in Fig. II.2.5-1(b). The steep pressure gradient broadens eigenfunctions of unstable modes and the region of the ELM enhanced transport. Figure II.2.5-1(c) shows the ELM energy loss, ΔW_{ELM}, normalized by the pedestal energy, W_{ped}, as a function of P'_{inped}/P'_{ped} where P'_{ped} is the pedestal pressure gradient. In the case A, the ELM energy loss is less than 10% of the pedestal energy and is comparable with those in JT-60U. The steep pressure gradient inside the pedestal top enhances the ELM energy loss. The density collapse, which is not considered here, enhances the values of

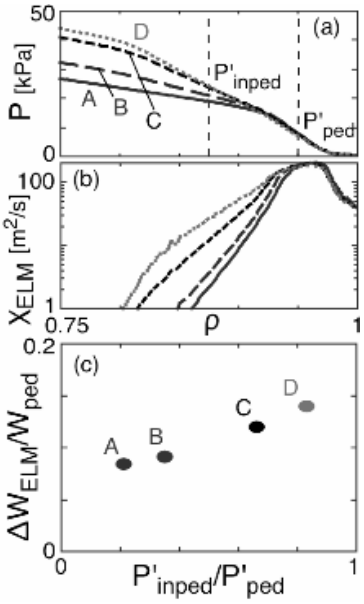

Fig. II.2.5-1 (a) Pressure profiles at ELM onset and (b) χ_{ELM} for cases A-D. (c) Dependence of $\Delta W_{ELM}/W_{ped}$ on P'_{inped}/P'_{ped}. Definition positions of P'_{inped} and P'_{ped} are shown in (a).

$\Delta W_{ELM}/W_{ped}$ by about 50% under the assumption of the similar collapse to the temperature one. The ELM energy loss in the simulation becomes larger than 15% of the pedestal energy, as is shown in the database of multi-machine experiments.

2.5.2 Dynamic Transport Simulation Code Including Plasma Rotation and Radial Electric Field

A new one-dimensional multi-fluid transport code named TASK/TX has been developed [2.5-2]. This code is able to describe dynamic behavior of tokamak plasmas, especially the time-evolution of the radial electric field and the plasma rotations. A set of flux-surface averaged equations is solved self-consistently in the cylindrical coordinates; Maxwell's equations, continuity equations, equations of motion, heat transport equations, momentum transfer equations for fast particles, and two-group neutral diffusion equations.

The finite element method with a piecewise linear interpolation function is employed. The Streamline Upwind Petrov–Galerkin method is also incorporated for numerically robust calculation. Despite solving the very nonlinear equations, the code shows a good convergence performance.

Modification of a density profile during neutral beam injection (NBI) is presented. We found the density peaking for the counter-NBI and the density broadening for the co-NBI. The balance between neoclassical and turbulent effects defines the status of the density profile. We have confirmed that the TASK/TX well reproduces the profiles observed in JFT-2M.

In the presence of ion orbit losses, the code predicts the generation of the intrinsic (spontaneous) rotation in the counter direction with the inward radial electric field. The non-ambipolar loss breaks quasi-neutrality and the plasma instantaneously generates the inward radial current near the periphery to compensate the ion loss current, inducing the more negative radial electric field and the torque toward the counter direction. Other conventional transport codes assuming the quasi-neutrality cannot follow these processes. It is the very special characteristic of the TASK/TX code that there is no need to impose an explicit quasi-neutrality condition.

References

2.5-1 Hayashi, N., *et al.*, *Contrib. Plasma Phys.* **48,** 196 (2008).

2.5-2 Honda, M., *et al., J. Comput.Phys.* **227,** 2808 (2008).

3. Atomic and Molecular Data

We have been producing, collecting and compiling cross-section data for atomic and molecular collisions and spectral data relevant to fusion research.

The electron capture and the electron loss cross-sections of singly ionized tungsten by collision with CH_4 and C_2H_6 have been measured at collision energies of 27.2 and 54.4 eV/amu. The state selective charge transfer cross-section data of B^{5+} and C^{6+} by collision with H* (n = 2) in the collision energy range between 62 eV/amu and 6.2 keV/amu have been calculated with a molecular-bases close-coupling method. The cross-section data for 42 processes of collisions of He, He^*, He^-, He^+, He^{2+} and $^3He^{2+}$ with H, H^-, H_2, He and He^+ have been complied. The recommended cross-section data are expressed with analytic functions to facilitate practical use of the data. The compiled data are in preparation for the Web at the URL http://www-jt60.naka.jaea.go.jp/english/JEAMDL/. The charge transfer data published in 2007 have been collected, and the database for the chemical sputtering yield data of graphite materials with hydrogen isotope collisions have been established.

III. Fusion Reactor Design Study

1. Progress in Compact DEMO Reactor Study

The design study of fusion DEMO reactor based on a slim CS (center solenoid coil) concept has been continued and still now be in progressing way. The slim CS concept leads to low aspect ratio plasma. The lower aspect ratio plasma is considered to have higher plasma performance (high elongation plasma and high beta) and then is considered to be preferable from viewpoint of economical aspect. The size of CS coil (radius of 75cm) is decided from the minimum magnetic flux requirement of 20 volt-second.

The SlimCS reactor produces a fusion output of 2.95GW with a major radius of 5.5m, aspect ratio (A) of 2.6, normalized beta (β_N) of 4.3 and maximum toroidal field of 16.4T.

Among the design progress issues, two issues concerning a plasma profile consistency and a tritium breeding are given in the followings.

Since plasma parameters are determined by a systems code based on a point model, the parameters should be checked for correctness using a one-dimensional (1-D) code. For this purpose, an ACCOME code [1-1] was used to investigate the consistency between the assumed plasma profiles and key parameters such as P_{fus}, β_N, n/n_{GW}, HHy2 and f_{BS}. In the 1-D analysis, we attempted to find a solution with q-profile other than strongly reversed shear (RS). This is because strong RS does not seem to be appropriate as the standard operation mode of SlimCS from the points of view of disruptivity and the controllability of q in the central region. Figure III.1-1 shows a solution for weakly RS [1-2]. Although the profile is not reasonably optimized because of a single ECRF beamline, the following information was obtained from the analysis:

1) Most of the design parameters by the point model are consistent with the 1-D calculation;
2) The location of NBCD is restricted to the peripheral region because of beam attenuation even for 1.5 MeV NB;
3) Use of ECRF as the main CD tool requires a high CD power due to its lower current drive efficiency than NBCD.

In addition, the calculation indicates that q-profile control in the central and peripheral regions is important to maintain the bootstrap fraction around the design value for various density and temperature profiles. For example, suppose that the BS current around an internal transport barrier is dominant. Then f_{BS} is strongly dependent on q-value around the ITB, i.e., the total current driven inside the ITB. For this sense, q-profile control can be key technology to maintaining f_{BS} at a design value in fusion plasma especially with high f_{BS}. In connection to this, the interplay between q-profile and pressure profile (including ITB structure) will be an essential issue governing the controllability on f_{BS}. A concern about the analysis is consistency between the obtained q-profile and the given density/temperature profiles. This is an open question to be resolved with further understanding on plasma transport. The result that even 1.5 MeV NB deposits in the peripheral region suggests the necessity to reconsider the role and beam energy of NBI. A possible idea for it is to use lower energy (e.g. ~0.5 MeV) NBI for driving plasma rotation as well as peripheral beam current.

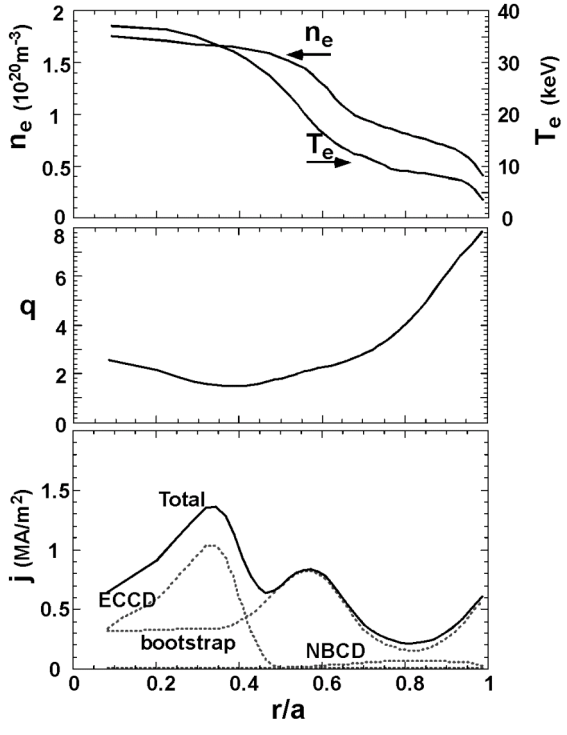

Fig.III.1-1 Example of weakly RS with consistency between pressure and current profiles

Another issue is a systematic analysis of tritium breeding ratio (TBR) based on a one-dimensional neutronics code THIDA with FENDL2.0 library. Findings of the analysis are:

- The required TBR is satisfied when ^{6}Li is enriched to about 70% for water-cooled solid pebble breeding blanket consisting of Li_2TiO_3 and Be;
- When ^{6}Li is enriched up to 40% or more, there is no difference about TBR between Li_2TiO_3 and Li_2ZrO_3;
- Sector-wide copper conducting shell with 1cm in thickness, which is placed in between replaceable and permanent blanket for vertical stability and high beta access of plasma, can be replaced by 7cm-thick reduced activated martensitic steel (F82H) with a slight decrease in TBR. This means that the torus configuration of SlimCS can be simplified by a modification of the structure of permanent blanket made of F82H.

When the actual tritium production is larger than expected, for example by 5%, surplus production of tritium amounts to about 25 g/day, which will be extracted from the fuel cycle system and stored in the on-site fuel storage. Since the surplus production of tritium reaches 9 kg for one-year operation, an in-situ TBR control method will be required to avoid excessive production. Borated-water is promising for the purpose in that water borated with 0.7 wt% of H_3BO_3 reduces the local TBR by 0.07 as shown in Fig.III.1-2, corresponding to a reduction of 0.05 in the net TBR. This indicates that borated-water injection into coolant is useful as in-situ TBR control.

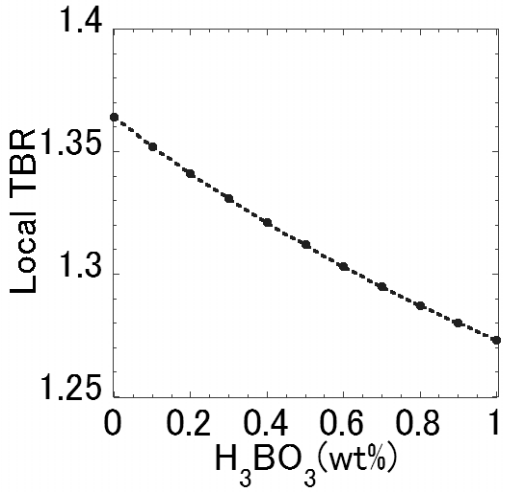

Fig.III.1-2 Local TBR as function of the concentration of H_3BO_3 in coolant.

References

1-1 Tani K., *et al., J. Comput. Phys.* **98**, 332(1990).

1-2 Tobita K., *et al*., *Nucl. Fusion* **47**, 892(2007).

2. Numerical Study on Beta Limit in Low Aspect Ratio Tokamak

The critical beta of low aspect ratio tokamak for toroidal mode number n=1 is analyzed by using MARG2D code developed in JAEA, which solves 2-dimensional Newcomb equation as an eigen-value problem [2-1].

The maximum stable beta value is considered to be mainly limited by RWM mode that is induced by ideal kink ballooning mode, and we analyze the ideal kink ballooning mode as a first step. As for the equilibria, typical up-down symmetric configuration of SlimCS (elongation : κ=2.0, triangularity : δ=0.36) is used, and the profiles of plasma current and pressure are obtained from the correlation function using the experimental profile data of JT-60U plasma with ITB (Internal Transport Barrier) [2-2], where the minimum values of safety factor are set to be greater than 3. Critical normalized beta 2.7 is obtained in the case of no ideal wall. To obtain stable β_N=4.3 SlimCS plasma, the conformal ideal wall must be placed at the position of 1.2 times plasma minor radius (Fig.III.2-1). Profile optimization is necessary to obtain higher critical normalized beta.

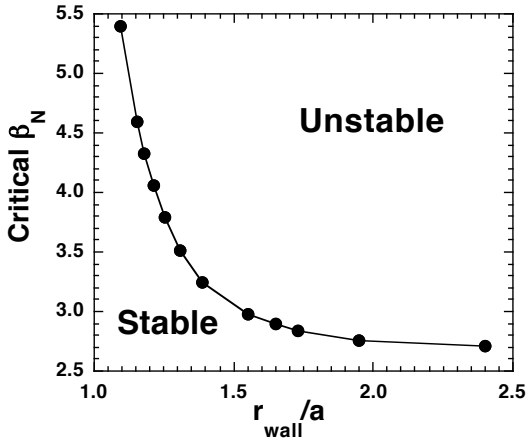

Fig.III.2-1 Critical β_N vs. minor radius of conformal ideal wall for n=1 mode.

References

2-1 Aiba N., *et al*., *Comp. Phys. Commun*. **175** 269 (2006).

2-2 Kurita G., Nagashima K., *et al* 1998 *15th Annual Meeting of Japan Society of Plasma Science and NuclearFusion Research.*

Appendix

A.1 Publication List (April 2007 – March 2008)

A.1.1 List of JAERI/JAEA Report

1) Chida, T., Ida, M., Nakamura, H., et al., "Thermo-Structural Analysis of Backwall in IFMIF Lithium Target, 2," JAEA-Technology 2007-048 (2007) (in Japanese).

2) Fujieda, H., Sugihara, M., Shimada, M., et al., "Studies on Representative Disruption Scenarios, Associated Electromagnetic and Heat Loads and Operation Window in ITER," JAEA-Research 2007-052 (2007).

3) Hayashi, K., Nakagawa, T., Onose, S., et al., "Investigation and Design of the Dismantling Process of Irradiation Capsules Containing Tritium, 1; Conceptual Investigation and Basic Design," JAEA-Technology 2008-010 (2008) (in Japanese).

4) Ichige, H., Honda, M., Sasaki, S., et al., "Development of Pellet Injector Using Screw Type Pellet Extruder; Improvement of Pellet Extruder for High Frequency and Long Duration, and its Test Results," JAEA-Technology 2007-037 (2007) (in Japanese).

5) Ida, M., Nakamura, H., Chida, T., et al., "Review of JAEA Activities on the IFMIF Liquid Lithium Target in FY2006," JAEA-Review 2008-008 (2008).

6) Ishii, K., Seki, M., Shinozaki, S., et al., "Power Injection Performance of the LH Antenna Tipped with Carbon Grills in JT-60U," JAEA-Technology 2007-036 (2007) (in Japanese).

7) Ishikawa, M., Kondoh, T., Hayakawa, A., et al., "Detail Design of Microfission Chamber for Fusion Power Diagnostic on ITER," JAEA-Technology 2007-062 (2007).

8) Iwai, Y., Hayashi, T., Kobayashi, K., et al., "Application of Tritium Behavior Simulation Code (TBEHAVIOR) to an Actual-Scale Tritium Handling Room," JAEA-Research 2007-070 (2007).

9) Kajita, S., Hatae, T., Katsunuma, A., et al., "Design Study of the Optical System in the Port Plug for Edge Thomson Scattering Diagnostics for ITER," JAEA-Technology 2007-064 (2008).

10) Kakudate, S., Shibanuma, K., "Singular Point Analysis During Rail Deployment into Vacuum Vessel for ITER Blanket Maintenance," JAEA-Technology 2007-032 (2007).

11) Oshima, K., Okano, F., Honda, A., et al., "Development of Protection System for Power Supply Facilities in JT-60U P-NBI for Long Pulse Operation," JAEA-Technology 2007-044 (2007) (in Japanese).

12) Sakata, S., Kiyono, K., Oshima, T., et al., "Progress of Data Processing System in JT-60 Utilizing the UNIX-Based Workstations," JAEA-Technology 2007-039 (2007) (in Japanese).

13) Seimiya, M., and JT-60 Operation Team, "The Archives of Operational Achievements in JT-60," JAEA-Technology 2007-049 (2007) (in Japanese).

14) Seki, Y., Tanigawa, H., Tsuru, D., et al., "Studies on Tritium Breeding Ratio for Solid Breeder Blanket Cooled by Pressurized Water Through Nuclear and Thermal Analyses," JAEA-Technology 2007-067 (2008) (in Japanese).

15) Shimada, K., Omori, Y., Okano, J., et al., "Initial Design Study of a DC Power Supply System for JT-60SA," JAEA-Technology 2008-031 (2008) (in Japanese).

16) Shimada, K., Terakado, T., Kurihara, K., "Design Study of an AC Power System for Additional Heating Facilities in JT-60SA," JAEA-Technology 2008-022 (2008) (in Japanese).

17) Sueoka, M., Kawamata, Y., Kurihara, K., et al., "Development of the Plasma Movie Database System in

JT-60," JAEA-Technology 2008-021 (2008) (in Japanese).

18) Suzuki, S., Seki, M., Shinozaki, S., et al., "Improvement of the Protection Devices for JT-60U LHRF Antenna System," JAEA-Technology 2007-055 (2007) (in Japanese).

19) Takato, N., Tobari, H., Inoue, T., et al., "Spatial Uniformity of Negative Ion Beam in Magnetically Filtered Hydrogen Negative Ion Source; Effect of the H^- Ion Production and Transport Processes on the H^- Ion Beam Intensity profile in the Cs-seeded negative ion source (Joint research)," JAEA-Research 2008-031 (2008) (in Japanese).

20) Terakado, M., Shimono, M., Sawahata, M., et al., "Development of the Power Modulation Technique in JT-60U ECH System," JAEA-Technology 2007-053 (2007) (in Japanese).

21) Totsuka, T., "Development of the Java-Based Man-Machine Interfacing System for Remote Experiments on JT-60," JAEA-Technology 2007-034 (2007) (in Japanese).

22) Yamaguchi, T., Kawano, Y., Kusama, Y., "Sensitivity Study of the ITER Poloidal Polarimeter," JAEA-Research 2007-078 (2008).

23) Yamauchi, M., Hori, J., Sato, S., et al., "ACT-XN; Revised Version of an Activation Calculation Code for Fusion Reactor Analysis; Supplement of the Function for the Sequential Reaction Activation by Charged Particles," JAEA-Data/Code 2007-016 (2007) (in Japanese).

24) Yokokura, K., Moriyama, S., Hasegawa, K., et al., "Development of Power Measuring Device of Transmission Type with Dielectric for High Power Millimeter Wave," JAEA-Technology 2007-045 (2007) (in Japanese).

A.1.2 List of Papers Published in Journals

1) Aiba, N., Tokuda, S., Fujita, T., et al., "Numerical Method for the Stability Analysis of Ideal MHD Modes with a Wide Range of Toroidal Mode Numbers in Tokamaks," Plasma Fusion Res., (Internet) **2**, 010 (2007).

2) Aiba, N., Tokuda, S., Takizuka, T., et al., "Effects of "Sharpness" of the Plasma Cross-Section on the MHD Stability of Tokamak Edge Plasmas," Nucl. Fusion, **47**, 297 (2007).

3) Araghy, H.P., Peterson, B.J., (Konoshima, S.), et al., "Spatial Variation of the Foil Parameters from in Situ Calibration of the JT-60U Imaging Bolometer Foil," Plasma Fusion Res., (Internet) **2**, S1116 (2007).

4) Asakura, N., ITPA SOL and Divertor Topical Group, "Understanding the SOL Flow in L-Mode Plasma on Divertor Tokamaks, and its Influence on the Plasma Transport," J. Nucl. Mater., **363-365**, 41 (2007).

5) Ashikawa, N., Kizu, K., (Miya, N.), et al., "Comparison of Boronized Wall in LHD and JT-60U," J. Nucl. Mater., **363-365**, 1352 (2007).

6) Batistoni, P., Angelone, M., (Ochiai, K.), et al., "Neutronics Experiment on a Helium Cooled pebble bed (HCPB) Breeder Blanket Mock-Up," Fusion Eng. Des., **82**, 2095 (2007).

7) Briguglio, S., Fogaccia, G., (Shinohara, K.), et al., "Particle Simulation of Bursting Alfvén Modes in JT-60U," Physics of Plasmas, **14**, 055904 (2007).

8) Callen, J.D., Anderson, J.K., (Fujita, T.), et al., "Experimental tests of paleoclassical transport," Nucl. Fusion, **47**, 1449 (2007).

9) Chankin, A.V., Coster, D.P., Asakura, N., et al., "Discrepancy Between Modelled and Measured Radial Electric Fields in the Scrape-Off Layer of Divertor Tokamaks; A Challenge for 2D Fluid Codes?," Nucl. Fusion, **47**, 479 (2007).

10) de Vries, P.C., Salmi, A., (Oyama, N.), et al., "Effect of Toroidal Field Ripple on Plasma Rotation in JET," Nucl. Fusion, **48**, 035007 (2008).

11) Donné, A.J.H., Costley, A.E., (Kawano, Y.), et al., "Progress in the ITER Physics Basis, 7; Diagnostics," Nucl. Fusion, **47**, S337 (2007).

12) Doyle, E.J., Houlberg, W.A., Kamada, Y., et al., "Progress in the ITER Physics Basis, 2; Plasma Confinement and Transport," Nucl. Fusion, **47**, S18 (2007).

13) Fasoli, A., Gormezano, C., (Shinohara, K.), et al., "Progress in the ITER Physics Basis, 5; Physics of Energetic Ions," Nucl. Fusion, **47**, S264 (2007).

14) Fujimoto, K., Nakano, T., Kubo, H., et al., "Modification of Tomography Technique for Two-Dimensional Spectroscopic Measurement in JT-60U Divertor Plasmas," Plasma Fusion Res., (Internet) **2**, S1121 (2007).

15) Fujino, I., Hatayama, A., (Inoue, T.), et al., "Analysis of Electron Energy Distribution of an Arc-Discharge H^- Ion Source with Monte Carlo Simulation," Rev. Sci. Instrum., **79**, 02A510 (2008).

16) Fujisawa, A., Ido, T., Hoshino, K., et al., "Experimental Progress on Zonal Flow Physics in Toroidal Plasmas," Nucl. Fusion, **47**, S718 (2007).

17) Fujita, T., Tamai, H., Matsukawa, M., et al., "Design Optimization for Plasma Performance and Assessment of Operation Regimes in JT-60SA," Nucl. Fusion, **47**, 1512 (2007).

18) Gormezano, C., Sips, A.C.C., (Ide, S.), et al., "Progress in the ITER Physics Basis, 6; Steady State Operation," Nucl. Fusion, **47**, S285 (2007).

19) Gribov, Y., Humphreys, D.A., (Ozeki, T.), et al., "Progress in the ITER Physics Basis, 8; Plasma Operation

and Control," Nucl. Fusion, **47**, S385 (2007).

20) Hamada, K., Nakajima, H., Kawano, K., et al., "Demonstration of Full Scale JJ1 and 316LN Fabrication for ITER TF Coil Structure," Fusion Eng. Des., **82**, 1481 (2007).

21) Hamamatsu, K., Takizuka, T., Hayashi, N., et al., "Numerical Simulation of Electron Cyclotron Current Drive in Magnetic Islands of Neo-Classical Tearing Mode," Plasma Phys. Control. Fusion, **49**, 1955 (2007).

22) Hanada, M., Ikeda, Y., Kamada, M., et al., "Correlation Between Voltage Holding Capability and Light Emission in a 500 keV Electrostatic Accelerator Utilized for Fusion Application," IEEE Trans. Dielectr. Electr. Insulat., **143**, 572 (2007).

23) Hanada, M., Inoue, T., Kashiwagi, M., et al., "R&D Progress at JAEA Towards Production of High Power and Large-Area Negative Ion Beams for ITER," Nucl. Fusion, **47**, 1142 (2007).

24) Hatae, T., Howard, J., Hirano, Y., et al., "Development of polarization interferometer based on Fourier transform spectroscopy for Thomson scattering diagnostics," Plasma Fusion Res., (Internet) **2**, S1026 (2007).

25) Hayashi, N., Takizuka, T., Aiba, N., et al., "Integrated ELM Simulation with Edge MHD Stability and Transport of SOL-Divertor Plasmas," Contrib. Plasma Phys., **48**, 196 (2008).

26) Hayashi, N., Takizuka, T., Hosokawa, M., et al., "Modeling of Dynamic Response of SOL-Divertor Plasmas to an ELM Crash," J. Nucl. Mater., **363-365**, 1044 (2007).

27) Hayashi, N., Takizuka, T., Ozeki, T., et al., "Integrated Simulation of ELM Energy Loss Determined by Pedestal MHD and SOL Transport," Nucl. Fusion, **47**, 682 (2007).

28) Hayashi, T., Kasada, R., Tobita, K., et al., "Impact of N-Isotope Composition Control of Ferritic Steel on Classification of Radioactive Materials from Fusion Reactor," Fusion Eng. Des., **82**, 2850 (2007).

29) Hayashi, T., Sakurai, S., Masaki, K., et al., "Conceptual Design of Divertor Cassette Handling by Remote Handling System of JT-60SA," Journal of Power and Energy Systems (Internet), **2**, 522 (2008).

30) Hayashi, T., Sugiyama, K., Krieger, K., et al., "Deuterium Depth Profiling in JT-60U Tiles Using the D(^{3}He, p)^{4}He Resonant Nuclear Reaction," J. Nucl. Mater., **363-365**, 904 (2007).

31) Hayashi, T., Isobe, K., Kobayashi, K., et al., "Recent Activities on Tritium Technologies for ITER and Fusion Reactors at JAEA," Fusion Sci. Tech., **52**, 651 (2007).

32) Hayashi, T., Nakamura, H., Isobe, K., et al., "Tritium Behavior on the Water-Metal Boundary for the Permeation Into Cooling Water Through Metal Piping," Fusion Sci. Tech., **52**, 687 (2007).

33) Hayashi, T., Suzuki, T., Shu, W., et al., "Isotope Effect of Hydrogen Rapidly Supplied from the Metal Storage Bed," Fusion Sci. Tech., **52**, 706 (2007).

34) Hender, T.C., Wesley, J.C., (Isayama, A.), et al., "Progress in the ITER Physics Basis, 3; MHD Stability, Operational Limits and Disruptions," Nucl. Fusion, **47**, S128 (2007).

35) Hirohata, Y., Tanabe, T., (Miya, N.), et al., "Hydrogen Isotopes Retention in JT-60U," J. Nucl. Mater., **363-365**, 854 (2007).

36) Hiroki, S., Tanzawa, S., Arai, T., et al., "Development of Water Leak Detection Method in Fusion Reactors Using Water-Soluble Gas," Fusion Eng. Des., **83**, 72 (2008).

37) Hirose, T., Tanigawa, H., Enoeda, M., et al., "Effects of Tube Drawing on Structural Material for ITER Test Blanket Module," Fusion Sci. Tech., **52**, 839 (2007).

38) Honda, M., Fukuyama, A., "Dynamic Transport Simulation Code Including Plasma Rotation and Radial

Electric Field," J. Comput. Phys., **227**, 2808 (2008).

39) Hoshino, K., Suzuki, T., Isayama, A., et al., "Electron Cyclotron Heating Applied to the JT-60U Tokamak," Fusion Sci. Tech., **53**, 114 (2008).

40) Hoshino, T., Yasumoto, M., Tsuchiya, K., et al., "Non-Stoichiometory and Vaporization Characteristic of $Li_{2.1}TiO_{3.05}$ in Hydrogen Atmosphere," Fusion Eng. Des., **82**, 2269 (2007).

41) Hosogane, N., JT-60SA Design Team and Japan-Europe Satellite Tokamak Working Group, "Superconducting Tokamak JT-60SA Project for ITER and DEMO Researches," Fusion Sci. Tech., **52**, 375 (2007).

42) Ichimura, M., Higaki, H., (Moriyama, S.), et al., "Observation of Spontaneously Excited Waves in the Ion Cyclotron Frequency Range on JT-60U," Nucl. Fusion, **48**, 035012 (2008).

43) Ida, M., Nakamura, H., Sugimoto, M., "Analytical Estimation of Accessibility to the Activated Lithium Loop in IFMIF," J. Nucl. Mater., **367-370**, 1557 (2007).

44) Ida, M., Nakamura, H., Sugimoto, M., "Estimation and Control of Beryllium-7 Behavior in Liquid Lithium Loop of IFMIF," Fusion Eng. Des., **82**, 2490 (2007).

45) Ide, S., Takenaga, H., Isayama, A., et al., "Studies on Impact of Electron Cyclotron Wave Injection on the Internal Transport Barriers in JT-60U Weak Shear Plasmas," Nucl. Fusion, **47**, 1499 (2007).

46) Idomura, Y., Ida, M., Tokuda, S., "Conservative Gyrokinetic Vlasov Simulation," Commun. Nonlinear. Sci. Numer. Simulat., **13**, 227 (2008).

47) Idomura, Y., Ida, M., Tokuda, S., et al., "New conservative gyrokinetic full-*f* Vlasov code and its comparison to gyrokinetic δ*f* particle-in-cell code," J. Comput. Phys., **226**, 244 (2007).

48) Ikeda, Y., Akino, N., Ebisawa, N., et al., "Technical design of NBI system for JT-60SA," Fusion Eng. Des., **82**, 791 (2007).

49) Inoue, T., Hanada, M., Kashiwagi, M., et al., "Development of Beam Source and Bushing for ITER NB System," Fusion Eng. Des., **82**, 813 (2007).

50) Inoue, T., Tobari, H., Takado, N., et al., "Negative Ion Production in Cesium Seeded High Electron Temperature Plasmas," Rev. Sci. Instrum., **79**, 02C112 (2008).

51) Ioki, K., Elio, F., Barabash, V., et al., "Six-Party Qualification Program of FW Fabrication Methods for ITER Blanket Module Procurement," Fusion Eng. Des., **82**, 1774 (2007).

52) Isayama, A., Oyama, N., Urano, H., et al., "Stabilization of Neoclassical Tearing Modes by Electron Cyclotron Current Drive in JT-60U," Nucl. Fusion, **47**, 773 (2007).

53) Ishii, Y., Azumi, M., Smolyakov, A.I., "Nonliear Evolution and Deformation of Driven Magnetic Islands in Rotating Plasmas," Nucl. Fusion, **47**, 1024 (2007).

54) Ishikawa, M., Nishitani, T., Kusama, Y., et al., "Neutron Emission Profile Measurement and Fast Charge Exchange Neutral Particle Flux Measurement for Transport Analysis of Energetic Ions in JT-60U," Plasma Fusion Res., (Internet) **2**, 019 (2007).

55) Ishikawa, M., Takechi, M., Shinohara, K., et al., "Confinement Degradation and Transport of Energetic Ions due to Alfvén Eigenmodes in JT-60U Weak Shear Plasmas," Nucl. Fusion, **47**, 849 (2007).

56) Ito, T., Hayashi, T., Isobe, K., et al., "Self-Decomposition Behavior of High Concentration Tritiated Water," Fusion Sci. Tech., **52**, 701 (2007).

57) Jolliet, S., Bottino, A., (Idomura, Y.), et al., "A Global Collisionless PIC Code in Magnetic Coordinates,"

Comput. Phys. Commun., **177**, 409 (2007).

58) Kajita, S., Ono, N., Takamura, S., et al., "Plasma-Assisted Laser Ablation of Tungsten; Reduction in Ablation Power Threshold due to Bursting of Holes/Bubbles," Applied Physics Letters, **91**, 261501 (2007).

59) Kamiya, K., Asakura, N., Boedo, J.A., et al., "Edge Localized Modes; Recent Experimental Findings and Related Issues," Plasma Phys. Control. Fusion, **49**, s43 (2007).

60) Kanemura, T., Kondo, H., (Ida, M.), et al., "Investigation of Free-Surface Fluctuations of Liquid Lithium Flow for IFMIF Lithium Target by Using an Electro-Contact Probe," Fusion Eng. Des., **82**, 2550 (2007).

61) Kawashima, H., Shimizu, K., Takizuka, T., "Development of Integrated SOL/Divertor Code and Simulation Study of the JT-60U/JT-60SA Tokamaks," Plasma Phys. Control. Fusion, **49**, s77 (2007).

62) Kawashima, H., Shimizu, K., Takizuka, T., et al., "Simulation of Divertor Pumping in JT-60U with SOLDOR/NEUT2D Code," J. Nucl. Mater., **363-365**, 786 (2007).

63) Kizu, K., Tsuchiya, K., Ando, T., et al., "Conceptual Design of Magnet System for JT-60 Super Advanced (JT-60SA)," IEEE Trans. Appl. Superconduct., **17**, 1348 (2007).

64) Kizu, K., Tsuchiya, K., Shimada, K., et al., "Evaluation of Bending Strain Dependence of Critical Current of Nb_3Al Conductor for Coils with React-And-Wind Method," Fusion Eng. Des., **82**, 1493 (2007).

65) Kobayashi, K., Hayashi, T., Nakamura, H., et al., "Study for the Behavior of Tritiated Water Vapor on Organic Materials," Fusion Sci. Tech., **52**, 696 (2007).

66) Kobayashi, K., Isobe, K., Iwai, Y., et al., "Studies on the Behavior of Tritium in Components and Structure Materials of Tritium Confinement and Detritiation Systems of ITER," Nucl. Fusion, **47**, 1645 (2007).

67) Kobayashi, K., Miura, H., Hayashi, T., et al., "Oxidation Performance Test of Detritiation System Under Existence of SF_6," Fusion Sci. Tech., **52**, 711 (2007).

68) Kobayashi, S., and JT-60 Team, "Development of Real-Time Measurement System of Charge Exchange Recombination Spectroscopy and its Application to Feedback Control of Ion Temperature Gradient in JT-60U," Plasma Fusion Res., (Internet) **2**, S1049 (2007).

69) Kobayashi, T., Moriyama, S., Seki, M., et al., "Achievement of 1.5 MW, 1 s Oscillation by the JT-60U Gyrotron," Plasma Fusion Res., (Internet) **3**, 014 (2008).

70) Koizumi, N., Isono, T., Hamada, K., et al., "Development of Large Current Superconductors Using High Performance Nb_3Sn Strand for ITER," Physica C, **463-465**, 1319 (2007).

71) Kojima, A., Kamiya, K., Iguchi, H., et al., "Numerical simulation of a high-brightness lithium ion gun for a Zeeman polarimetry on JT-60U," Plasma Fusion Res., (Internet) **2**, S1104 (2007).

72) Kondo, H., Kanemura, T., (Ida, M.), et al., "Measurement of Free Surface of Liquid Metal Lithium Jet for IFMIF Target," Fusion Eng. Des., **82**, 2483 (2007).

73) Kondo, K., Murata, I., Ochiai, K., et al., "Measurement and Analysis of Neutron-Induced Alpha Particle Emission Double-Differential Cross Section of Carbon at 14.2 MeV," J. Nucl. Sci. Technol., **45**, 103 (2008).

74) Kondo, K., Murata, I., Ochiai, K., et al., "Verification of Nuclear Data for DT Neutron Induced Charged-Particle Emission Reaction of Light Nuclei," Fusion Eng. Des., **82**, 2786 (2007).

75) Kubo, H., Sasaki, A., Moribayashi, K., et al., "Study of Highly Ionized Xe Spectra with 3s-3p and 3p-3d Transitions in JT-60U Reversed Shear Plasmas," J. Nucl. Mater., **363-365**, 1441 (2007).

76) Kubota, N., Kondo, K., Ochiai, K., et al., "Neutron Elastic Recoil Detection for Hydrogen Isotope Analysis in Fusion Materials," J. Nucl. Mater., **367-370**, 1596 (2007).

77) Li, Z., Tanaka, T., (Sato, S.), et al., "Spectral Effects of Activation for Liquid Blanket Relevant Materials Induced by D-T Neutron Irradiation," Fusion Sci. Tech., **52**, 817 (2007).

78) Liu, Y., Tamura, N., (Konoshima, S.), et al., "Application of Tomographic Imaging to Multi-Pixel Bolometric Measurements," Plasma Fusion Res., (Internet) **2**, S1124 (2007).

79) Loarte, A., Lipschultz, B., (Asakura, N.), et al., "Progress in the ITER Physics Basis, 4; Power and Particle Control," Nucl. Fusion, **47**, S203 (2007).

80) Maggi, C.F., Groebner, R.J., Oyama, N., et al., "Characteristics of the H-mode Pedestal in Improved Confinement Scenarios in ASDEX Upgrade, DIII-D, JET and JT-60U," Nucl. Fusion, **47**, 535 (2007).

81) Masaki, K., Tanabe, T., Hirohata, Y., et al., "Hydrogen Retention and Carbon Deposition in Plasma Facing Components and the Shadowed Area of JT-60U," Nucl. Fusion, **47**, 1577 (2007).

82) Matsumoto, T., Li, J., Kishimoto, Y., "Characteristics of ETG-Driven Turbulence Dominated by Zonal Flows," Nucl. Fusion, **47**, 880 (2007).

83) Matsushita, D., Takado, N., (Inoue, T.), et al., "Numerical Analysis of H^- Ion Transport Processes in Cs-Seeded Negative Ion Sources," Rev. Sci. Instrum., **79**, 02A527 (2008).

84) Miki, K., Kishimoto, Y., Miyato, N., et al., "Intermittent Transport Associated with the Geodesic Acoustic Mode Near the Critical Gradient Regime," Physical Review Letters, **99**, 145003 (2007).

85) Mishima, Y., Yoshida, N., (Tsuchiya, K.), et al., "Recent Results on Beryllium and Beryllides in Japan," J. Nucl. Mater., **367-370**, 1382 (2007).

86) Miyato, N., Kishimoto, Y., Li, J.Q., "Turbulence Suppression in the Neighbourhood of a Minimum-q Surface due to Zonal Flow Modification in Reversed Shear Tokamaks," Nucl. Fusion, **47**, 929 (2007).

87) Morimoto, M., Ioki, K., Terasawa, A., et al., "Design Progress of the ITER In-Wall Shielding," Fusion Sci. Tech., **52**, 834 (2007).

88) Morioka, A., Sakurai, S., Okuno, K., et al., "Development of 300°C Heat Resistant Boron-Loaded Resin for Neutron Shielding," J. Nucl. Mater., **367-370**, 1085 (2007).

89) Moriyama, S., Seki, M., Fujii, T., "Design Study of a New Antenna System for Steering Microwave Beam in Electron Cyclotron Heating/Current Drive System," Fusion Eng. Des., **82**, 785 (2007).

90) Motojima, O., Yamada, H., (Isayama, A.), et al., "Extended Steady-State and High-Beta Regimes of Net-Current Free Heliotron Plasmas in the Large Helical Device," Nucl. Fusion, **47**, S668 (2007).

91) Murakami, H., Ishiyama, A., (Koizumi, N.), et al., "Numerical Simulation of Critical Current and N-Value in Nb_3Sn Strand Subjected to Bending Strain," IEEE Trans. Appl. Superconduct., **17**, 1394 (2007).

92) Nagashima, Y., Ito, K., (Hoshino, K.), et al., "In search of Zonal Flows by Using Direct Density Fluctuation Measurements," Plasma Phys. Control. Fusion, **49**, 1611 (2007).

93) Nakajima, H., Hamada, K., Okuno, K., et al., "Development of Optimum Manufacturing Technologies of Radial Plates for the ITER Toroidal Field Coils," Fusion Eng. Des., **82**, 1473 (2007).

94) Nakamichi, M., Kulsartov, T.V., Hayashi, K., et al., "In-pile Tritium Permeation Through F82H Steel with and Without a Ceramic Coating of Cr_2O_3-SiO_2 Including $CrPO_4$," Fusion Eng. Des., **82**, 2246 (2007).

95) Nakamura, H., Kobayashi, K., Yamanishi, T., et al., "Tritium Release Behavior from Steels Irradiated by High Energy Protons," Fusion Sci. Tech., **52**, 1012 (2007).

96) Nakamura, H., Ida, M., Chida, T., et al., "Design of a Lip Seal-Replaceable Backwall for IFMIF Liquid

Lithium Target," Fusion Eng. Des., **82**, 2671 (2007).

97) Nakamura, T., Sakagami, H., (Koga, J.K.), et al., "High Energy Electron Generation by Laser-Cone Interaction," Plasma Fusion Res., (Internet) **2**, 018 (2007).

98) Nakamura, T., Sakagami, H., (Koga, J.K.), et al., "Optimization of Cone Target Geometry for Fast Ignition," Physics of Plasmas, **14**, 103105 (2007).

99) Nakano, T., and JT-60 Team, "Particle Balance Under Global Wall Saturation in Long-Pulse Discharges of JT-60U," J. Nucl. Mater., **363-365**, 1315 (2007).

100) Nakano, T., Kubo, H., Asakura, N., et al., "Volume Recombination of C^{4+} in Detached Divertor Plasmas of JT-60U," Nucl. Fusion, **47**, 1458 (2007).

101) Nishimura, A., Nishijima, S., (Nishitani, T.), et al., "Change in Properties of Superconducting Magnet Materials by Fusion Neutron Irradiation," Fusion Eng. Des., **82**, 1555 (2007).

102) Nishitani, T., Enoeda, M., Akiba, M., et al., "Recent Progress in Solid Breeder Blanket Development at JAEA," Fusion Sci. Tech., **52**, 971 (2007).

103) Nishitani, T., Sato, S., Ochiai, K., et al., "Progress in Neutronics Studies for the Water Cooled Pebble Bed Blanket," Fusion Sci. Tech., **52**, 791 (2007).

104) Nishitani, T., Yamauchi, M., Izumi, M., et al., "Engineering Design of the ITER Invessel Neutron Monitor Using Micro-Fission Chambers," Fusion Eng. Des., **82**, 1192 (2007).

105) Nunoya, Y., Isono, T., Koizumi, N., et al., "Development of Strain-Applying Apparatus for Evaluation of ITER Nb_3Sn Strand," IEEE Trans. Appl. Superconduct., **17**, 2588 (2007).

106) Ochiai, K., Sato, S., Wada, M., et al., "Thin Slit Streaming Experiment for ITER by Using D-T Neutron Source," Fusion Eng. Des., **82**, 2794 (2007).

107) Ogawa, H., Sugie, T., Kasai, S., et al., "Development of Impurity Influx Monitor (Divertor) for ITER Plasma," Fusion Res., (Internet) **2**, S1054 (2007).

108) Ogawa, M., Iio, S., (Inoue, T.), et al., "Magnetic Fusion Energy Studies in Japan," Nucl. Instrum. Methods. Phys. Res., A, **577**, 30 (2007).

109) Ohira, S., Hayashi, T., Shu, W., et al., "Radiochemical Characteristics of Tritium to be Considered in Fusion Reactor Facility Design," J. Radioanal. Nucl. Chem., **272**, 575 (2007).

110) Oka, K., Onuki, S., Yamashita, S., et al., "Structure of Nano-Size Oxides in ODS Steels and its Stability Under Electron Irradiation," Materials Transactions, **48**, 2563 (2007).

111) Okuno, K., Nakajima, H., Sugimoto, M., et al., Technology Development for the Construction of the ITER Superconducting Magnet System," Nucl. Fusion, **47**, 456 (2007).

112) Onozuka, M., Shimizu, K., (Nakajima, H.), et al., "Basic Analysis of Weldability and Machinability of Structural Materials for ITER Toroidal Field Coils," Fusion Eng. Des., **82**, 1431 (2007).

113) Oshima, T., Kiyono, K., Sakata, S., et al., "Improvement of Data Processing System for Advanced Diagnostics in JT-60U," Fusion Eng. Des., **82**, 1210 (2007).

114) Oya, Y., Hirohata, Y., (Masaki, K.), et al., "Hydrogen Isotope Retentions and Erosion/Deposition Profiles in the First Wall of JT-60U," Fusion Sci. Tech., **52**, 554 (2007).

115) Oyama, N., and JT-60 Team, "Improved Performance in Long-Pulse ELMy H-mode Plasmas with Internal Transport Barrier in JT-60U," Nucl. Fusion, **47**, 689 (2007).

116) Ozeki, T., and JT-60 Team, "High-Beta Steady-State Research with Integrated Modeling in the JT-60 Upgrade," Physics of Plasmas, **14**, 056114 (2007).

117) Peterson, B.J., LHD Team and JT-60U Team, "Research and Development of Imaging Bolometers," Plasma Fusion Res., (Internet) **2**, S1018 (2007).

118) Peterson, B.J., and JT-60 Team, "Observation of Divertor and Core Radiation in JT-60U by Means of Bolometric Imaging," J. Nucl. Mater., **363-365**, 412 (2007).

119) Prater, R., La Haye, R.J., (Isayama, A.), et al., "Stabilization and Prevention of the 2/1 Neoclassical Tearing Mode for Improved Performance in DIII-D," Nucl. Fusion, **47**, 371 (2007).

120) Rewoldt, G., Lin, Z., Idomura, Y., "Linear Comparison of Gyrokinetic Codes with Trapped Electrons," Comput. Phys. Commun., **177**, 775 (2007).

121) Saibene, G., Oyama, N., Lönnroth, J., et al., "The H-Mode Pedestal, ELMs and TF Ripple Effects in JT-60U/JET Dimensionless Identity Experiments," Nucl. Fusion, **47**, 969 (2007).

122) Sakamoto, K., "Progress of High-Power-Gyrotron Development for Fusion Research," Fusion Sci. Tech., **52**, 145 (2007).

123) Sakamoto, K., Kasugai, A., Takahashi, K., et al., "Achievement of Robust High-Efficiency 1 MW Oscillation in the Hard-Self-Excitation Region by a 170 GHz Continuous-Wave Gyrotron," Nature Physics, **3**, 411 (2007).

124) Sakamoto, Y., and JT-60 Team, "Controllability of Large Bootstrap Current Fraction Plasmas in JT-60U," Nucl. Fusion, **47**, 1506 (2007).

125) Sakamoto, Y., and JT-60 Team, "Controllability of Large Bootstrap Current Fraction Plasmas in JT-60U," Nucl. Fusion, **47**, 1506 (2007).

126) Sasao, M., Nishitani, T., Krasilnikov, A., et al., "Fusion Product Diagnostics," Fusion Sci. Tech., **53**, 604 (2008).

127) Sato, K., Omori, J., Ebisawa, K., et al., "Development of ITER Diagnostic Upper Port Plug," Plasma Fusion Res., (Internet) **2**, S1088 (2007).

128) Sato, M., Isayama, A., "Evaluation of Extended Trubnikov Emissivity to the Oblique Propagation and Application to Electron Temperature Measurement in a Reactor-Grade Tokamak," Fusion Sci. Tech., **52**, 169 (2007).

129) Sato, M., Isayama, A., "Effects of Relativistic and Absorption on ECE Spectra in High Temperature Tokamak Plasma," Plasma Fusion Res., (Internet) **2**, S1029 (2007).

130) Sato, S., Ochiai, K., Verzilov, Y., et al., "Measurement of Tritium Production Rate in Water Cooled Pebble Bed Multi-Layered Blanket Mockup by DT Neutron Irradiation Experiment," Nucl. Fusion, **47**, 517 (2007).

131) Sato, S., Verzilov, Y., Ochiai, K., et al., "Neutronics Experimental Study on Tritium Production in Solid Breeder Blanket Mockup with Neutron Reflector," J. Nucl. Sci. Technol., **44**, 657 (2007).

132) Seki, M., "ITER Activities and Fusion Technology," Nucl. Fusion, **47**, S489 (2007).

133) Shibama, Y., Arai, T., Miyo, Y., et al., "Structural Design of Ferritic Steel Tiles for Ripple Reduction of Toroidal Magnetic Field in JT-60U," Fusion Eng. Des., **82**, 2462 (2007).

134) Shimada, K., Ito, J., Matsukawa, M., "A Control Method of Matrix Converter for Plasma Control Coil power Supply," Fusion Eng. Des., **82**, 1513 (2007).

135) Shimada, M., Campbell, D.J., Mukhovatov, V., et al., "Progress in the ITER Physics Basis, 1; Overview and

Summary," Nucl. Fusion, **47**, S1 (2007).

136) Shimizu, K., Takizuka, T., Kawashima, H., "A New Fast Velocity-Diffusion Modelling for Impurity Transport in Integrated Edge Plasma Simulation," J. Nucl. Mater., **363-365**, 426 (2007).

137) Shimizu, K., Takizuka, T., Kawashima, H., "Extension of IMPMC Code Toward Time Evolution Simulation," Contrib. Plasma Phys., **48**, 270 (2008).

138) Shimomura, K., Takenaga, H., Tsutsui, H., et al., "Burn Control Simulation Experiments in JT-60U," Fusion Eng. Des., **82**, 953 (2007).

139) Shinohara, K., Isobe, M., Darrow, D.S., et al., "Escaping Ion Measurement with High Time Resolution During Bursting Modes Induced by Neutral Beam Injection on CHS," Plasma Fusion Res., (Internet) **2**, 042 (2007).

140) Shinohara, K., and JT-60 Team, "Ferritic Insertion for Reduction of Toroidal Magnetic Field Ripple on JT-60U," Nucl. Fusion, **47**, 997 (2007).

141) Sueoka, M., Kawamata, Y., Kurihara, K., et al., "The Plasma Movie Database System for JT-60," Fusion Eng. Des., **82**, 1008 (2007).

142) Sugiyama, K., Hayashi, T., (Miya, N.), et al, "Ion Beam Analysis of H and D Retention in the Near Surface Layers of JT-60U Plasma Facing Wall Tiles," J. Nucl. Mater., **363-365**, 949 (2007).

143) Sukegawa, A., Sakurai, S., Masaki, K., et al., "Safety Design of Radiation Shielding for JT-60SA," Fusion Eng. Des., **82**, 2799 (2007).

144) Takado, N., Matsushita, D., (Inoue, T.), et al., "Effect of Energy Relaxation of H^0 Atoms at the Wall on the Production Profile of H^- Ions in Large Negative Ion Sources," Rev. Sci. Instrum., **79**, 02A503 (2008).

145) Takahashi, K., Kobayashi, N., Omori, J., et al., "Progress on Design and Development of ITER Equatorial Launcher; Analytical Investigation and R&D of the Launcher Components for the Design Improvement," Fusion Sci. Tech., **52**, 266 (2007).

146) Takahashi, Y., Yoshida, K., Nabara, Y., et al., "Stability and Quench Analysis of Toroidal Field Coils for ITER," IEEE Trans. Appl. Superconduct., **17**, 2426 (2007).

147) Takeda, N., Kakudate, S., Nakahira, M., et al., "Performance Test of Diamond-Like Carbon Films for Lubricating ITER Blanket Maintenance Equipment Under GPa-Level High Contact Stress," Plasma Fusion Res., (Internet) **2**, 052 (2007).

148) Takenaga, H., and JT-60 Team, "Overview of JT-60U Results for the Development of a Steady-State Advanced Tokamak Scenario," Nucl. Fusion, **47**, S563 (2007).

149) Takenaga, H., Kubo, H., Sueoka, M., et al., "Response of Fusion Gain to Density in Burning Plasma Simulation on JT-60U," Nucl. Fusion, **48**, 035011 (2008).

150) Takenaga, H., Oyama, N., Isayama, A., et al., "Observation on Decoupling of Electron Heat Transport and Long-Spatial-Scale Density Fluctuations in a JT-60U Reversed Shear Plasma," Plasma Phys. Control. Fusion, **49**, 525 (2007).

151) Takizuka, T., Oyama, N., Hosokawa, M., "Effect of Radial Transport Loss on the Asymmetry of ELM Heat Flux," Contrib. Plasma Phys., **48**, 207 (2008).

152) Tamai, H., Fujita, T., Kikuchi, M., et al., "Prospective Performances in JT-60SA Towards the ITER and DEMO Relevant Plasmas," Fusion Eng. Des., **82**, 541 (2007).

153) To, K., Shikama, T., (Yamauchi, M.), et al., "Search for Luminescent Materials Under 14 MeV Neutron Irradiation," J. Nucl. Mater., **367-370**, 1128 (2007).

154) Tobari, H., Seki, T., Takado, N., et al., "Negative Ion Production in High Electron Temperature Plasmas," Plasma Fusion Res., (Internet) **2**, 022 (2007).

155) Tobita, K., Nishio, S., Sato, M., et al., "SlimCS; Compact Low Aspect Ratio DEMO Reactor with Reduced-Size Central Solenoid," Nucl. Fusion, **47**, 892 (2007).

156) Tomita, Y., Smirnov, R.D., Takizuka, T., et al., "Effect of Oblieque Magnetic Field on Release Conditions of Dust Particle from Plasma-Facing Wall," Contrib. Plasma Phys., **48**, 285 (2008).

157) Tomita, Y., Smirnov, R., (Takizuka, T.), et al., "Effect of Truncation of Electron Velocity Distribution on Release of Dust Particle from Plasma-Facing Wall," J. Nucl. Mater., **363-365**, 264 (2007).

158) Tsuchiya, K., Kizu, K., Ando, T., et al., "Design of the Superconducting Coil System in JT-60SA," Fusion Eng. Des., **82**, 1519 (2007).

159) Tsuchiya, K., Hoshino, T., Kawamura, H., et al., "Development of Advanced Tritium Breeders and Neutron Multipliers for DEMO Solid Breeder Blankets," Nucl. Fusion, **47**, 1300 (2007).

160) Tsuchiya, K., Kawamura, H., Ishida, T., "Compatibility Between Be-Ti Alloys and F82H Steel," J. Nucl. Mater., **367-370**, 1018 (2007).

161) Tsuchiya, K., Kawamura, H., Ishida, T., "Effect of Ti Content on Compatibility Between Be-Ti and SS316LN," Nuclear Technology **159**, 228 (2007).

162) Tsuchiya, K., Shimizu, M., Kawamura, H., et al., "Effect of Re-Irradiation by Neutrons on Mechanical Properties of Un-Irradiated/Irradiated SS316LN Weldments," J. Nucl. Mater., **373**, 212 (2008).

163) Tsuru, D., Enoeda, M., Akiba, M., "Pressurizing Behavior on Ingress of Coolant Into Pebble Bed of Blanket of Fusion DEMO Reactor," Fusion Eng. Des., **82**, 2274 (2007).

164) Ueda, Y., Fukumoto, M., (Miya, N.), et al., "Surface Studies of Tungsten Erosion and Deposition in JT-60U," J. Nucl. Mater., **363-365**, 66 (2007).

165) Urano, H., and JT-60 Team, "H-mode Pedestal Structure in the Variation of Toroidal Rotation and Toroidal Field Ripple in JT-60U," Nucl. Fusion, **47**, 706 (2007).

166) Wakai, E., Ando, M., Sawai, T., et al., "Effect of Helium and Hydrogen Production on Irradiation Hardening of F82H Steel Irradiated by Ion Beams," Materials Transactions **48**, 1427 (2007).

167) Wakai, E., Ando, M., Sawai, T., et al., "Effect of Heat Treatments on Tensile Properties of F82H Steel Irradiated by Neutrons," J. Nucl. Mater., **367-370**, 74 (2007).

168) Watanabe, H., Nakamura, N., (Nakano, T.), et al., "X-ray Spectra from Neon-Like Tungsten Ions in the Interaction with Electrons," Plasma Fusion Res., (Internet) **2**, 027 (2007).

169) Yamada, H., Takenaga, H., Suzuki, T., et al., "Density Limit in Discharges with High Internal Inductance on JT-60U," Nucl. Fusion, **47**, 1418 (2007).

170) Yamaguchi, T., Kawano, Y., Kusama, Y., "Sensitivity Study for the Optimization of the Viewing Chord Arrangement of the ITER Poloidal Polarimeter," Plasma Fusion Res., (Internet) **2**, S1112 (2007).

171) Yamamoto, I., Nishitani, T., Sagara, A., "Overview of Recent Japanese Activities and Plans in Fusion Technology," Fusion Sci. Tech., **52**, 347 (2007).

172) Yamamoto, Y., Yamanishi, T., (Isobe, K.), et al., "Fundamental Study on Purity Control of the Liquid Metal Blanket Using Solid Electrolyte Cell," Fusion Sci. Tech., **52**, 692 (2007).

173) Yamauchi, M., Nishitani, T., Nishio, S., et al., "Activation Analysis for Sequential Reactions of a Fusion

Demo-Reactor," Fusion Sci. Tech., **52**, 781 (2007).

174) Yoshida, M., and JT-60 Team, "Role of Pressure Gradient on Intrinsic Toroidal Rotation in Tokamak Plasmas," Physical Review Letters, **100**, 105002 (2008).

175) Yoshida, M., and JT-60 Team, "Momentum Transport and Plasma Rotation Profile in Toroidal Direction in JT-60U L-Mode Plasmas," Nucl. Fusion, **47**, 856 (2007).

176) Zanino, R., Astrov, M., (Takahashi, Y.), et al., "Predictive Analysis of the ITER Poloidal Field Conductor Insert (PFCI) Test Program," IEEE Trans. Appl. Superconduct., **17**, 1353 (2007).

177) Zucchetti, M., El-Guebaly, L.A., (Tobita, K.), et al., "The Feasibility of Recycling and Clearance of Active Materials from Fusion Power Plants," J. Nucl. Mater., **367-370**, 1355 (2007).

A.1.3 List of Papers Published in Conference Proceedings

1) Hayashi, T., Sakurai, S., Masaki, K., et al., "Conceptual Design of Divertor Cassette Handling by Remote Handling System for JT-60SA," Proc. 15th International Conference on Nuclear Engineering (ICONE-15) (CD-ROM), 8 (2007).

2) Isayama, A., and JT-60 Team, "Control of Current Profile and Instability by Radiofrequency Wave Injection in JT-60U and Its Applicability in JT-60SA," AIP Conference Proceedings 933, 229 (2007).

3) Isobe, K., Uzawa, M., Yamanishi, T., et al., "Development of Ceramic Electrolysis Method for Processing High-Level Tritiated Water," STI/PUB/1284 (CD-ROM), 7 (2007).

4) Kobayashi, N., Bigelow, T., Bonicelli, T., et al., "Design of Electron Cyclotron Heating and Current Drive System of ITER," AIP Conference Proceedings 933, 413 (2007).

5) Koide, Y., "Development in Diagnostics Application to Control of Advanced Tokamak Plasma," AIP Conference Proceedings 988, 413 (2008).

6) Kondoh, T., Kawano, Y., Hatae, T., et al., "Progress in Development of Collective Thomson Scattering Diagnostic with High Power CO_2 Laser," NIFS-PROC-68, 126 (2007).

7) Matsunami, N., Nakano, T., "Current Status of Chemical Sputtering of Graphite and Related Materials," Proc. International Symposium on EcoTopia Science 2007 (ISETS '07) (CD-ROM), 321 (2007).

8) Nishitani, T., Ishikawa, M., Kondoh, T., et al., "Absolute Neutron Emission Measurement in Burning Plasma Experiments," AIP Conference Proceedings 988, 267 (2008).

9) Sugie, T., Ogawa, H., Kasai, S., et al., "Spectroscopic Measurement System for ITER Divertor Plasma; Impurity Influx Monitor (Divertor)," AIP Conference Proceedings 988, 218 (2008).

10) Sukegawa, A., Oikawa, A., Miya, N., et al., "Estimation of Low Level Waste by a Regulatory Clearance in JT-60U Fusion Device," Proceedings of 15th International Conference on Nuclear Engineering (ICONE-15) (CD-ROM), 6 (2007).

11) Takahashi, K., Kajiwara, K., Kasugai, A., et al., "Investigation of Transmission Characteristic in Corrugated Waveguide Transmission Lines for Fusion Application," Proc. 8th IEEE International Vacuum Electronics Conference (IVEC 2007), 275 (2007).

12) Takato, N., Hanatani, J., (Inoue, T.), et al., "Numerical Analysis of the Hydrogen Atom Density in a Negative Ion Source," AIP Conference Proceedings 925, 38 (2007).

13) Takenaga, H., Oyama, N., Asakura, N., et al., "Divertor Density Measurements Using mm-Wave Interferometer in JT-60U," NIFS-PROC-68, 62 (2007).

A.1.4 List of other papers

1) Ando, M., Tanigawa, H., Shiba, K., et al., "Irradiation Creep Behavior of Reduced Activation Ferritic/Martensitic Steel Irradiated in HFIR," J. Jpn. Inst. Met., **71**, 559 (2007) (in Japanese).

2) Ando, M., Wakai, E., Okubo, N., et al., "Extra-Irradiation Hardening of Reduced Activation Ferritic/Martensitic Steel by Multi-Ion Irradiation," J. Jpn. Inst. Met., **71**, 1107 (2007) (in Japanese).

3) Ando, T., "Information on ITER Project, 3," J. Plasma Fusion Res., **82**, 533 (2007) (in Japanese).

4) Ando, T., "Information on ITER Project, 5," J. Plasma Fusion Res., **83**, 775 (2007) (in Japanese).

5) Ando, T., "Information on ITER Project, 7," J. Plasma Fusion Res., **84**, 69 (2008) (in Japanese).

6) Ando, T., "Information on ITER Project, 8," J. Plasma Fusion Res., **84**, 164 (2008) (in Japanese).

7) Araki, M., Kamada, Y., Mori, M., et al., "Current Status and Evolution of Nuclear Fusion Development; Aiming at the Achievement of the Nuclear Fusion Energy," Electrical Review, **92**, 38 (2007) (in Japanese).

8) Asakura, N., "Fast Plasma Flow in Tokamak Divertor and Scrape-Off Layer," J. Plasma Fusion Res., **83**, 501 (2007) (in Japanese).

9) Fujita, T., Fukuda, T., (Shinohara, K.), et al., "Report on ITPA (International Tokamak Physics Activity) Meeting, 20," J. Plasma Fusion Res., **84**, 70 (2008) (in Japanese).

10) Hayashi, T., Sakurai, S., Masaki, K., et al.,"Conceptual Design Study of Exchange of the In-Vessel Components by Remote Handling System for JT-60SA," Transactions of the American Nuclear Society, **96**, 783 (2007).

11) Higuchi, M., "Systematization of Standards," Maintenology, **6**, 73 (2007) (in Japanese).

12) Ida, M., Idomura, Y., Tokuda, S., "Gyrokinetic Simulation of Fusion Plasma Turbulence, 1; Modelling and Numerical Methods," Papers in the 2007 Annual Meeting of The Japan Society of Fluid Mechanics (CD-ROM), 5 (2007) (in Japanese).

13) Ide, S., "Present Status of Tokamak Research Towards Steady-State Operation," J. Plasma Fusion Res., **83**, 415 (2007) (in Japanese).

14) Ikeda, Y., "Recent Progress of Fusion Research," Text of The 39th Summer Seminar concerning the Reactor Physics by Atomic Energy Society of Japan, 160 (2007) (in Japanese).

15) Koide, Y., "On the JT-60 Joint Research Prize," J. Plasma Fusion Res., **84**, 230 (2008) (in Japanese).

16) Koizumi, N., Nishimura, A., "Intelligible Seminar on Fusion Reactors, 9; Superconducting Coil to Generate Magnetic Field for Plasma Confinement," J. Nucl. Sci. Tech., **47**, 703 (2007) (in Japanese).

17) Kurihara, K., "Principles of Magnetic Measurements," Handbook of the Modern Electric Power, 129 (2007) (in Japanese).

18) Maegawa, T., Yoshimatsu, K., Sato, S., "14 MeV Neutron Irradiation Test of Low-Activation Concrete with Limestone Powder," Denryoku Doboku, 86 (2008) (in Japanese).

19) Matsui, K., Koizumi, N., Nabara, Y., et al., "Evaluation of Thermal Strain Caused by Nb_3Sn Reaction Heat Treatment for the ITER Cable-in-Conduit Conductors," J. Cryo. Soc. Jpn., **42**, 311 (2007) (in Japanese).

20) Mori, M., "ITER Project in Detail," Genshiryoku eye, **53**, 11 (2007) (in Japanese).

21) Mori, M., Okuno, K., Sakamoto, K., "Information on ITER Project, 4," J. Plasma Fusion Res., **83**, 643

(2007) (in Japanese).

22) Mori, M., Yoshida, H., "Information on ITER Project, 6," J. Plasma Fusion Res., **83**, 928 (2007) (in Japanese).

23) Ninomiya, H., "Nuclear Fusion," Thermal Power Generation and Atomic Power Generation, **58**, 1038 (2007) (in Japanese).

24) Nishitani, T., "Detail of the Broader Approach Project," Genshiryoku eye, **53**, 21 (2007) (in Japanese).

25) Ohira, S., "Information of Broader Approach Activities, 2," J. Plasma Fusion Res., **83**, 398 (2007) (in Japanese).

26) Ohira, S., "Information of Broader Approach Activity, 3," J. Plasma Fusion Res., **83**, 587 (2007) (in Japanese).

27) Ohira, S., "Information of Broader Approach Activity, 4," J. Plasma Fusion Res., **83**, 716 (2007) (in Japanese).

28) Ohira, S., "Information of Broader Approach Activity, 5," J. Plasma Fusion Res., **83**, 853 (2007) (in Japanese).

29) Ohira, S., "Information of Broader Approach Activity, 7," J. Plasma Fusion Res., **84**, 229 (2008) (in Japanese).

30) Okuno, K., "Recent Progress in the Technology Development for the ITER Superconducting Coils," Superconductivity Communications, **16**, 6 (2007) (in Japanese).

31) Ozeki, T., "Realization of a Nuclear Fusion Experiment from a Remote Place by the Advanced Security," RIST News, 3 (2007) (in Japanese).

32) Ozeki, T., "Remote Hierarchical Environment of Experiment and Simulation," Simulation, **27**, 27 (2008) (in Japanese).

33) Ozeki, T., Watanabe, K., "Avoidance and Suppression of MHD Instability," J. Plasma Fusion Res., **83**, 44 (2007) (in Japanese).

34) Sakamoto, Y., Ida, K., "Control of High Confinement Plasmas," J. Plasma Fusion Res., **83**, 439 (2007) (in Japanese).

35) Sasao, M., Kusama, Y., Kawano, Y., et al., "Report of Meetings of ITPA (International Tokamak Physics Activity), 19," J. Plasma Fusion Res., **83**, 779 (2007) (in Japanese).

36) Sawahata, A., Tanigawa, H., Enomoto, M., "Effects of Electro-Slag Remelting on Inclusion Formation and Impact Property of Reduced Activation Ferritic/Martensitic Steels," J. Jpn. Inst. Met., **72**, 176 (2008) (in Japanese).

37) Shinohara, K., Takechi, M., Ishikawa, M., "Interaction Between Alfvén Eingenmodes and Energetic Ions on Tokamaks," J. Plasma Fusion Res., **83**, 873 (2007) (in Japanese).

38) Suzuki, S., Enoeda, M., Matsuda, H., et al., "Numerical Evaluation of Crack Propagation of ITER First Wall with an Initial Interfacial Defect," Transactions of the Atomic Energy Society of Japan, **6**, 365 (2007) (in Japanese).

39) Suzuki, T., "Current profile control in advanced tokamak plasmas," J. Plasma Fusion Res., **83**, 434 (2007) (in Japanese).

40) Takahashi, Y., "How is the ITER Project Going on?," Chodendo Web 21 (Internet), 25 (2008) (in Japanese).

41) Takeda, N., Kakudate, S., Nakahira, M., et al., “Current Status of Research and Development on Remote Maintenance for Fusion Components,” J. Plasma Fusion Res., **84**, 100 (2008) (in Japanese).

42) Takemura, M., “My First stay in Provence in the South of France,” FAPIG, 3 (2007) (in Japanese).

43) Takenaga, H., Morisaki, T., “Fuelling and Heat / Particle Control,” J. Plasma Fusion Res., **83**, 453 (2007) (in Japanese).

44) Tobita, K., “Challenges in Technology for Attractive Fusion Energy,” J. Inst. Electr. Eng. Jpn., **128**, 86 (2008) (in Japanese).

45) Urano, H., “Sun on the Earth,” Enjinia Ring, 9 (2007) (in Japanese).

46) Urano, H., Matsumoto, T., Matsunaga, G., “Conference Report on "10th Plasma Research Workshop by Young Scientists" J. Plasma Fusion Res., **82**, 534 (2007) (in Japanese).

47) Ushigusa, K., Seki, M., Ninomiya, H., et al., “Research and Development of Nuclear Fusion,” Genshiryoku Handbook, 906 (2007) (in Japanese).

48) Yamanishi, T., Iwai, Y., Isobe, K., et al., “Developments of Water Detritiation Systems in a Fusion Reactor,” J. Plasma Fusion Res., **83**, 545 (2007) (in Japanese).

49) Yoshida, H., “The Trend of Fusion Energy Research and Development in the Participant Party and Countries in the ITER Project,” Genshiryoku eye, **53**, 31 (2007) (in Japanese).

A.2 Organization of Fusion Research and Development Directorate

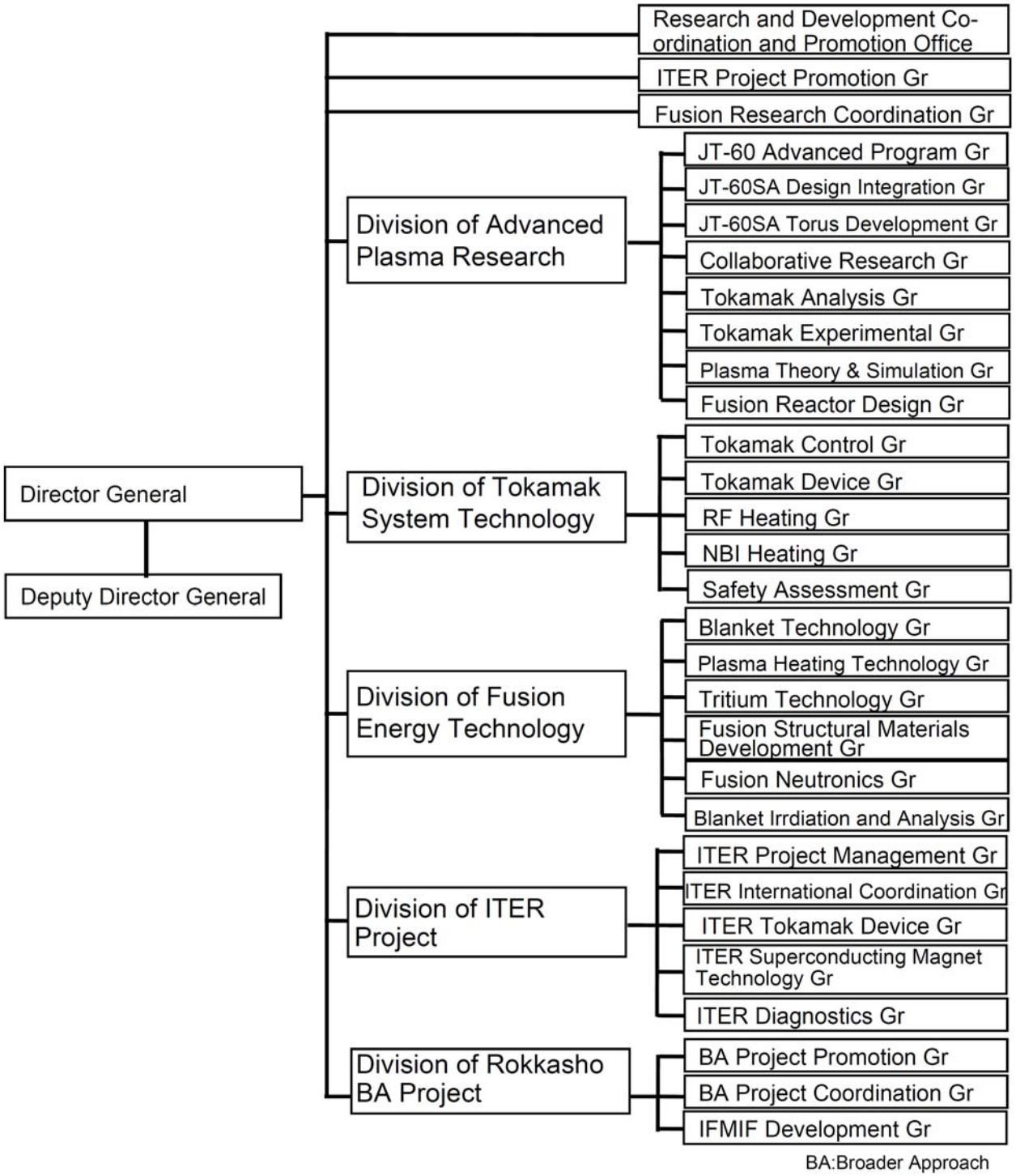

A.3 Personnel Data

A.3.1 Staff in Fusion Research and Development Directorate of JAEA

Fusion Research and Development Directorate

TSUNEMATSU Toshihide	(Director General)
NINOMIYA Hiromasa	(Deputy Director General)
OKUMURA Yoshikazu	(Deputy Director General)
NAGAMI Masayuki	(Supreme Researcher)
TANI Keiji	(Senior Principal Researcher)
YOSHIDA Hidetoshi	(Principal Researcher)
SEKI Masahiro	(Invited Researcher)
SEKI Shogo	(Invited Researcher)
SHIMOMURA Yasuo	(Invited Researcher)
MATSUI Hideki	(Invited Researcher)
KOHYAMA Akira	(Invited Researcher)
IDA Katsumi	(Invited Researcher)
KISHIMOTO Yasuaki	(Invited Researcher)

Research and Development Co-ordination and Promotion Office

NINOMIYA Hiromasa	(General Manager)	
WATANABE Tsutomu	(Deputy General Manager)	
GUNJI Masato	Hayashi Kazuyuki	KIMURA Shoko
KOYANAGI Daisaku	MATSUMOTO Hiroyuki	MORITA Hisao
NEMOTO Tetsuo	ONOZAKI Kazutoyo	SOGA Yoriko
TSUCHIDA Tatsuro	YOSHIDA Hiroshi	

ITER Project Promotion Group

SHIRAI Hiroshi	(Group Leader)
DOI Kenshin	OGAWA Toshihide

Fusion Research Coordination Group

USHIGUSA Kenkichi	(Group Leader)
ISEI Nobuaki	OOHARA Hiroshi

Division of Advanced Plasma Research

KIKUCHI Mitsuru	(Unit Manager)
OZEKI Takahisa	(Senior Principal Researcher)

JT-60 Advanced Program Group

KAMADA Yutaka	(Group Leader)
TAKENAGA Hidenobu	URANO Hajime

JT-60SA Design Integration Group

MATSUKAWA Makoto	(Group Leader)

YOSHIDA Kiyoshi	(Deputy Group Leader)	
KAWASHIMA Hisato	TSUCHIYA Katsuhiko	KIZU Kaname
TSUKAHARA Yoshimitsu	HOSHI Ryo (*4)	MATSUMURA Hiroshi (*4)
SUZUKI Yutaka (*17)	EDAYA Masahiro (*31)	SATO Fujio (*7)
KOMEDA Masao (*16)		

Collaborative Research Group

KOIDE Yoshihiko	(Group Leader)	
IDE Shunsuke	(Deputy Group Leader)	
HOSHINO Katsumichi	KAMIYA Kensaku	KONOSHIMA Shigeru (*1)

Tokamak Analysis Group

OZEKI Takahisa	(Group Leader)	
NAITO Osamu	(Deputy Group Leader)	
AIBA Nobuyuki (*23)	HAMAMATSU Kiyotaka	HAYASHI Nobuhiko
HONDA Mitsuru (*23)	KIYONO Kimihiro	KAMATA Isao (*24)
KOMINATO Toshiharu (*2)	SAKATA Shinya	SATO Minoru
SHIMIZU Katsuhiro	SUZUKI Mitsuhiro (*31)	TAKIZUKA Tomonori (*1)

Tokamak Experimental Group

ITAMI Kiyoshi	(Group Leader)	
ASAKURA Nobuyuki	(Deputy Group Leader)	
CHIBA Shinichi	FUJIMOTO Kayoko (*23)	HANAWA Osamu (*22)
HATAE Takaki	ISAYAMA Akihiko	KOIKE Tomonori (*22)
KITAMURA Shigeru	KOJIMA Atsushi (*23)	MATSUNAGA Go
MIYAMOTO Atsushi (*21)	NAKANO Tomohide	NUMATA Hiroyuki (*22)
OYAMA Naoyuki	SAKAMOTO Yoshiteru	SHINOHARA Kouji
SUNAOSHI Hidenori	SUZUKI Takahiro	TSUBOTA Naoaki (*21)
TSUTSUMI Kazuyoshi (*21)	UEHARA Kazuya (*1)	YOSHIDA Maiko (*25)

Plasma Theory & Simulation Group

TOKUDA Shinji	(Group Leader)	
IDOMURA Yasuhiro	ISHII Yasutomo	KAGEI Yasuhiro (*25)
LESUR Maxime (*3)	MATSUMOTO Taro	MIYATO Naoaki
SUZUKI Yoshio	TUDA Takashi (*1)	

Fusion Reactor Design Group

TOBITA Kenji	(Group Leader)	
NAKAMURA Yukiharu	KURITA Gen-ichi	NISHIO Satoshi

JT-60SA Torus Development Group

SAKASAI Akira	(Group Leader)	
HIGASHIJIMA Satoru	KASHIWA Yoshitoshi	MASAKI Kei
SAKURAI Shinji	SHIBAMA Yusuke	TAKECHI Manabu

Division of Tokamak System Technology

HOSOGANE Nobuyuki	(Unit Manager)	
YAMAMOTO Takumi	(Senior Principal Researcher)	
FUJII Tsuneyuki	(Senior Principal Researcher)	

Tokamak Control Group

KURIHARA Kenichi	(Group Leader)	
AKASAKA Hiromi	HOSOYAMA Hiromi (*8)	KAMIKAWA Masaaki (*10)
KAWAMATA Youichi	MATSUKAWA Tatsuya (*21)	OHMORI Yoshikazu
OKANO Jun	SATO Tomoki (*31)	SEIMIYA Munetaka (*1)
SHIBATA Kazuyuki (*22)	SHIMADA Katsuhiro	SUEOKA Michiharu
TERAKADO Hiroyuki (*7)	TERAKADO Tsunehisa	TOTSUKA Toshiyuki
YAMAUCHI Kunihito	WADA Kazuhiko (*22)	

Tokamak Device Group

SATO Masayasu	(Group Leader)	
ARAI Takashi	HAGA Saburo (*21)	ICHIGE Hisashi
ISHIGE Youichi (*22)	KAMINAGA Atsushi	MATSUZAWA Yukihiro (*21)
MIYO Yasuhiko	NISHIYAMA Tomokazu	OKANO Fuminori
SASAJIMA Tadayuki	SATO Yoji (*21)	SUZUKI Yozo (*4)
YAGYU Jun-ichi		

RF Heating Group

HOSOGANE Nobuyuki	(Group Leader)	
HIRANAI Shinichi	HASEGAWA Koichi	IGARASHI Koichi (*21)
KOBAYASHI Takayuki (*23)	MORIYAMA Shinichi	SATO Fumiaki (*21)
SAWAHATA Masayuki	SHIMONO Mitsugu	SUZUKI Sadaaki
SUZUKI Takashi (*22)	TERAKADO Masayuki	WADA Kenji (*21)
YOKOKURA Kenji		

NBI Heating Group

IKEDA Yoshitaka	(Group Leader)	
AKINO Noboru	EBISAWA Noboru	HANADA Masaya
HONDA Atsushi	KAMADA Masaki (*23)	KAWAI Mikito
KAZAWA Minoru	KIKUCHI Katsumi (*22)	KOBAYASHI Kaoru (*4)
KOMATA Masao	MOGAKI Kazuhiko	NOTO Katsuya (*21)
OOASA Kazumi	OSHIMA Katsumi (*21)	SASAKI Shunichi
SHIMIZU Tastuo (*21)	SHINOZAKI Shinichi	TAKENOUCHI Tadashi (*29)
TANAI Yutaka (*22)	USUI Katsutomi	

Safety Assessment Group

MIYA Naoyuki	(Group Leader)	
SUKEGAWA Atsuhiko	HAYASHI Takao	OIKAWA Akira (*1)

Division of Fusion Energy Technology

TAKATSU Hideyuki	(Unit Manager)	
NISHITANI Takeo	(Senior Principal Researcher)	

Blanket Technology Group

AKIBA Masato	(Group Leader)	
ENOEDA Mikio	EZATO Koichiro	HIROSE Takanori
HOMMA Takashi (*1)	MOHRI Kensuke (*12)	NISHI Hiroshi
SEKI Yohji (*23)	SUZUKI Satoshi	TANIGAWA Hisashi
TANZAWA Sadamitsu	TSURU Daigo	YOKOYAMA Kenji

Plasma Heating Group

SAKAMOTO Keishi	(Group Leader)	
INOUE Takashi	(Deputy Group Leader)	
DAIRAKU Masayuki	IKEDA Yukiharu	KASHIWAGI Mieko
KASUGAI Atsushi	KAJIWARA Ken (*25)	KOBAYASHI Noriyuki (*30)
KOMORI Shinji (*22)	OMINE Takashi (*31)	TAKAHASHI Koji
TAKESHIMA Yuichirou (*5)	TANIGUCHI Masaki	TOBARI Naoyuki (*25)
UMEDA Naotaka	WATANABE Kazuhiro	YAMAMOTO Masanori (*4)

Tritium Technology Group

YAMANISHI Toshihiko	(Group Leader)	
ARITA Tadaaki(*26)	HAYASHI Takumi	HOSHI Shuichi(*22)
INOMIYA Hiroshi(*22)	ISOBE Kanetsugu	IWAI Yasunori
KAWAMURA Yoshinori	KOBAYASHI Kazuhiro	NAKAMURA Hirofumi
SHU Wataru	SUZUKI Takumi	YAMADA Masayuki

Fusion Structural Materials Development Group

TAKATSU Hideyuki	(Group Leader)	
TANIGAWA Hiroyasu	(Deputy Group Leader)	
ANDO Masami	NOZAWA Takashi (*25)	OGIWARA Hiroyuki (*23)
SAWAHATA Atsushi (*5)	NAKATA Toshiya (*18)	

Fusion Neutronics Group

KONNO Chikara	(Group Leader))	
ABE Yuichi	IIDA Hiromasa (*1)	KAWABE Masaru (*22)
KUTSUKAKE Chuzo	OCHIAI Kentaro	OKADA Koichi (*28)
OHNISHI Seiki (*25)	SATO Satoshi	TAKAKURA Kosuke (*21)
TANAKA Shigeru		

Blanket Irradiation and Analysis Group

HAYASHI Kimio	(Group Leader)	
NAKAMICHI Masaru	HOSHINO Tsuyoshi	YONEHARA Kazuo (*9)
HASEGAWA Teiji (*22)	NAMEKAWA yoji (*22)	TSUCHIYA Kunihiko

Division of ITER Project

YOSHINO Ryuji		(Unit Manager)

ITER Project Management Group

KOIZUMI Koichi	(Group Leader)	
NEYATANI Yuzuru	(Deputy Group Leader)	
KITAZAWA Siniti	IWAMA Yasushi (*21)	SENGOKU Akio (*21)
KOIKE Kazuhisa (*21)	YAGUCHI Eiji (*13)	SATO Koichi (*31)
SATO Kazuyoshi	HIGUCHI Masahisa (*27)	

ITER International Coordination Group

MORI Masahiro	(Group Leader)	
ANDO Toshiro	(Deputy Group Leader)	
OIKAWA Toshihiro	ODAJIMA Kazuo (*1)	

ITER Tokamak Device Group

SHIBANUMA Kiyoshi	(Group Leader)	
KAKUDATE Satoshi	KOZAKA Hiroshi (*21)	MATSUMOTO Yasuhiro (*30)
TAGUCHI Kou (*22)	TAKEDA Nobukazu	

ITER Superconducting Magnet Technology Group

OKUNO Kiyoshi	(Group Leader)	
NAKAJIMA Hideo	(Deputy Group Leader)	
HAMADA Kazuya	HEMMI Tsutomu	ISONO Takaaki
KAWANO Katsumi	KOIZUMI Norikiyo	MATSUI Kunihiro
NABARA Yoshihiro	NAKAHIRA Masataka	NIIMI Kenichiro (*11)
NUNOYA Yoshihiko	OHMORI Junji (*30)	OKUI Yoshio (*14)
OSHIKIRI Masayuki (*22)	SEO Kazutaka (*19)	SHIMANE Hideo (*13)
SHIMIZU Tatuya (*13)	TAKAHASHI Yoshikazu	TAKANO Katsutoshi (*22)
TSUTSUMI Fumiaki (*31)		

ITER Diagnostics Group

KUSAMA Yoshinori	(Group Leader)	
FUJIEDA Hirobumi	HAYASHI Toshimitsu (*20)	ISHIKAWA Masao (*25)
KAJITA Shin (*25)	KAWANO Yasunori	KONDOH Takashi
OGAWA Hiroaki	SUGIE Tatsuo	TAKEI Nahoko (*23)
YAMAGUCHI Taiki (*23)	YAMAMOTO Tsuyoshi (*8)	

Division of Rokkasho BA Project

OKUMURA Yoshikazu	(Unit Manager)

BA Project Promotion Group

OHIRA Shigeru	(Group Leader)
EJIRI Shintaro	(Deputy Group Leader)

BA Project Coordination Group

OHIRA Shigeru	(Group Leader)
TAKEMOTO Junpei (*10)	

IFMIF Development Group

OKUMURA Yoshikazu	(Group Leader)	
NAKAMURA Hiroo	(Deputy Group Leader)	
ASAHARA Hiroo(*21)	IDA Mizuho (*6)	MAEBARA Sunao
KIKUCHI Takayuki	KOJIMA Toshiyuki(*21)	KUBO Takashi (*15)
MIYASHITA Makoto (*30)	YONEMOTO Kazuhiro(*10)	

A.3.2 Staff in ITER Organization and Project Teams of the Broader Approach Activities

ITER Organization

Office of Director-General

MATSUMOTO Hiroshi (Head)

Project Office

TADA Eisuke (Head)

Department for Administration

IDE Toshiyuki

Department for Fusion Science & Technology

SHIMADA Michiya

Department for Central Engineering & Plant Support

MARUYAMA So

Project Teams of the Broader Approach Activities

International Fusion Energy Research Center

ARAKI Masanori (Project Leader)

Satellite Tokamak Programme

ISHIDA Shinichi	(Project Leader)	
FUJITA Takaaki	KIMURA Haruyuki	OSHIMA Takayuki
SEKI Masami	TAMAI Hiroshi	

IFMIF EVEDA

SUGIMOTO Masayoshi	(Deputy Project Leader)
NAKAMURA Kazuyuki	SHINTO Katsuhiro(*25)

A.3.3 Collaborating Laboratories

Tokai Research and Development Center

Nuclear Science and Engineering Directorate

Irradiation Field Materials Research Group

JITSUKAWA Shiro	(Group Leader)	
FUJII Kimio	OKUBO Nariaki	TANIFUJI Takaaki
WAKAI Eiichi	YAMAKI Daiju	

Research Group for Corrosion Damage Mechanism

MIWA Yukio

Quantum Beam Science Directorate

Nanomaterials Synthesis Group

TAGUCHI Tomitsugu

Oarai Research and Development Center

Technology Development Department

MIYAKE Osamu (Deputy Director)

Advanced Liquid Metal Technology Experiment Section

YOSHIDA Eiichi (General Manager)

HIRAKAWA Yasushi

Advanced Nuclear System Research and Development Directorate

Innovative Technology Group

ARA Kuniaski (Group Leader)

OTAKE Masahiko

*1 Contract Staff
*2 Customer System Co., Ltd.
*3 Ecole Polytechnique (France)
*4 Hitachi, Ltd.
*5 Ibaraki University
*6 Ishikawajima-Harima Heavy Industries Co., Ltd.
*7 JP HYTEC Co., Ltd.
*8 Japan EXpert Clone Corp.
*9 KAKEN Co., Ltd.
*10 Kandenko Co., Ltd.
*11 Kawasaki Heavy Industries, Ltd.
*12 Kawasaki Plant Systems, Ltd.
*13 KCS Corporation
*14 Kobe Steel, Ltd.
*15 Kumagai Gumi Co., Ltd.
*16 MAYEKAWA MFG. CO., LTD
*17 Mitsubishi Heavy Industries, Ltd.
*18 Muroran Institute of Technology
*19 National Institute for Fusion Science
*20 NEC Corporation
*21 Nippon Advanced Technology Co., Ltd.
*22 Nuclear Engineering Co., Ltd.
*23 Post-Doctoral Fellow
*25 Princeton Plasma Physics Laboratory (USA)
*24 Research Organization for Information Science & Technology
*25 Senior Post-Doctoral Fellow
*26 Sumitomo Heavy Industries, Ltd.
*27 The Japan Atomic Power Company
*28 Tohoku University
*29 Tomoe Shokai Co., Ltd.
*30 Toshiba Corporation
*31 Total Support Systems